Low Power Autonomous Microsystem for Oil Well Logging Applications

by

Yu Sui

A dissertation submitted in partial fulfillment
of the requirements for the degree of
Doctor of Philosophy
(Electrical Engineering)
in the University of Michigan
2017

Doctoral Committee:

Professor Yogesh B. Gianchandani, Co-Chair
Assistant Research Scientist Tao Li, Co-Chair
Professor Duxin Sun
Professor Khalil Najafi

Yu Sui

sui@umich.edu

ORCID iD: 0000-0002-4440-0706

© Yu Sui 2017

ACKNOWLEDGEMENTS

The research described by this dissertation was funded in part by the Advanced Energy Consortium (AEC) and by National Science Foundation (NSF). Some fabrication and characterization were performed at the Lurie Nanofabrication Facility (LNF) operated by the Solid-State Electronics Laboratory (SSEL) at the University of Michigan. The systems used in this research were packaged by Dr. Yushu Ma, Ms. Neeharika Vellaluru, and Mr. Andrew Trickey-Glassman. The software in this research was partially developed by Mr. Ryan Meredith and Ms. Wenching Tsai. The sapphire substrate pressure sensor and the RF switch in this research were fabricated by Mr. Alexander Benken. The HPHT tests in this research were performed at external laboratories and facility, including RTI International (Research Triangle Park, NC), Exploration and Production R&D Division at Total (Pau, France), and in a brine well (Vauvert, France). Some of these tests were performed by Mr. Andrew Trickey-Glassman. I sincerely appreciate all the researchers involved for their assistance in these tests.

I want to express my deepest gratitude to my advisor Prof. Yogesh Gianchandani. His enthusiasm, advanced research vision, and high efficiency in enforcing research plans, have kept inspiring me through my Ph.D. study. Under his guidance, I become better in conducting research, solving problems as well as writing articles. I am also grateful to my co-advisor and mentor Dr. Tao Li for his constant guidance in my research. Dr. Li has been extremely professional, intelligent, kind and helpful. He not only provided valuable advice on research methodology, but also encouraged me when I faced difficulties. I would also like to thank the other committee members,

Prof. Khalil Najafi and Prof. Duxin Sun, for their constructive comments and valuable suggestions in my dissertation.

I would like to thank the staff members at the University of Michigan, including Pillar Herrera-Flerro, Nadine Wang, Terre Briggs, Matt Oonk, Steven Sostrom, Tom Latowski, Vishva Ray, Lisa Stowe, Trasa Burkhardt, Larry Tuttle, Robert Gordenker, Barb Rice, Wendy Umbriac, Jim Kozich, Nicole Doher, and many others, whose professional attitudes and timely help have made my research going smoothly.

I would like to thank the members of Prof. Gianchandani's research group, including Scott, Erwrin, Seungdo, Anup, Jun, Ravish, Xin, Yutao, Venkat, Yushu, Shiyang, Andy, Alex, Qisen, Jiqing, Neeharika, Ramprasad, Ryan, Jonathan, Robin, and many others. I would also like to thank my friends, including Stacey, Yi, Tal, Amin, Ali, Christopher, Farzad, Sajal, and many others. Their warm encouragement and fully supports have helped me get through many difficulties in my Ph.D. journey.

Finally, I would like to thank my family members, especially my parents, for their unconditional love to me.

TABLE OF CONTENTS

ACKNOWLEDGEMENTS **ii**

LIST OF FIGURES **vi**

LIST OF TABLES **xv**

LIST OF APPENDICES **xvi**

ABSTRACT **xvii**

CHAPTER 1: INTRODUCTION **1**

1.1. BACKGROUND AND MOTIVATION 1
1.2. CHALLENGES OF MICROSYSTEMS FOR DOWNHOLE APPLICATIONS 8
1.3. ELECTRONICS FAILURE UNDER STRESSED CONDITION 12
1.4. COMMUNICATION METHODS FOR MICROSYSTEMS 14
1.5. GOALS AND CHALLENGES 17
1.6. ORGANIZATION OF THE DISSERTATION 19

CHAPTER 2: AUTONOMOUS MICROSYSTEM FOR DOWNHOLE TEMPERAUTRE LOGGING **22**

2.1. SYSTEM HARDWARE 22
2.2. SYSTEM SOFTWARE 31
2.3. SYSTEM FABRICATION AND PACKAGING 37
2.4. EXPERIMENTAL METHODS AND RESULTS 40
2.5. DISCUSSION AND SUMMARY 50

CHAPTER 3: AUTONOMOUS MICROSYSTEM FOR DOWNHOLE TEMPERAUTRE AND PRESSURE LOGGING **53**

3.1. ELM2.0 & ELM2.1 SYSTEM DESIGN 54
3.2. ELM2.0 AND ELM2.1 SYSTEM FABRICATION AND PACKAGING 60
3.3. ELM3.0 SYSTEM DESIGN 63
3.4. ELM2.0 AND ELM2.1 EXPERIMENTAL RESULTS FROM LABORATORY TESTS 66
3.5. FIELD TESTS OF ELM2.0 AND ELM3.0 SYSTEMS IN A BRINE WELL 76
3.6. ELM PRESSURE SENSOR CALIBRATION AND PRESSURE INTERPRETATION 78
3.7. CAPACITANCE DRIFT ANALYSIS AND CORRECTION 85
3.8. DISCUSSION AND SUMMARY 101

CHAPTER 4: INVESTIGATION OF A POLYIMIDE PRESSURE SENSOR **103**
4.1. MOTIVATION AND LITERATURE REVIEW 104
4.2. DEVICE CONCEPT AND THEORETICAL ANALYSIS 107
4.3. DEVICE FABRICATION 114
4.4. EXPERIMENTAL RESULTS 115
4.5. DISCUSSION AND SUMMARY 119
CHAPTER 5: CONCLUSION AND FUTURE WORK **121**
5.1. CONCLUSIONS 121
5.2. FUTURE WORK 123
APPENDICES **129**
REFERENCE **166**

LIST OF FIGURES

Figure 1.1: The principle of wireline logging. The wireline tool is lowered into the oil well for environmental monitoring [Ell07]. 3

Figure 1.2: (a) The principle of cross-well electromagnetic imaging. The transmitter generates a primary electromagnetic field and the field is received by the receiver. (b) The operation of the cross-well imaging. The target zone is illuminated at several angles by moving the transmitter and receiver [Sch06]. 4

Figure 1.3: A typical application scenario of the autonomous sensing microsystems in the downhole environment.......... 5

Figure 1.4: (a) The downhole smart ball developed by Openfield™ Technlogy, which has a diameter of 50.8 mm [Ope13]. (b) The downhole sensor developed by University of Tulsa and Saudi Aramco, with a diameter of 7.5 mm [Shi15]. 6

Figure 1.5: Leakage path for a typical NMOS transistor. The three main leakage paths are reverse-biased PN junction leakage (I_1), subthreshold leakage (I_2) and gate leakage (I_3, I_4) [Roy03]........ 9

Figure 1.6: The failure in time (FIT) for the Silicon Laboratories 0.18 µm process with embedded flash over temperature. The increase of FIT at elevated temperatures results from temperature acceleration of several failure mechanisms, such as surface charge accumulation and charge injection [Sze88, Ohr98]. 14

Figure 2.1: The block diagram of the ELM1.0. The system consists of a solar cell for charging, two LED indicators for data reporting, a low power MCU for system control and temperature sensing, a charging circuit for wireless charging, a Schmitt trigger for charging protection and a 3 V lithium battery for energy storage. 24

Figure 2.2: The schematic of the system circuit of ELM1.0. It consists of a charging circuit block, a Schmitt trigger block, an MCU and two LED indicators.......... 25

Figure 2.3: (a) The MS412FE battery from Seiko Instruments [Sei14]. (b) The CPC1822 photodiode from IXYS Integrated Circuit Division [Ixy12]. 28

Figure 2.4: Measured current consumption of the MCU at various power supply voltages. The peak current consumption appears at 1.6 V V_{supply}. This current consumption significantly exceeds the maximum allowed continuous discharging current of the lithium battery (100 μA) [Sei14]. 29

Figure 2.5: The block diagram of the optical communication box. The box contains hardware for optical communication and is controlled by a Labview™ user interface program. A data acquisition card is connected between the box and the PC. 30

Figure 2.6: Overall system software state diagram. The system consists of 7 regular operation states. The transition between states is triggered by light patterns specified in the table. 32

Figure 2.7: The diagram of sub-states for State 4, the detection state. 33

Figure 2.8: The diagram of sub-states for State 5, the readout state. 34

Figure 2.9: Typical operation flow chart of the ELM1.0. After assembly and packaging, the system is put into deep sleep state for storage. Recharge is required before the deployment of the system. During deployment, the system will go through detection state, deep sleep state, readout state, and back to deep sleep state. 35

Figure 2.10: Configuration of the folded system stack. Top layer: solar cell and LEDs. Middle layer: battery. Bottom layer: Electronics. Flexible polyimide PCB is used for electrical interconnect between layers. 38

Figure 2.11: Photos of the ELM1.0. (a) Photo of ELM1.0 flexible polyimide PCB before assembly. (b) Photo of the folded ELM1.0 stack. (c) Photo of the ELM1.0 in the package. 39

Figure 2.12: Results of the Schmitt trigger circuit test. The measured threshold voltages were V_H = 2.45 V and V_L = 1.95 V. These voltages matches the calculated threshold values. 41

Figure 2.13: The static current consumption of the system in active / sleep mode at various temperatures. Power supply V_B = 2.4 V is selected for representing the average voltage in the system operation cycles. 42

Figure 2.14: The temperature data recorded in the system calibration test. The offset increases with temperature and reaches 3.5°C at the environment temperature of 128.9°C........................ 43

Figure 2.15: The results of the high temperature system test in an emulated operational flow. (a) Step 1, the discharge curve of the system battery in storage. (b) Step 2, the charging curve of the system battery. (c) Step 3, the discharge curve of the system battery in the high temperature test. (d) Step 3, the temperature data stored in the MCU flash memory during the high temperature test. 45

Figure 2.16: The reported temperature curve during the stressed high temperature test. The system is able to measure temperature up to 150°C. 46

Figure 2.17: The HPHT testing procedure for ELM1.0 system at Pau, France. 47

Figure 2.18: The summary of the testing results at Total Research Center, Pau, France. The ELM1.0 survived 125°C and 7200 psi in API brine. It also survived 10000 psi and cement slurry solution. 48

Figure 2.19: (a) Temperature and pressure in the testing cell reported by the HPHT instrument from the standard HPHT test. (b) Temperature data reported by the system during the standard HPHT test. (c) Temperature and pressure reported by the HPHT instrument from the extended duration test. (d) Temperature data reported by the system during the extended duration test. ... 49

Figure 2.20: The measured temperature during the flight test from Pau, France to Detroit, USA. A total amount of 16 hours data were collected. 50

Figure 3.1: (a) The block diagram for ELM2.0. (b) The block diagram for ELM2.1. 55

Figure 3.2: (a) The circuit schematic of ELM2.0. The ELM2.0 includes one Murata pressure sensor and one custom pressure sensor. (b) The circuit schematic of ELM2.1. The ELM2.1 has all the components of ELM2.0, and incorporates one STM inertial sensor and one Murata RFID tag. 57

Figure 3.3: (a) Schematic diagram and (b) photo of the Murata capacitive pressure sensor. 58

Figure 3.4: The photo of the micromachined pressure sensor developed at the University of Michigan, denoted as "U. Michigan pressure sensor". 59

Figure 3.5: The software state diagram for the ELM2.0 system. The detection state has been upgraded and two new states – the battery check state and the parameter change state – have been implemented. 60

Figure 3.6: Configuration of the folded ELM2.0 PCB in steel package. Top layer: solar cell and LEDs. Middle layer: lithium battery. Bottom layer: MCU, pressure sensors and other electronics. The stack is packaged in the stainless steel tube filled with transparent silicone. The overall encapsulated stack is 9.5×9.5×6.5 mm^3 (L×W×H) in size. 61

Figure 3.7: Photos of ELM2.0 and ELM2.1 before packaging. (a) Photo of ELM2.0 before folding. (b) Photo of the ELM2.0 after one fold. (c) Photo of ELM2.1 before folding. 62

Figure 3.8: The encapsulation process of the ELM2.0 system with silicone as filler material. ... 63

Figure 3.9: The ELM2.0 system in a steel package filled with silicone caulk. 63

Figure 3.10: The circuit schematic of the ELM3.0 system. 64

Figure 3.11: The folded stack diagram of the ELM3.0 system. The stack consists of four layers in total. 65

Figure 3.12: (a) The molding process of the ELM3.0 system. (b) Photo of the ELM3.0 system in RTI epoxy. (c) Photo of the ELM2.0 system in silicone caulk.. 66

Figure 3.13: The amplification circuit for ELM3.0 transient current measurement.................... 67

Figure 3.14: Transient current consumption of ELM at 25°C, 125°C and 150°C. (a) The transient current of ELM during multiple full detection events. The wake-up period is set ats 3 s for oscilloscope measurement. (b) The magnified view of the current at the beginning of each detection event, view 1. (c) The magnified view of the current at the end of each detection event, view 2. 68

Figure 3.15: (a) Setup for characterization of temperature effect of the MCU capacitive sensing module. (b) Change of capacitance measured by the MCU at different temperatures for different ceramic capacitors. 70

Figure 3.16: The measured temperature during the cycled lifetime test. The system survived six 3-hr test cycles at 125°C. The system failed at 7th cycle due to possible flash writing error. 71

Figure 3.17: The change in capacitance of the Murata pressure sensor recorded by the ELM system and the applied pressure recorded by a reference pressure transducer during one of the medium pressure tests. 72

Figure 3.18: The summary of the successful HPHT tests performed on the ELM2.0 system. The testing durations are indicated. 74

Figure 3.19: (a) Temperature and pressure reported by the testing equipment, and the MCU temperature and interpreted pressure from ELM2.0 during the HPHT test. (b) Temperature (*Temp.MCU*) and capacitance changes (*ΔC.PS.Raw*, *ΔC.PS.Cor*, and *ΔC.RefCap*) recorded by ELM during the HPHT test. 75

Figure 3.20: The setup for the brine well test. The ELMS are mounted in clamp together with reference modules. The systems were lowered into the well via the steel cable controlled by a winch. The systems were lowered to a maximum depth of 1235 m. 77

Figure 3.21: Pressure and temperature data collected by the Openfield^{TM} apparatus, and ELM temperature data and ELM converted pressure data. 77

Figure 3.22: The proposed calibration procedure for the ELM2.0 system. These three steps correct offset, gain and linearity. More steps can be added to further correct the transfer function. 80

Figure 3.23: (a) The idealized transfer function *g(p)*, the output capacitance from an ELM2.0 system over applied pressure, and the capacitance after each step of calibration. (b) The interpreted pressure error using *g(x)* after each calibration step. 81

Figure 3.24: (a) Temperature and pressure reported by the testing equipment, and the MCU temperature and interpreted pressure from ELM2.0-15 in Pau Test A1. (b) Temperature (*Temp.MCU*) and capacitance changes (*ΔC.PS.Raw*, *ΔC.PS.Cor*, and *ΔC.RefCap*) recorded by ELM2.0-15 in Pau Test A1. (c) Corrected ΔC of the pressure sensor (ΔC.PS.Cor) plotted as a function of the applied pressure for ELM in HPHT test. The trend line uses second order fit. .. 84

Figure 3.25: (a) Temperature (*Temp.MCU*) and capacitance changes (*ΔC.PS.Raw*, *ΔC.PS.Cor*, and *ΔC.RefCap*) recorded by one ELM during the HPHT test at 55°C, 1400 psi. The capacitance drifted over time with certain drift rate. (b) Temperature and pressure reported by the testing equipment, and the MCU temperature and interpreted pressure from the ELM3.0 during the HPHT test. The interpreted pressure drifted up while the environment pressure was stable. 86

Figure 3.26: (a) The recorded temperature and capacitance of the 10 pF reference capacitor, with a capacitance drift rate of 0.028 fF/min; (b) The recorded temperature and capacitance of the 0.2 pF reference capacitor, with a capacitance drift rate of 0.027 fF/min. The ELM3.0-DR1 was used for the tests. (c) Summary of capacitance drift rates of the ELM reference capacitors from the in-lab long duration test.. 88

Figure 3.27: The illustration of the LaGrange multiplier method. At the maximum point (x_0, y_0), both $\nabla f(x_0,y_0)$ and $\nabla g(x_0,y_0)$ should be orthogonal to the $g(x,y) = 0$ curve. 93

Figure 3.28: (a) The drift rate, normalized temperature for C100 sensors and their reference capacitors, and the principal component between drift rate and temperature. (b) The drift rate, normalized pressure for C100 sensors and their reference capacitors, and the principal component between drift rate and pressure. The data are from the C100 sensors and their reference capacitors. 95

Figure 3.29: (a) The *ΔC.PS.Cor* with and without drift rate correction for ELM3.0-AF3.4, Vauvert test B2. (b) The *ΔC.PS.Cor* with and without drift rate correction for ELM3.0-AF3.6 Vauvert test B5. Both systems were assembled with C100 pressure sensors and packaged in RTI epoxy. 97

Figure 3.30: (a) Temperature and pressure reported by the testing equipment, and the MCU temperature and interpreted pressure for Vauvert Test B2, AF-34 device. (b) Temperature and pressure reported by the testing equipment, and the MCU temperature and interpreted pressure for

Vauvert Test B5, AF-36 device. Linear transfer curve is used to interpret the environment pressure. 99

Figure 3.31: (a) Temperature and pressure reported by the testing equipment, and the MCU temperature and interpreted pressure for Vauvert Test B2, AF3.4 device. (b) Temperature and pressure reported by the testing equipment, and the MCU temperature and interpreted pressure for Vauvert Test B5, AF3.6 device. (c) The fitted second order transfer function for pressure interpretation used in (a). (d) The fitted second order transfer function for pressure interpretation used in (b). 101

Figure 4.1: (a) The photo of the piezo-resistive pressure sensor fabricated using SU-8 at National Cheng Kung University [Ko07]. (b) The schematic of the polyimide capacitive pressure sensor fabricated in at the University of Twente [Ped97]. 105

Figure 4.2: The schematic of the low-cost polyimide sensor. 107

Figure 4.3: The four sensor geometries used for FEA analysis. (a) The square-shaped sensor (LC-SQ). (b) The round-shaped sensor (LC-R). (c) The T-shaped sensor fabricated on ELM3.0 and tested later (LC-T). (d) The rectangular strip array sensor (LC-RS). All of these geometries have an active area of 20 mm^2. 110

Figure 4.4: The simulated ΔC over applied pressure for various shapes of sensors with an area of 20 mm^2. 111

Figure 4.5: (a) The simulated ΔC per unit area (fF/mm^2) of the LC-SQ sensor for different areas and thicknesses. (b) The simulated ΔC over C_0 of the LC-SQ sensor for different areas and thicknesses. 112

Figure 4.6: The deformation of the polyimide sensor with a 25 µm thickness, under the pressure of 50 MPa. (a) Sensor with 25 µm edge size. (b) Sensor with 1 mm edge size. 113

Figure 4.7: (a) The layout of the tested polyimide pressure sensor. The estimated area is 20 mm^2. (b) The stack configuration of the polyimide pressure sensor fabrication process. 114

Figure 4.8: Photo of the polyimide sensor on an ELM3.0 flexible PCB. In this photo, the backside of the ELM3.0 PCB is facing up. 115

Figure 4.9: (a) The applied pressure and ELM3.0 recorded capacitance of the trial polyimide sensor during the high pressure test cycle. (b) The zoomed-in view of plot (a) at the pressure transition points. The pressure segments are illustrated in plot (b). 116

Figure 4.10: The applied pressure and the capacitance change of the trial polyimide sensor after baseline correction. 117

Figure 4.11: (a) The temperature and capacitance change during an ELM3.0 high temperature test, system A with RTI epoxy. (b) The temperature and capacitance change during an ELM3.0 high temperature test, system B with silicone mold. 119

Figure 4.12: The temperature and polyimide sensor capacitance change of an ELM3.0 system during a brine well test cycle. The capacitance changed by 5 pF under 1800 psi pressure and 70°C temperature. 120

Figure 5.1: The measured leakage current for NMOS transistors with different gate dimensions and temperatures. The leakage current increased by several orders of magnitudes when temperature increased from 25°C to 250°C [Sho89]. 124

Figure 5.2: (a) An example shows the MEMS switch as a power management unit for energy scavenging of light [Par12]. (b) Proposed power management system circuit schematic.......... 126

Figure 5.3: (a) An example of reconfigurable antenna implemented with RF MEMS switches [Erd07]. (b) The proposed architecture of the passive RFID system for wireless communication, with assistance from the RF MEMS switch network. 128

Figure A.1: (a) The photo of a high power DC-RF switch from the University of Michigan [Ozk12]. (b) The SEM image of a high power DC-RF switch from the University of California, San Diago [Pat12]. 132

Figure A.2: (a) Photo of the Raytheon MEMS capacitive MEMS shunt switch [Gol98]. (b) Photo of the University of Michigan low voltage MEMS shunt switch [Pac00]. (c) SEM of the University of Waterloo capacitive MEMS switch fabricated with the standard CMOS fabrication process. A wrapped-plate structure is used to enhance capacitance ratio [Fou10]. 134

Figure A.3: (a) The principle of dielectric charging of the RF capacitive switch. (b) SEM of RF switch designed at the University of Colorado with ALD Al_2O_3/ZnO as the dielectric layer [Her07]. (c) The side view of the dielectric RF switch proposed by the University of San Diego [Gri10]. 135

Figure A.4: (a) Fabrication process for the University of Michigan ALD packaging process. (b) The SEM photo of the cross section of the ALD package [An14]. 136

Figure A.5: (a) Top view of the proposed switch structure. (b) Cross sectional view along X-X'. (c) Cross sectional view along A-A' 139

Figure A.6: The bridge design for switches R-SP1 to R-SP3. The designs R-SP4 to R-SP6 are the same designs as R-SP1 to R-SP3 but with 0.5x dimensions. The designs R-SP2, R-SP3, R-SP5 and R-SP6 contain crab-leg shaped structures for in-plane stress release. 140

Figure A.7: (a) Deformation of bridge at 22.5 V voltage, right before pull-in. The design evaluated in the plot is R-SP1. (b) The bridge actuation voltage with different residual tensile stress, designs from R-SP1 to R-SP6 are included. 143

Figure A.8: (a) The setup for the stress analysis. (b) The simulation results for the stress analysis. The maximum stresses are generated at each corner of the bridge structure. The maximum stress generated with the pre-defined stress condition is 380 MPa. 144

Figure A.9: The simulation setup for analyzing the out-of-plane bending of the RF switch. 145

Figure A.10: (a) Deformation with +170 MPa stress in Si_3N_4 for design R-SP1. (b) Deformation with +170 MPa stress in Si_3N_4 for design R-SP2. 147

Figure A.11: The CPW line configuration used for the input and output ports of the RF switch. 148

Figure A.12: Origins of the lumped-element components from the physical structure of the switch. 149

Figure A.13: (a) The general lumped-element model for the series capacitive RF switch. (b) The lumped-element model for the series RF switch in this work, considering the fabrication process and the metal thickness of each layer. 149

Figure A.14: (a) Down state insertion loss for regular and small design sets of the switch, with 20 nm and 40 nm Al_2O_3 thicknesses. (b) Up state isolation for both design sets, with 1 µm and 2 µm gap distances. 151

Figure A.15: (a) The simulation setup for steady state temperature; the heat conduction in the substrate is the main heat transfer path. The ambient temperature is set as 20°C. (b) The device temperature distribution with sapphire substrate at 1W input power, regular-sized design. (c) The device temperature distribution with glass substrate at 1 W input power, regular-sized design. 153

Figure A.16: The baseline fabrication process flow for the RF switch. (a) (Mask 1) Lower metal deposition and patterning. (b) (Mask 2) First sacrificial α-Si deposition and patterning. (c) (Mask 3) Upper metal deposition and patterning. (d) (Mask 4) ONO-1 structural layer deposition and patterning. (e) (Mask 5) Second sacrificial α-Si deposition and patterning. (f) (Mask 6) ONO-2 structural layer deposition and patterning. (g) XeF_2 etching of the sacrificial α-Si from steps b and e. (h) ALD Al_2O_3 deposition. (i) Nitride and ALD Al_2O_3 deposition, sealing the ONO-2 device package. (j) (Mask 7) ALD Al_2O_3, nitride and ONO-2 patterning. 155

Figure A.17: (a) 3D profile of the switch contact area, first batch, R-SP1. The switch is bent downwards for 3 µm. (b) 3D profile of the switch contact area, second batch, R-SP1. The switch is bent upwards for 10 µm. 156

Figure A.18: (a) Cross-section view of the switch at A-A' plane, where the contact cantilever is located. (b) Cross-section view of the switch at B-B' plane, where the anchor is located......... 157

Figure A.19: (a) Top-down view photo of device R-SP4. (b) The photo of the RF switch die with angled view. 158

Figure A.20: The experimental setup for switch RF measurement. The two DC actuation pads are connected with the power supply, with 1 MΩ series resistors for dielectric breakdown protection and high isolation. The RF input and output pads are connected with the 0.1-26.5 GHz network analyzer with 50 Ω RF probes. 159

Figure A.21: (a) The measured S-parameter of device R-SP1 from the first batch of fabricated devices. (b) The measured S-parameter of device R-SP1 from the second batch. 160

Figure B.1: Schematic diagram of a typical RFID system [Sam08, Una11, Kha14, Ser15]. The transponder modulates and backscatters the RF signal for data transmission. 162

Figure B.2: (a) The photo of the NFC-RFID platform developed at the University of Washington [Zha15]. (b) The schematic of the miniaturized sensor and microfluidic channel developed at Boston University [Ser15]. (c) Chipless RFID tag fabricated at Monash University [Isl12]..... 164

LIST OF TABLES

Table 1.1: Comparison of communication methods [Web-Blu, Web-WiF, Web-Zig, Fin10]..... 17

Table 1.2: Design target of this dissertation. 17

Table 2.1: Major system components and their relevant features for target application. 25

Table 2.2: The MCU considered for the ELM system implementation. 26

Table 2.3: Overall design parameters of the ELM1.0. 40

Table 2.4: Testing solutions used in the HPHT tests in Total, France... 48

Table 3.1: Overall design parameters of the ELM2.0 system.. 56

Table 3.2: Testing solutions used in the ELM2.0 HPHT tests... 73

Table 3.3: The summary of the ELM3.0 drift rate from various tests. 90

Table 3.4: The estimated drift rate for the AEC C100 device under different testing condition.. 96

Table 4.1: The summary of the LC sensor names and simulation results. 113

Table A.1: The performance parameters of state-of-the-art RF switches. Both semiconductor and MEMS switches are included. 137

Table A.2: Geometry parameters for each design variation of the RF switch........................... 140

Table A.3: Summary of RF switch designs and their performances. 141

Table A.4: The actuation speed of RF switches at $V_s = 2V_p$. 145

Table A.5: Summary of out-of-plane bending distances at various Si_3N_4 stress conditions. 146

Table A.6: The extracted parasitic capacitance in the lumped-element switch model. 150

Table A.7: The simulated steady-state temperature at the switch contact point........................ 153

Table B.1: Comparison of state-of-the-art RFID tags and systems. 165

LIST OF APPENDICES

APPENDIX A: A MEMS High Power Tx/Rx Duplex Switch for Radio Transceiver Application 129

APPENDIX B: Literature Reviews on RFID Assisted Sensor Technology............................... 161

ABSTRACT

Downhole environmental monitoring can provide significant benefits to the petroleum industry. The rapid development of semiconductor technology enables autonomous sensing microsystems to operate at extreme environments. By injecting these microsystems into the boreholes and retrieving them after deployment, the geophysical conditions in the area of interest can be obtained. Challenges include high temperature, high pressure, miniaturized system size and packaging. This dissertation describes three generations of the environmental logging microsystem (ELM) for downhole geophysical logging applications.

The first generation of the microsystem, ELM1.0, is designed for temperature logging in downhole environments. Each system consists of a power management circuit, a microcontroller with an integrated temperature sensor, and optical indicators. The system electronics are integrated on a flexible printed circuit board and packaged in a steel shell. The ELM1.0 has a packaged size of 8.9×8.9×6.85 mm^3. It was tested at up to 125°C, 50 MPa in high salinity condition.

The second generation (ELM2.0 & ELM2.1) is upgraded from ELM1.0 by adding a micromachined capacitive pressure sensor for pressure sensing up to 50 MPa. The ELM2.0 & ELM2.1 systems are packaged in steel shells filled with transparent polymer for pressure transfer. The packaged systems have a dimension of 9.5×9.5×6.5 mm^3. The third generation (ELM3.0) is upgraded from ELM2.0 with a power switch and a low-cost polyimide pressure sensor for coarse pressure measurement up to 50 MPa. Both ELM2.0 and ELM3.0 systems were successfully tested at up to 125°C, 50 MPa in corrosive environments using laboratory instruments, and in a brine

well at a depth up to 1235 m. A progressive polynomial calibration method was used for interpretation of the pressure sensor data from these tests.

In addition, a high power micromachined RF switch for radio transceiver applications was designed, fabricated and tested. The RF switch can potentially be used to establish antenna networks for RF communication in the ELM. The switch consists of a bridge structure for electrostatic actuation and capacitive contact. The switch was fabricated with a 7-mask process. The fabricated device showed limited RF performance because of challenges related to the control of residual stress in suspended elements.

CHAPTER 1:

INTRODUCTION

1.1. Background and Motivation

Rapid growth in the developing world is increasing global demands for energy. Fossil fuels, which are formed by natural processes such as anaerobic decomposition of organic matter and primarily include coal, fuel oil and natural gas, are expected to remain as the primary energy source on earth [Ene10]. Currently, the amount of resources extracted from oil reservoirs is approximately 40% to 60% of the total available contents [Cha12]. Enhancing oil extraction efficiency while maintaining safety is an important goal for the fossil fuel industry. Downhole environmental monitoring can provide significant benefits to the petroleum industry. Knowledge of downhole geophysical conditions, such as temperature, pressure, and chemical concentrations in oil wells, hydraulic fractures, and reservoirs, can guide decisions governing operational efficiency and safety in exploration and production [Cha12, Ell07, Etn89, Tim85].

Well logging technology, which is the practice of sensing and recording downhole conditions, has been developed since the 1920s, and serves many functions in the petroleum industry [Ell07]. With a record of environmental parameters such as temperature, pressure and resistivity, subsurface geophysical mapping can be generated. Such maps help in the evaluation of the hydrocarbon production potential of a reservoir and in the refinement of the extraction strategy. One of the traditional oil well logging methods, wireline logging, is performed by

lowering a cable with instruments on the end of a wireline into an oil well. These instruments record the geophysical parameters using a variety of sensors (Fig. 1.1). The instruments are generally cylindrical devices with an outer diameter limited to 10 cm to accommodate the normal borehole dimension (15 cm). The lowering speed ranges from 180 m/hour to 550 m/hour and traditional sampling provides one averaged measurement for every 15 cm travel of the tool [Ell07]. The sensors on the instruments measure temperature, pressure, and resistivity in the wellbore. The spatial resolution of the measurements depends on the lowering speed of the wireline, and is typically on the order of several centimeters. Although wireline logging has been used for many years and has advantages of easy operation, multiple sensor integration and real-time data acquisition, there are important limitations. The primary limitation of wireline logging is that it can only provide geophysical measurements in spaces very close to the wireline. The environmental conditions of regions close to the wellbore can be detected through methods such as inductive sensing. However, the environmental conditions deeper in the reservoir remain unknown.

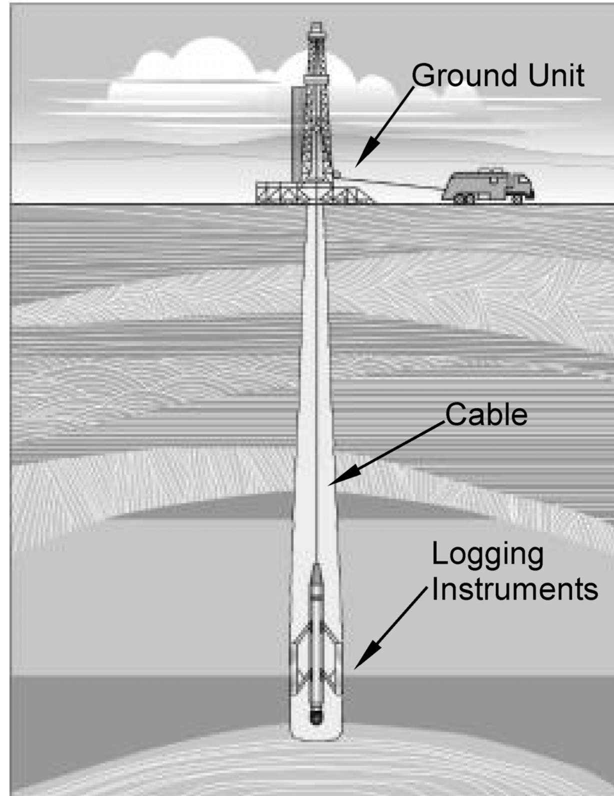

Figure 1.1: The principle of wireline logging. The wireline tool is lowered into the oil well for environmental monitoring [Ell07].

Cross-well electromagnetic or seismic imaging provides an alternative method for well logging with the detection range extending to the deep reservoir. Similar to wireline logging, this method uses instruments that are attached to cables. By lowering transmitter and receiver instruments into separate wellbores, electromagnetic waves with frequency from 10 to 100 Hz are transmitted between the transmitter and the receiver (Fig. 1.2(a)). As the transmitter is moved within the region of interest, the target zone is illuminated at several angles and the electromagnetic waves are received by the receiver at multiple locations (Fig. 1.2(b)). These waves are interpreted as geophysical parameters using appropriate algorithms. Currently, the nominal inter-well spacing is 300 m. Cross-well imaging has a maximum data resolution of 2% of the inter-well spacing,

which is ~6 m for nominal inter-well spacing [Sch06]. This spatial resolution is relatively low and the results are easily affected by underground environmental noise sources.

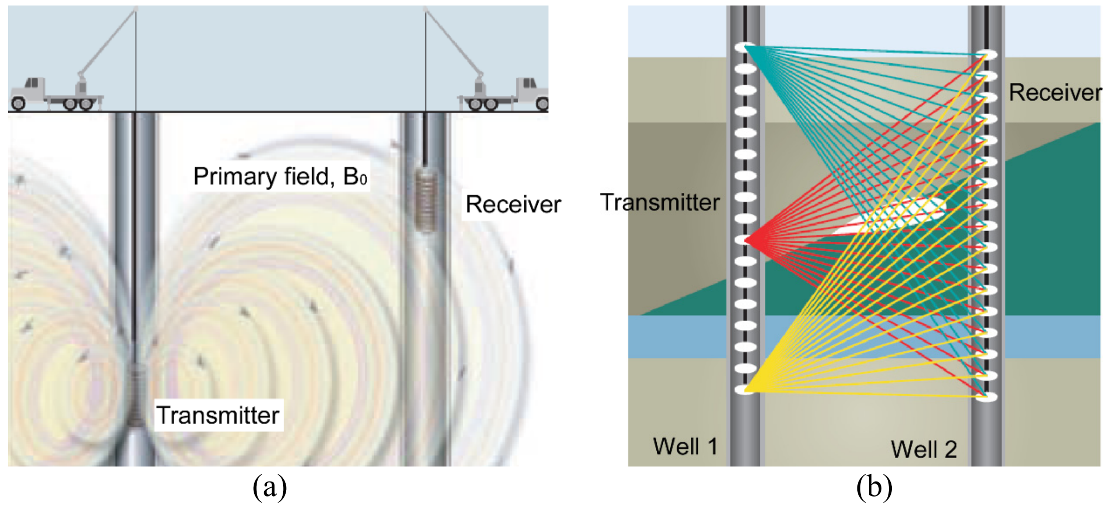

Figure 1.2: (a) The principle of cross-well electromagnetic imaging. The transmitter generates a primary electromagnetic field and the field is received by the receiver. (b) The operation of the cross-well imaging. The target zone is illuminated at several angles by moving the transmitter and receiver [Sch06].

The traditional well logging techniques discussed above mainly provide aggregate information with limited spatial resolution. It is envisioned that the traditional methods of illuminating the downhole environment can be augmented by the widespread deployment of autonomous sensing microsystems. Clusters of such microsystems can be used to enhance the spatial resolution of the sensed parameters, reaching locations in narrow confines and away from the wellbore. Figure 1.3 illustrates a potential application scenario. In this scenario, the microsystems are sensing and logging data while being transported by fluid flow along the wellbore and the fractures. In the long term, the microsystems could be envisioned to acquire time stamped data on temperature, pressure, chemical environment, geolocation, etc. Following the data collection, the systems would be retrieved with the return fluid, and wirelessly interrogated at close proximity in a controlled environment [Cha12].

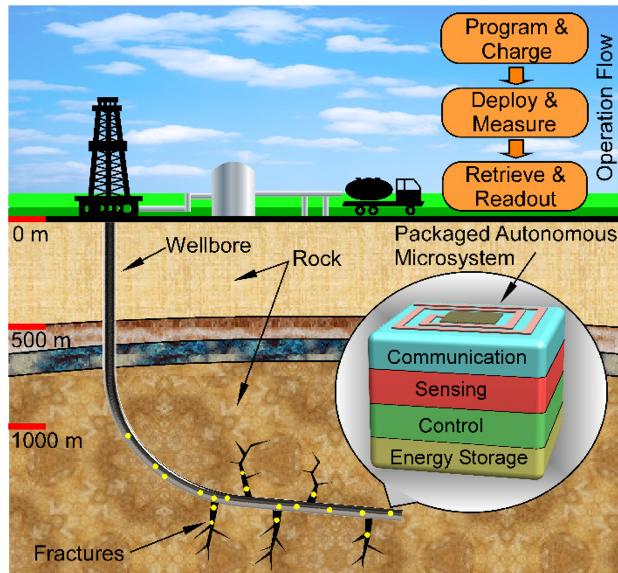

Figure 1.3: A typical application scenario of the autonomous sensing microsystems in the downhole environment.

At a depth of 3658 m (12,000 feet) in a typical reservoir, the temperature can reach 125°C, the pressure can range from 7-41 MPa (1000-6000 psi), and the chemical environment can have salinity levels from 50,000-150,000 ppm [Cha12]. In many other situations, the temperature and pressure may exceed 150°C and 70 MPa (10,000 psi). This proposed microsystem should work at the downhole temperature and pressure, and endure the high salinity. Very limited work has been reported on microsystems for downhole environmental monitoring. Openfield™ Technology has developed a temperature and pressure recorder packaged in a Φ50.8 mm spherical titanium shell that can flow in well pipes for downhole monitoring [Ope13]. Additionally, a research prototype using customized electronic chips encapsulated in a Φ7.5 mm polymer sphere has been reported for temperature and pressure measurements in oil wells [Yu12, Shi15].

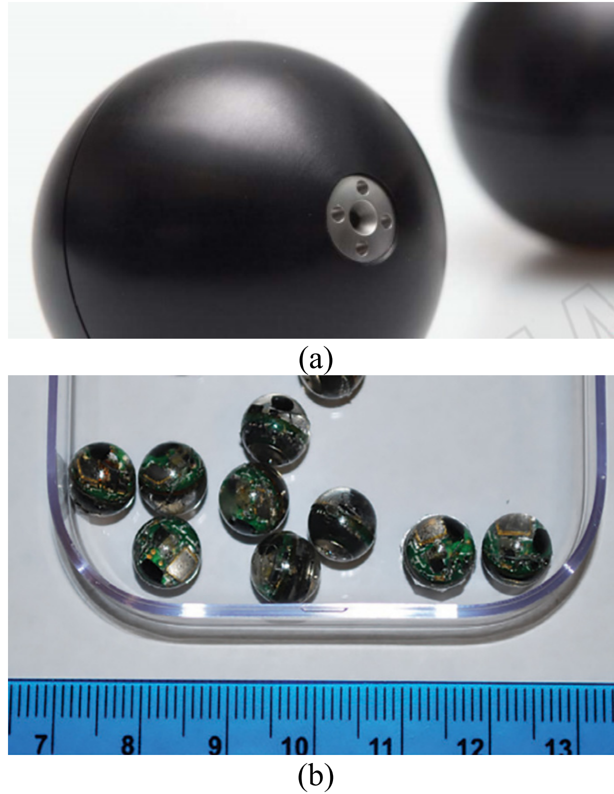

Figure 1.4: (a) The downhole smart ball developed by Openfield^{TM} Technlogy, which has a diameter of 50.8 mm [Ope13]. (b) The downhole sensor developed by University of Tulsa and Saudi Aramco, with a diameter of 7.5 mm [Shi15].

The proposed microsystem can either use electronic chips that are designed at the transistor level for targeted elevated temperatures, or use commercial CMOS electronic chips rated for operation in nominal temperature range (25-85°C). Whereas commercial electronics offer flexibility, the challenge lies in identifying the failure modes at the intended operating temperature and then developing the appropriate hardware and software solutions. There are many packaged commercial electronic chips with millimeter-scale footprint that are potential candidates for the microsystem, offering functionalities of computing, data storage, sensing, communication and power regulation. These chips can be assembled onto a flexible PCB using a commercial service. This reduces the overall cost and allows higher design flexibility and higher reliability. Although not designed for target temperatures in typical downhole environments, commercial chips can be

stressed in reliability tests that exceed the datasheet specifications, and configured to have the capability to operate at over 125°C if arranged in appropriate configurations. In section 1.3, the temperature dependence of the reliability of CMOS electronics is presented.

The temperature sensor and pressure sensor used in the proposed microsystem can either be custom designed for the target high temperature, high pressure, and small footprint, or obtained from commercial vendors. The silicon-based CMOS temperature sensors are usually integrated in the commercial microcontroller unit, and have adequate performance for this application. For pressure sensors, the commercially available miniaturized pressure sensors are usually targeted at pressures near atmospheric pressure [Mur15], and cannot be used for downhole applications. As a result, a custom designed pressure sensor is needed to achieve the required dynamic range and footprint.

Motivated by the needs described above, this work focuses on the development of an autonomous microsystem for downhole environmental logging. The sensor platform developed in this effort, named the environmental logging microsystem (ELM), is a miniaturized electronics system composed of microfabricated sensors, commercial interface electronics, a power source and embedded software. The microsystem is designed to survive the downhole environment of ≥125°C and ≥7200 psi in corrosive environments, and record temperature and pressure data. In the following sections of this chapter, Section 1.2 describes the challenges involved in developing the microsystems for downhole application. Section 1.3 provides the theoretical background of electronic failure rates at stressed temperature conditions, and the reliability analysis of the C8051F990 MCU used in the ELM system. This is followed by Section 1.4, which summarizes the communication methods for microsystems. Section 1.5 provides a summary of the goals and challenges of this work. Section 1.6 describes the organization of the rest of the dissertation.

1.2. Challenges of Microsystems for Downhole Applications

As stated above, autonomous sensing microsystems with data logging capabilities can reach locations away from the wellbore and provide high spatial resolution. However, several challenges exist in the implementation of these systems. The high temperature is the primary challenge to the electronics and battery components, as it leads to electronic malfunction and battery degradation. The high pressure and the required small footprint of the microsystem present challenges for the pressure sensing element as well as the interface electronics. Such high pressure exceeds the dynamic ranges of all readily available commercial pressure sensors, which typically target pressures near atmospheric pressure. The high pressure can also potentially damage the bonds between the pads of the electronic chips and circuit boards. The environmental conditions also demand special considerations for system packaging to protect the electronics, which has been addressed in [Ma16] and is not a topic in this dissertation.

The high temperature presents the primary challenge to electronics. In the downhole environment, the electronics and the battery of the microsystem must survive above 125°C, and above 150°C in certain circumstances [Wat12]. However, silicon-based CMOS transistors, which are the building blocks of modern digital computing and control electronics, have leakage currents that increase exponentially with temperature. For a regular CMOS transistor, there are three main leakage paths: reverse-biased PN junction leakage, subthreshold leakage and gate leakage. Among these paths, the reverse-biased PN junction leakage current has the highest dependence on temperature (Fig. 1.5(a)) [Roy03]. This current mainly consists of the diffusion current and the recombination-generation (R-G) current [Pie96, Roy03, Cla92]. It can occur in two paths: from the substrate to the transistor wells, and from the wells to the source or drain of transistors. At elevated temperatures, the diffusion current dominates and is given by [Pie96]:

$$I_{Diffusion} = I_s[exp(\frac{qV}{kT}) - 1] \quad (1.1)$$

where I_S is the reverse bias saturation current, q is the magnitude of the electronic charge, V is the reverse bias voltage, k is the Boltzmann constant and T is the junction temperature in Kelvin. In this equation, I_S has a mild dependence on temperature, while the primary temperature dependence comes from the exponential term. The consequence of the enhanced leakage is most significant for the memory circuit block. According to published experimental results, the leakage current of a memory circuit increases by 2,000-10,000× when the temperature increases from room temperature to 125°C [Wat12, McC12, Wol12, Sho89]. This leakage current substantially increases the average power consumption. This raises concerns about available energy and system lifetime. Furthermore, a high leakage current affects the performance of the electronics and leads to reliability issues, which are discussed in Section 1.3.

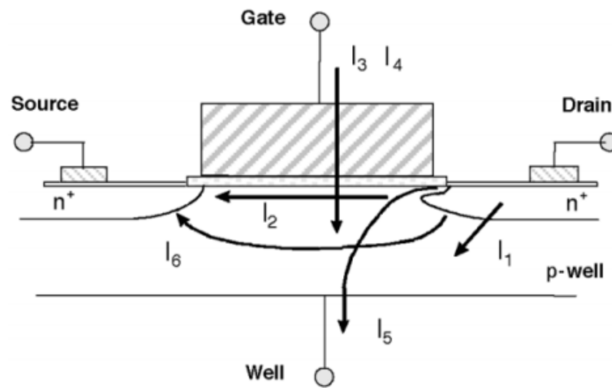

Figure 1.5: Leakage path for a typical NMOS transistor. The three main leakage paths are reverse-biased PN junction leakage (I_1), subthreshold leakage (I_2) and gate leakage (I_3, I_4) [Roy03].

The operating temperature is a challenge for the battery as well. The use of rechargeable batteries can potentially allow the microsystems to be re-used. Lithium batteries are attractive for this purpose. Lithium batteries can provide high energy density and, in principle, can be used at temperatures as high as 250°C [Hen98, Caj13, Muñ07]. However, there are very few options that

are commercially available with mm-scale footprints, and none of these are rated at temperatures exceeding 100°C. A Seiko MS412FE battery has a Φ4.8 mm footprint and 1 mAh capacity, and is rated up to 60°C [Sei13]. When used at temperatures beyond the specifications, the electrolyte inside the battery will degrade, which will adversely affect battery performance, reduce battery lifetime, and may even cause chemical hazards such as leakage or explosion [Hen98, Dou12, Rob97]. Thin film solid state lithium batteries can operate at temperatures up to 125°C and can be integrated on mm-scale silicon chips. However, this form factor compromises energy density; for example, the EnerChip CBC001-BDC thin film battery has only 1 μAh capacity on a 1.375×0.85 mm^2 bare die [Cym14]. This cannot even power a typical commercial microcontroller unit (MCU) in deep sleep state consuming a few μA, and is, therefore, not a candidate for the system.

The high pressure in downhole environments presents an additional challenge for the pressure sensing element. Although various types of MEMS pressure sensors have been explored in the past five decades, most have been intended for operating near atmospheric pressure. Many of the MEMS pressure sensors are built upon one of two sensing principles: piezo-resistive and capacitive [Eat97, Gia06, Kum14]. Compared with piezo-resistive pressure sensors, capacitive pressure sensors can achieve further miniaturization because of the absence of on-chip resistors. With a smaller footprint, a higher pressure dynamic range can be achieved due to the higher stiffness of the sensing diaphragm. However, this increased stiffness reduces the capacitance change, which limits the pressure sensing resolution and adds additional requirements for the capacitance readout module's accuracy. A capacitive pressure sensor that can operate at 50 MPa with a reasonable capacitance change is being developed at the University of Michigan under a separate effort [Ben17]. Meanwhile, the pressure sensor signals need to be picked up by the

electronics. The pressure sensor can be either placed on the exterior of the system package and connected with the electronics using through the package vias, or directly assembled on the circuit board of the electronics inside the package. The first approach introduces a high parasitic capacitance due to the long lead transfer between the sensor and the readout electronics, and the fabrication and assembly process are difficult. The second approach requires appropriate packaging techniques for transferring the pressure to the sensor and electronics with low attenuation, while not affecting the operation and communication reliability of the electronics.

The miniaturization of the system presents another design challenge. A small size is desirable because one of the goals is to permit the microsystem to reach into hydraulic fractures that are created to increase fluence around a well. For this work the overall system size constraint is specified as 1 cm, including packaging, sensors, electronics and battery. Advancement in semiconductor technologies has allowed complex electronics to be placed on a chip die of a few millimeters size. Integration of these electronics within a small form factor requires a specific layout of the printed circuit board (PCB) and assembly techniques.

The high pressure (≈50 MPa) and high salinity (concentrated brine) require specific packaging techniques. As noted above, since the pressure is transferred onto the printed circuit board, the packaged commercial electronic components should operate normally under the high pressure. The package should allow for radio-frequency (RF) or optical communication between the microsystems and the external reader for triggering and data readout. These packaging considerations have been addressed in our recent work on sub-millimeter packages for microsystems in downhole environments [Ma15]. In that effort, the package has a dimension of 0.8 mm^3, and survived >48 h in American Petroleum Institute (API) standard brine (with 8 wt%

NaCl and 2 wt% $CaCl_2$ in deionized water) at 80°C, and subsequently, in 50 MPa of hydraulic pressure. The size of this mm-sized package can be adapted to fit the ELM.

To summarize, a variety of challenges exist and solutions are being developed gradually, with advancements in multiple engineering fields including semiconductor physics, battery technology, sensor technology and packaging technology. To overcome these challenges and demonstrate functioning systems, the reliability of each component under the target environment conditions is critical. Compared with the components that are still under development or investigation in research labs, the off-the-shelf components provide superior yield at nominal conditions. Although in certain circumstances those components are not rated for target operating conditions, they are still preferable considering the full suite of tests at nominal conditions performed by the manufacturer. Thorough electrical tests of these components at the target temperature is required before integration into the system.

1.3. Electronics Failure under Stressed Condition

As stated in the preceding section, silicon-based CMOS integrated circuits suffer from increased failure rates at elevated temperatures. Such increased failure rates could cause the autonomous sensing system to record incorrect data or even fail during deployment in oil wells, thus must be considered during system design. In general, there are several failure mechanisms that dominate the electronics failure rates, such as surface charge accumulation, dielectric breakdown, electromigration, bonding and packaging leaks. Surface charge accumulation and dielectric breakdown are associated with the silicon-oxide interface. The gate oxide in modern CMOS circuits is on the order of nm thick and will be thinner in the future. During handling of the devices, a voltage higher than the breakdown voltage may be presented and cause the oxide to breakdown. The majority of the excessive voltage arises from triboelectricity (i. e., electricity

produced by rubbing two materials together), which can easily damage the circuit. The electromigration usually occurs at the metal contact between separate metal layers, and can eventually cause the loss of metal connections, and circuit failure. Bonding and packaging failure is usually caused by the fabrication process and ambient environment [Sze88].

Many of these failure mechanisms are chemical processes, and the reaction rates of these processes are accelerated by temperature with exponential relation. The reaction rate R of the temperature acceleration process is governed by the Arrhenius equation [Sze88]:

$$R = R_0\, exp(-E_a / kT) \tag{1.2}$$

where E_a is the activation energy of the specific process, k is the Boltzmann constant (8.6×10^{-6} eV/K) and T is temperature in Kelvin. This equation is widely used as a formula for the temperature dependence of reaction rates in the chemical field. From Equation (1.2), the acceleration factor A_f, which is the ratio of the two amounts of time to failure at two different temperatures, is given by [Sze88]:

$$A_f = \frac{t_1}{t_2} = Exp(\frac{E_a}{k} \times (\frac{1}{T_1} - \frac{1}{T_2})) \tag{1.3}$$

where t_1 is the failure time at temperature T_1, and t_2 is the failure time at temperature T_2. From Equation (1.3), it can be easily seen that $t_1 < t_2$ for $T_1 > T_2$, which indicates that the reaction is faster at higher temperatures.

Silicon Laboratories, Inc. (Austin, TX) provides the failure test results of the 0.18 μm CMOS process with embedded flash in their quality and reliability report [Sil15]. This process is the fabrication process for C8051F990 MCU, which is the control unit of the autonomous system developed in this effort. The activation energy E_a for this process is characterized to be 0.7. During the tests, many chips were evaluated with a total device hour (number of devices × total

hours) of 4,741,000 with zero failure. Based on the test results, the failure in time (FIT), which represents the estimated number of failures in a billion hours of operation, is obtained by [Cor12]:

$$FIT \geq \frac{\chi^2(\alpha, 2k+2)}{2 \times A_f \times D \times H} \times 10^9 \tag{1.4}$$

in which χ^2 is the chi-square distribution function, α is the confidence level of the estimation, k is the number of failures observed in the tests, A_f is the acceleration factor under different temperatures and $D \times H$ is the total tested device hours. Figure 1.6 shows the FIT curve of this process at 20-180°C with α = 90%. In the integrated circuit community, an FIT of 100 is usually recognized as a maximum tolerable value, which is reached at 115°C in this plot. Since the ELM system developed in this work is targeted at 125°C, a FIT higher than 100 is expected for the microcontroller. This indicates a higher chance that electronics failure could occur, and full system characterization is required at the target high temperature.

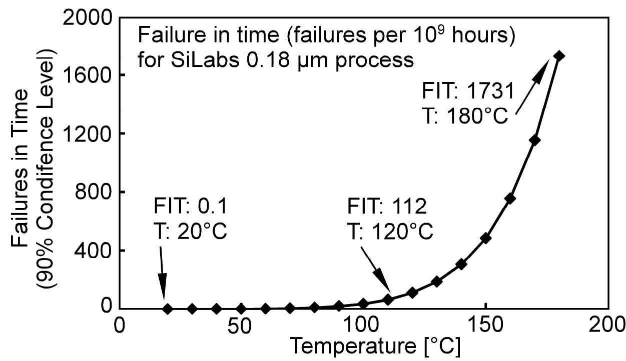

Figure 1.6: The failure in time (FIT) for the Silicon Laboratories 0.18 µm process with embedded flash over temperature. The increase of FIT at elevated temperatures results from temperature acceleration of several failure mechanisms, such as surface charge accumulation and charge injection [Sze88, Ohr98].

1.4. Communication Methods for Microsystems

The communication module of the autonomous microsystems is mainly used for system control, data sharing, and data retrieval after deployment. For the proposed well logging

applications, communication will be used to wake up the microsystem from deep sleep mode, trigger the system into different functional states, and change system parameters such as the measurement time interval or data resolution. The communication module is also necessary for reporting data, which must be performed in a reliable and efficient manner that consumes low power. In this section, challenges in the development of the communication module are discussed first. Then three communication methods are proposed and compared, including optical communication, active RF communication and passive RF communication. Table 1.1 lists the advantages and drawbacks of these communication methods. A detailed literature review on one type of passive RF communication method, the radio-frequency identification (RFID), and its application in microsystems, is presented in Appendix B of this dissertation.

Because the reservoirs contain high salinity brine solution, in which the electromagnetic waves are highly attenuated, sensor nodes cannot communicate through RF means in the downhole environment [Ser15]. As a result, communication must occur before deployment and after retrieval. To fit in the targeted small dimension of the ELM, the communication hardware should have a small size. Optical communication can be achieved via miniaturized LEDs. For RF communication, a miniaturized antenna is required; thus, the RF signal frequency must be increased to permit the antenna efficiency to be acceptable. The communication power should be minimized to fit the low power system design.

Three types of communication methods are widely used in sensing microsystems: optical, active RF, and passive RF communication. Optical communication usually uses an LED or a lamp transmitter, a channel that allows light transmission, and a photodiode receiver. Optical communication based on high power LEDs has been demonstrated in an underwater environment with communication distance >1 m [Par09]. Compared with RF, optical communication is easier

to implement with miniaturized components. The communication distance is usually limited by the power level of the LEDs. Ambient light contributes to high white noise, thus a dark environment is preferred.

Active RF communication uses radio-frequency electromagnetic waves to transmit signals. The electromagnetic waves are transmitted via antennas between the transmitter and receiver, and devices on both sides consume power. Active RF communication is widely used in modern local area network (LAN) and personal area network (PAN) where electronics share information with each other. The data are transmitted among the wireless modules following certain protocols. Popular protocols include Bluetooth, ZigBee and Wi-Fi, which have been used in many commercial products [Web-Blu, Web-WiF, Web-Zig]. Devices supporting these protocols have high data transmission rates and distances, but their power consumption is high for microsystems application.

Passive communication uses electromagnetic waves to convey information as well. However, instead of powering itself, the receiver in the microsystem harvests energy from the external transponder and uses backscattering to send information back. It does not require an integrated power source and has moderate communication speed, which are suitable for sensing applications. One major passive communication category is RFID. The RFID module is usually composed of an interrogator and a passive tag. The interrogator is a read/write device which is used for transponder data capturing and data writing on some occasions [Fin10]. To date, integrated RFID chips have been manufactured in large quantities. These chips have been implemented in real-time sensing microsystems and are discussed in Appendix B.

Table 1.1: Comparison of communication methods [Web-Blu, Web-WiF, Web-Zig, Fin10].

Communication Method		Read Range	Data Rate	Power Consumption	Comment
Optical		Usually < 1 m	Slow	High	Easy to implement, short distance
Active RF	Bluetooth	<10 m	1-3 Mb/s	High	Short distance, high power
	ZigBee	10-100 m	20-250 Kb/s	Medium	Long distance, moderate power
	Wi-Fi	20 m indoor	6-54 Mb/s	High	Medium distance, high data rate, high power
Passive RF: RFID		<5 m	kB/s	Low	Short distance, low power for microsystem

1.5. Goals and Challenges

The overall goal of this dissertation is to develop an environmental logging microsystems (ELM) for downhole environmental sensing. The microsystem should record temperature and pressure up to 125°C and 50 MPa in corrosive solution. The microsystem should be able to communicate with an external readout unit for system control and data readout. The system should be ≤1 cm^3, including sensors, electronics, battery and packaging. The system lifetime under 125°C in the detection state should exceed 12 hours for a full deployment event. Table 1.2 summarizes the design target of this dissertation.

Table 1.2: Design target of this dissertation.

Parameter	Target
Pressure	≥50 MPa (7,250 psi)
Temperature	≥125°C
Chemical	API standard brine (8 wt% NaCl and 2 wt% $CaCl_2$); Additional exploration: Hydrocarbons represented by Isopar^{TM}-L.
System Size	≤1 mm^3
System Lifetime	≥12 hours

Several challenges have to be addressed to meet the goals. The first design challenge is the high temperature, which lead to electronics malfunction and battery degradation. The second design challenge is the high pressure, which requires a specific pressure sensor element design and a sensor integration strategy with the ELM system. The third challenge is the required small footprint of the electronics. The fourth challenge is an appropriate packaging method that can protect these electronics and transfer the external pressure onto the electronics, which has been addressed in [Ma16].

To address these challenges, several specific goals have been formulated. The first specific goal is to design a microsystem platform that can achieve the temperature logging function up to 125°C, 50 MPa in a corrosive environment. The system should be wirelessly recharged when the battery voltage is low, and it should be able to wirelessly communicate with the external readout unit. The lifetime of the system should be ≥12 hours. Challenges of achieving this goal include identification and mitigation of failure mode in the electronic using hardware solutions, development of a state machine that accommodates the battery degradation, and design of a flexible PCB that permits compact 3D fold of the system into the necessary form factor. Efforts toward this goal are described in Chapter 2.

The second specific goal is to embed a pressure sensor within the system, and to adapt the electronics, packaging and firmware as necessary. The embedded readout electronics of the pressure sensor should operate under the target temperature and pressure of 125°C and 50 MPa. In this system, the electronics and battery are not protected from the applied pressure. Challenges include the calibration and interpretation of the pressure sensor readout. Efforts toward this goal are described in Chapter 3.

The third specific goal is to investigate a low cost polyimide sensor (LC sensor) that can potentially measure pressure up to 50 MPa. This LC sensor could be directly fabricated on the flexible PCB of the ELM system to reduce the manufacturing and assembly cost and improve yield. Challenges include the limited sensitivity of this sensor structure, the large parasitic capacitances that add up to the sensor readout, and the high temperature dependency of this sensor and the readout interface. Efforts toward this goal are described in Chapter 4.

A separate specific goal is to design an RF capacitive MEMS switch that can handle up to 1 W of transmission power at 2 GHz. This switch should have a low pull-in voltage, fast switching speed, and be hermetically packaged. This RF switch could potentially be used as an element of an antenna network for ELM passive communication. Efforts toward this goal are described in Appendix A.

1.6. Organization of the Dissertation

Three generations of ELM systems have been designed and fabricated. In the following sections of this dissertation, Chapter 2 describes the first generation of ELM (ELM1.0) for downhole temperature logging applications. The system is implemented with commercial electronics and a custom encasement for packaging, and the hardware and the software implementation of the system is explained in detail. The system is assembled on a flexible PCB and packaged in a sapphire on steel package. The packaged system has a dimension of $8.9\times8.9\times6.85$ mm^3. The system was successfully tested at 125°C, 7200 psi in corrosive solutions for more than 1 hour. The maximum characterized system lifetime is 6 hours under 125°C in hot sands. The highest temperature the system survived was 150°C with battery connected. The limitations in this first generation of the system include: (1) the ambient pressure is not transmitted

into the system, and thus cannot be measured; (2) the batteries must be attached immediately prior to deployment in order to extend the system shelf life.

Chapter 3 describes two new generations of the ELM (ELM2 and ELM3). There are two variations of ELM2 systems. ELM2.0 includes everything in ELM1.0, plus the pressure sensing capability. A micromachined pressure sensor is integrated into the system for pressure measurement up to 50 MPa. In addition to the pressure sensor, the ELM2.1 system adds an inertial measurement unit for potential use in geolocation tracking. The ELM2.0 and ELM2.1 systems are packaged in steel shell filled with transparent polymer for pressure transfer while not affecting communication. The packaged system has a dimension of 9.5×9.5×6.5 mm^3. The systems were successfully tested up to 125°C, 7200 psi for 3 hours, and at a reduced temperature of 100°C for 13 hours. The third generation of the ELM (ELM3.0) is also presented in this chapter; in addition to ELM2.0 components, it adds a slide switch that allows the battery to be integrated when the electronic system is assembled, and a low cost polyimide pressure sensor for coarse measurement of pressure. Both the ELM2.0 and ELM3.0 systems were successfully tested in a brine well with a depth of 1235 m. The results were presented in this chapter.

Chapter 4 describes the concept and preliminary study of the LC polyimide pressure sensor for potential downhole pressure monitoring. This low cost sensor can be directly fabricated on the ELM printed circuit board, with two large metal plates as the sensing electrode, and the sandwiched polyimide as the dielectric. Preliminary FEA was performed on sensors with different geometries and sizes, and the results show that the ΔC of a 20 mm^2 polyimide sensor over 0-50 MPa can achieve 165 fF. A trial polyimide sensor used for initial tests was designed and fabricated on the ELM3.0 system. The high pressure test of this trial device indicated that a capacitance change of 205 fF can be observed under 0-50 MPa hydrostatic pressure, while a large capacitance

drift was monitored. The sensor output has a high dependency on temperature, which is unexpected and limited the sensor usage at high temperatures.

Chapter 5 describes the future work and two other efforts are proposed: (a) a power management system using DC MEMS switches for leakage current reduction; (b) a miniaturized antenna network built with RF MEMS switches for passive communication of the system. The challenges of the proposed work include integration of the switch component into the system, the control methods for the DC MEMS switch and the design and implementation of the antenna network.

In Appendix A, the study of a high power MEMS switch for RF communication applications is presented. A capacitive switch with fixed-fixed actuation bridge is designed. The bridge is made of Oxide-Nitride-Oxide (ONO) and the dielectric material is atomic layer deposition (ALD) of Al_2O_3. The estimated pull-in voltage is 22 V. The simulated insertion loss is 0.2 dB and isolation is 20 dB at 2 GHz. The switch is hermetically packaged with an ONO shell and sealed with ALD Al_2O_3. The device was fabricated and a large in-plane deformation of the diaphragm was observed, which greatly degraded the RF performance of the switch. Stress compensation experiments have been tried to flatten the ONO bridge, and the results are presented.

In Appendix B, a literature review of RFID technology is provided. The review describes the existing RFID standards and the systems implemented with these standards, especially in the autonomous sensor area.

CHAPTER 2:

AUTONOMOUS MICROSYSTEM FOR DOWNHOLE TEMPERAUTRE LOGGING

This chapter describes the implementation and testing of the first generation of the ELM system (ELM1.0). This system is designed for temperature logging in high-temperature, high-pressure and high-salinity downhole environments. The system uses the smallest suitable off-the-shelf electronic and battery components that are compatible with assembly on a flexible printed circuit board. The folded size of the ELM is 6.5×6.3×4.5 mm^3. A special configuration is used to facilitate operation at elevated temperatures. During the system operation in the detection state, the system wakes up every 2 minutes from the deep sleep state to take temperature measurements and store the data in the MCU flash memory. During the post-deployment interrogation, the measured temperature data is optically reported to a laptop computer through a readout box. The ELM1.0 was packaged in a hollow stainless steel shell with a sapphire lid. The encapsulated systems were successfully tested at temperature and pressure reaching 150°C and 10,000 psi (exceed the target values), in environments of concentrated brine (American Petroleum Institute standard formulation), oil (Isopar®-L), and uncured cement slurry.

2.1. System Hardware

The block diagram of the ELM1.0 is shown in Fig. 2.1. The microsystem consists of an MCU, a solar cell, a charging circuit, two LED indicators, and a 3 V miniature rechargeable lithium battery. The MCU has an integrated temperature sensor. The MCU is also responsible for

functional control, data storage and communication, and system power management. The solar cell is used for wireless charging of the lithium battery, optical triggering of the system functions during testing and post-deployment interrogation. The charging circuit assists the wireless charging of the battery using the solar cell. The wireless charging occurs when the solar cell is continuously exposed to bright light from an external light source. For optical triggering, the solar cell is exposed to an external light source that generates predefined light pulse patterns. This results in corresponding voltage pulses from the solar cell. These voltage pulses are picked up by a comparator embedded within the MCU. Different pulse patterns trigger the MCU into different functional states, such as states for temperature detection, data reporting, etc. The measured temperature data during a testing cycle are stored in the flash memory integrated in the MCU. These data are encoded with a cyclic redundancy check (CRC) algorithm for transmission error detection. The data and the CRC verification bytes are transmitted optically through the two LED indicators controlled by the MCU. An external control/readout system based on Labview™ program is built for interaction between the microsystem and client. The functions of this control system include generating the optical triggering pulses and receiving the optical signal generated by the LEDs.

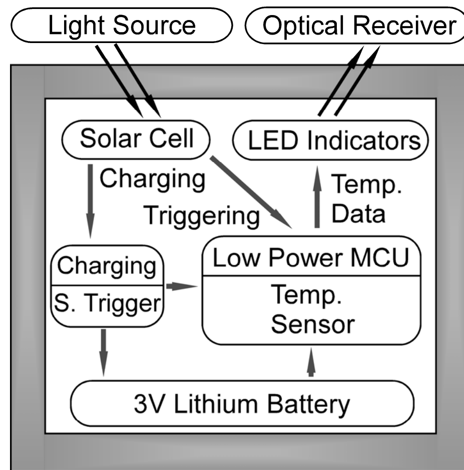

Figure 2.1: The block diagram of the ELM1.0. The system consists of a solar cell for charging, two LED indicators for data reporting, a low power MCU for system control and temperature sensing, a charging circuit for wireless charging, a Schmitt trigger for charging protection and a 3 V lithium battery for energy storage.

The ELM1.0 circuit consists of a charging circuit block for the power supply, a Schmitt trigger block for charging protection, an MCU for temperature measurement, data processing and data storage, and two LED indicators for data reporting (Fig. 2.2). All components in this circuit are commercially available from electronic element distributors such as Digi-Key Corporation. The general rules for selecting the components, listed in the sequence of preference, include small footprint, low power consumption, integrated functionality, and low unit price. Table 2.1 summarizes the selected major components of the system circuit and their relevant features for the target application.

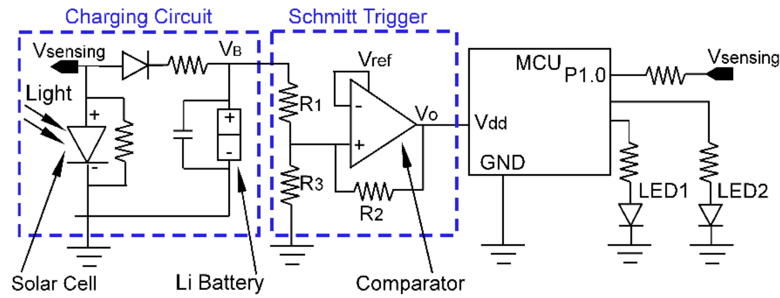

Figure 2.2: The schematic of the system circuit of ELM1.0. It consists of a charging circuit block, a Schmitt trigger block, an MCU and two LED indicators.

Table 2.1: Major system components and their relevant features for target application.

Component	**Part No.**	**Footprint**	**Device Feature**
MCU	Silicon Labs C8051F990	3 mm × 3 mm	0.8 µA sleep mode current, 80 µA active current (RT), 32 kHz internal oscillator, integrated temperature sensor
Battery	Seiko Instr. MS412FE	4.8 mm diameter	1 mA·h capacity, 100 µA maximum continuous discharge current
Solar cell	IXYS CPC1822	5.8 mm × 5 mm	4.2 V nominal output voltage, 50 µA nominal output current
Comparator for Schmitt Trigger	TI TLV3012	2.4 mm × 2 mm	2.8 µA static current, integrated 1.2 V internal reference voltage

2.1.1. Silicon Labs C8051F990 MCU

For this work, the C8051F990 low power microcontroller (MCU) from Silicon Laboratories, Inc. [Sil11] is selected over other options. This MCU has an integrated temperature sensor, an integrated capacitive sensing module, a small footprint of 3×3 mm^2 and low power consumption (e.g. 80 µA in the active mode and 0.8 µA in the sleep mode) at room temperature. Other MCUs that were also considered include Freescale KL03, Atmel Attiny20 and TI MSP430 series. Table 2.2 compares the key parameters of some of these MCUs. After a system is assembled and packaged, optical communication is used to interact with the MCU. The output of the solar cell is fed into the high-impedance comparator input pin (MCU P1.0) of the MCU for this purpose. The MCU stays in the sleep mode until it is awakened into the active mode and

triggered into different operation states by voltage pulses from the solar cell. Temperature measurements are made using the internal temperature sensor. The measured temperature data are stored in the flash memory and are optically transmitted through two LED indicators when requested by the exterior control/readout system.

Table 2.2: The MCU considered for the ELM system implementation.

MCU Part Number	Si Labs C8051F990	Freescale KL03	Atmel ATtiny20
Operating Temp.	-40 to 85°C	-40 to 85°C WLCSP / -40 to 105°C QFN	-55 to 125°C
Power Consumption	Core Power Consumption 82 μA at 32 kHz ADC Power Consumption: 370 μA (low power mode) Sleep Mode Power Consumption: 0.6 μA	Run Power Consumption: 50 μA/MHz Static power consumption as low as 2.2 μA	Active mode: 200 μA at 1MHz Idle mode: 25μA at 1 MHz Power-down mode: < 0.1μA ADC: 200-400 μA
Footprint	3×3x0.55 mm^3	2.0x1.61x0.56 mm^3 / 3x3x0.65 mm^3	1.55x1.41x0.538 mm^3
Package	QFN20	WLCSP / QFN	12-WLCSP
Volt. Supply	1.8 - 3.6 V	1.71 - 3.6 V	1.8 - 5.5 V
Clock sources	- Internal 24.5MHz High Power Oscillator (300 μA) - Internal 22 MHZ Low Power Oscillator(100 μA) - Internal 16.4 kHz RT Oscillator(< 1 μA) - External Clock	- 48 MHz high accuracy internal clock - 8/2 MHz low power internal clock - 32 kHz to 40 kHz crystal oscillator - 1 kHz LPO clock	- Internal 128 kHz clock - Internal 8 MHz clock - External clock
Temperature Sensor	Yes	Yes	Yes
Memory	8 KB Flash, 512 byte RAM	32 KB Flash, 2KB RAM	2 KB Flash, 128 byte RAM
ADC	12 bit	12 bit	10 bit
Capacitive Sensing	Yes (1 fF resolution, 45 or 500 pF max load)	No	No (capacitive touch sensing library available)
Unit Cost (for 1 pc / 5000 pcs)	$0.97 / <$0.89	$2.308 / $1.703	$1.50 / $0.655

2.1.2. Charging Circuit Block

The charging circuit block includes a Seiko Instruments MS412FE rechargeable lithium battery for energy storage, an IXYS CPC1822 solar cell for wireless optical charging, a rectifier diode to prevent the reverse flow of the charging current, and a protection resistor $R_{protect}$ to limit the charging current. A voltage is generated when the solar cell is exposed to external light. This results in a current flowing from the solar cell, through the rectifier diode and the protection resistor, into the battery for charging.

The MS412FE battery uses silicon oxide as its anode and lithium manganese composite oxide as its cathode. This battery has a high capacity (1 mA·h) and a small form factor (Φ4.8 mm×1.2 mm). The specified operating temperature for the battery is -20°C to 60°C [Sei13]. High temperature tests of the battery have been performed. According to the testing results, the battery can support the system operation in detection state (12 µA average current) at 125°C for at least two 6 h cycles without evident capacity loss. No leakage or explosion was observed in any testing cycle. At 150°C, this battery model has enough capacity to support the system operation for two 6 h cycles, though the capacity of the battery is gradually lost.

The IXYS CPC1822 is a monolithic photovoltaic string of solar cells. The nominal output voltage of CPC1822 is 4.2 V at the illuminance of 6000 lux. The nominal short-circuit output current is 50 µA and this value can increase up to 200 µA with higher intensity light. This solar cell has a footprint of 5.8×5 mm^2 [Ixy12]. The charging protection resistor $R_{protect}$ is selected as 10 kΩ to limit the charging current to 100 µA, following guidelines in the battery document [Sei11, Sei12].

A buffer capacitor of 4.7 μF is connected in parallel to the battery to accommodate any transient current need when the system operates in the active mode. This includes brief use of the analog to digital converter (ADC), temperature sensor, high power oscillator for initialization of the MCU, etc.

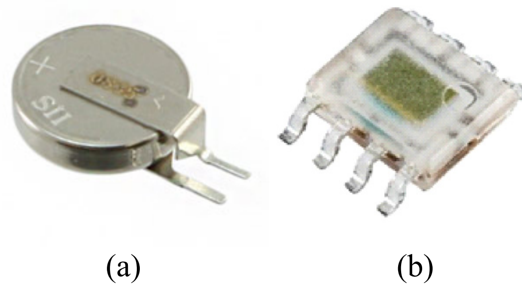

(a) (b)

Figure 2.3: (a) The MS412FE battery from Seiko Instruments [Sei14]. (b) The CPC1822 photodiode from IXYS Integrated Circuit Division [Ixy12].

2.1.3. Schmitt Trigger Block

A special Schmitt trigger block is designed to manage low battery conditions that may be encountered in prolonged deployment periods. As shown in Fig. 2.4, the C8051F990 MCU consumes significantly higher current when its supply voltage drops below the minimum operation voltage (1.8 V) specified in the datasheet. In room temperature operation, the current draw reaches 1.52 mA at a supply voltage of 1.6 V, which is ≈19× the normal current draw in the active mode. This elevated current draw, which would be exacerbated at high temperatures, shortens the deployment lifetime. Additionally, it prevents charging of depleted batteries before or after the deployment period as this current draw significantly exceeds the combined maximum current available from the battery and the solar cell.

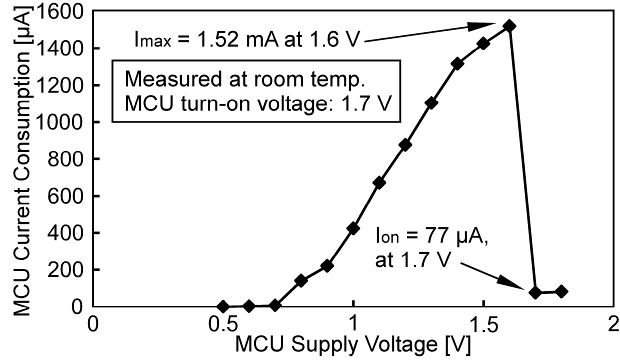

Figure 2.4: Measured current consumption of the MCU at various power supply voltages. The peak current consumption appears at 1.6 V V_{supply}. This current consumption significantly exceeds the maximum allowed continuous discharging current of the lithium battery (100 µA) [Sei14].

To address the problem of excess current draw by the MCU at low supply voltages, the ELM power supply circuit includes a Schmitt trigger along with the battery charging circuit. The charging circuit uses the IXYS solar cell and other components to supply the necessary current for recharging the battery. The Schmitt trigger, implemented by a comparator (TI TLV3012) and three resistors, serves as a power switch with hysteresis to safely shut down the MCU before the supply voltage drops too low during deployment, and to prevent the MCU from turning on at lower battery voltages. As shown in Fig. 2.2, when the battery is being charged and its voltage (V_B) is below the higher hysteresis threshold voltage (V_H) of the Schmitt trigger, the Schmitt trigger is off and its output voltage (V_O), which sets the supply voltage for the MCU, remains at 0. When V_B reaches V_H, the Schmitt trigger is turned on and V_O follows V_B closely; this also turns on the MCU. When the battery is discharging, the Schmitt trigger remains on until V_B goes below the lower hysteresis threshold (V_L), at which point the MCU is safely turned off. The values of V_H and V_L are determined by the three resistors [Smi88]:

$$V_H = \frac{1.2 \times (R_{c1} + R_{c2} \,||\, R_{c3})}{R_{c2} \,||\, R_{c3}} \quad (2.1)$$

$$V_L = \frac{1.2 \times R_{c3}}{R_{c1} \,||\, R_{c2} + R_{c3}} \quad (2.2)$$

For this work, V_H is set to 2.45 V and V_L to 1.95 V, allowing proper operation of the MCU during prolonged deployment periods and effective battery recharging after deployment. The selected resistance values are R_{c1} = 1 MΩ, R_{c2} = 3.9 MΩ and R_{c3} = 1.5 MΩ. The selected resistors are in the MΩ range to minimize the current consumption of the Schmitt trigger circuit.

2.1.4. An Optical Communication Box for ELM

An optical communication box is built as the interface between the client and ELM. The communication box is controlled by Labview^{TM} program installed on a laptop. A data acquisition (DAQ) card is connected between the laptop and the communication box. Inside the communication box, there is a bright LED to generate patterned light pulses for triggering the ELM, a high sensitive photodiode to receive the optical signals from the ELM LEDs, and a 9V battery for power supply. From the Labview^{TM} program on the laptop, clients can trigger the ELM into different operational states and readout the stored environmental data.

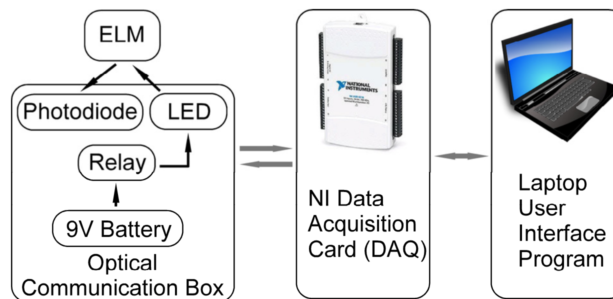

Figure 2.5: The block diagram of the optical communication box. The box contains hardware for optical communication and is controlled by a Labview^{TM} user interface program. A data acquisition card is connected between the box and the PC.

2.2. System Software[1]

The ELM1.0 software is implemented in the MCU to provide functions including system control and power management, temperature measurement, data processing and storage, and bidirectional communication with an exterior control/readout system through the optical link. The goals for the software development include: develop and optimize code for low power consumption and high temperature stability, limit memory usage, and retain straightforward operation flow for ease of use.

The state diagram of the system software is shown in Fig. 2.6. The solar cell in the system generates different voltage pulses according to the received external light pulse patterns. These voltage pulses trigger the MCU into different functional state. There are 7 functional states and one error state in the state diagram. State 1 is the MCU off state when $V_{dd} < V_{th}$. State 2 is MCU initialization state, in which MCU is turned on and all dynamic memory is refreshed. State 3 is deep sleep state; this is the state when the MCU core is turned off and only the low frequency clock (real-time clock described later) is on, and system consumes minimal power. The two key functions of the system, temperature data collection and reporting, are implemented in the detection (State 4) and readout (State 5) states, respectively. In State 4, the system wakes up from deep sleep, turn on the temperature sensor and Analog-to-Digital Converter (ADC), performs temperature measurement every 2 min, and store the data in the flash memory. In State 5, the system reports data to an exterior receiver unit by flashing the LEDs. Each temperature data point is coded in a two-byte form and all bytes of data are sent consequently. CRC is performed on all bytes of data set. State 6 is erase state, in which the temperature measurement data stored in the

[1] Portions of the software were developed by Mr. Ryan Meredith.

flash memory is erased to open up storage space for new measurement. State 7 is reset state, in which the system is manually reset and all registers in the program are refreshed.

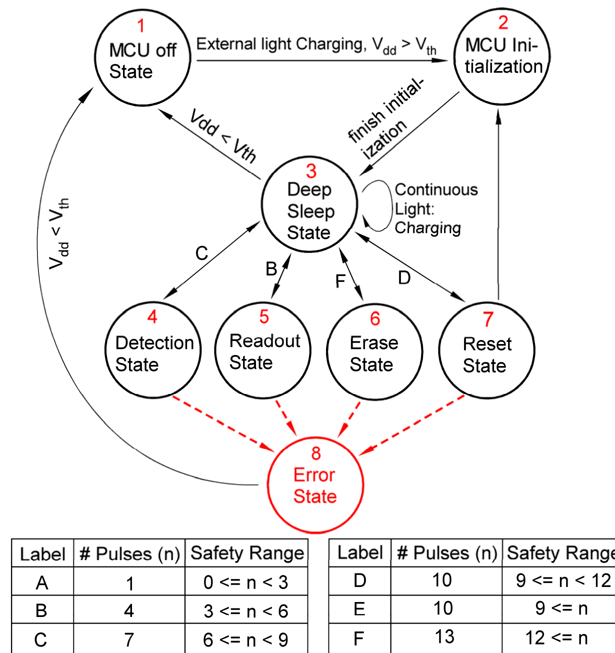

Label	# Pulses (n)	Safety Range
A	1	0 <= n < 3
B	4	3 <= n < 6
C	7	6 <= n < 9

Label	# Pulses (n)	Safety Range
D	10	9 <= n < 12
E	10	9 <= n
F	13	12 <= n

Figure 2.6: Overall system software state diagram. The system consists of 7 regular operation states. The transition between states is triggered by light patterns specified in the table.

The detection state performs the temperature measurement with a predefined schedule and the sub-states diagram is shown in Fig. 2.7. When the system enters this state, the red LED flashes 3 times. The system then enters the sleep mode to conserve power until a measurement is to be taken. The first temperature measurement is made 5 minutes after entering the state to allow the user time to load the system into the target environment. Then the system wakes up every 2 min for the following measurements. Between measurements, the MCU may also wake up by optical triggering (for testing or exception reasons). This can trigger the system to exit the detection state, to reset the MCU and immediately re-enter the detection state with the same sequence number of temperature measurement, or to check whether the system is in the detection state by LED flashing. If the time when the system is woken up by triggering (i.e. in State 4c) overlaps with the time that

a measurement should be taken, the measurement will be taken immediately after State 4c finishes. In this state, the comparator of the MCU is disabled when the system detects a temperature >60°C. This is to avoid unexpected system wake up by interference signals on the comparator input at higher temperatures. The comparator is re-enabled when a temperature below 60°C is detected. The comparator is also re-enabled when the system finishes all measurements and goes to the sleep mode (State 3).

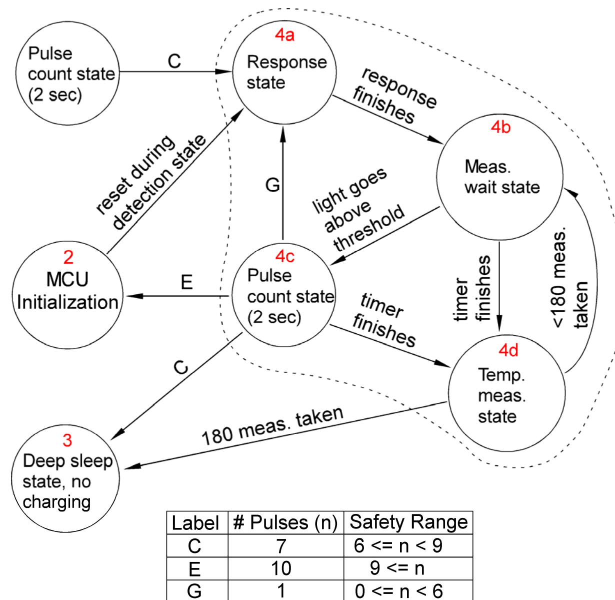

Label	# Pulses (n)	Safety Range
C	7	6 <= n < 9
E	10	9 <= n
G	1	0 <= n < 6

Figure 2.7: The diagram of sub-states for State 4, the detection state.

The readout state reports data to an exterior receiver unit by flashing the LEDs to represent measured temperature data, and the sub-states diagram is shown in Fig. 2.8. When the system enters this state, it flashes the red LED 9 times. During data readout, the '1's are represented by the on state of the LED, and the '0's are represented by the off state. All data are transmitted at a rate of 16 bits/sec. For each data set to be sent, the MCU first sends one byte of data to communicate to the exterior receiver the size of the data set (number of bytes). A '1' is appended to the front of this byte of data, signifying the start of transmission. A delay of 2 sec is inserted

from the time that this appended '1' is sent before the first bit of the actual data is sent. Each temperature data point is coded into two bytes, and all bytes of a data set will be sent consecutively. A '1' is again appended to the front of the first byte of the data set to indicate the start of transmission. A built-in MCU resource is used to perform CRC on all bytes of each data set, and the two-byte CRC result is sent at the end of the data set transmission. The system then waits 2 sec for a response from the exterior receiver. According to the response received, it would resend the same data set, send the next data set, or exit the readout state. This state also ends if no response is received from the exterior receiver during the 2 sec delay, or if all data have been sent properly.

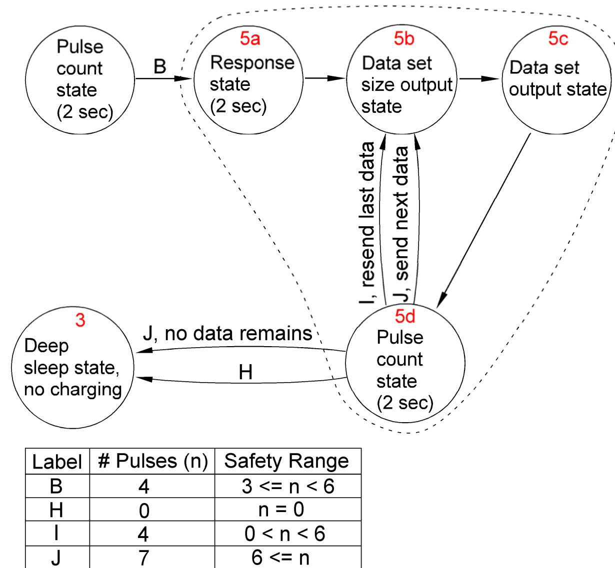

Label	# Pulses (n)	Safety Range
B	4	3 <= n < 6
H	0	n = 0
I	4	0 < n < 6
J	7	6 <= n

Figure 2.8: The diagram of sub-states for State 5, the readout state.

The typical software operation flow of a field test for temperature logging with the ELM1.0 is provided in Fig. 2.9. After assembly and packaging of the system with a fresh battery, the MCU is initialized (State 2) and then put to the deep sleep mode for storage (State 3). The system is expected to typically remain in State 3 until prepared for deployment. However, if the system is stored for too long (>1 weeks), the system battery may be drained below V_L and the MCU will be

turned off (State 1). In any case, the battery must be recharged to a certain voltage above V_H to allow the MCU to be re-initialized and to go back to deep sleep state (State 3). When the system is ready to be deployed, the detection state (State 4) is triggered by the corresponding light pattern. Then the system performs the temperature measurement activity following a predefined schedule. When all measurements are done, the system is triggered back to the deep sleep state (State 3). After the system is unloaded from testing and cleaned up, the client triggers the system into the readout state (State 5) and retrieves all measurement data in the system flash memory. This concludes the typical operation flow for oil well temperature logging.

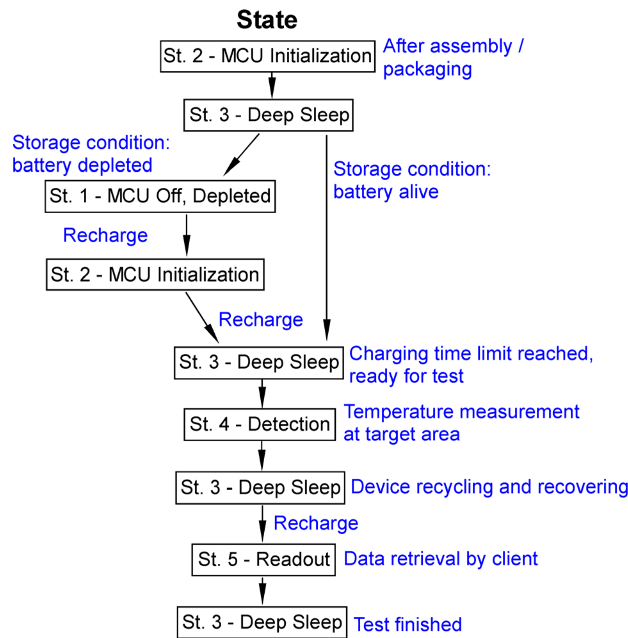

Figure 2.9: Typical operation flow chart of the ELM1.0. After assembly and packaging, the system is put into deep sleep state for storage. Recharge is required before the deployment of the system. During deployment, the system will go through detection state, deep sleep state, readout state, and back to deep sleep state.

The software is optimized for minimal system power consumption while maintaining the functionality. This is achieved by designing the software so that the MCU is in the sleep mode as much as possible. For example, the MCU is put in deep sleep mode during the waiting between

measurements in the detection state. As another example, when the MCU must perform a task that takes a specific amount of time (e.g. when flashing the LEDs at a certain rate in the Readout state), the MCU is placed in the idle mode to further conserve power. The clock selection is also critical to maintain low power consumption. There are three oscillators integrated with the MCU: two that operate at high frequencies (>20 MHz) for fast operation but require large currents (>0.2 mA), and one that operates at 32 kHz and consumes much less current (<1 μA). The 32 kHz low frequency oscillator, known as the real-time clock (RTC) oscillator, is therefore selected for the system operation. This frequency is adequate for temperature logging in the target application. However, the RTC must be calibrated for operation at high temperature for clock accuracy. The frequency of the RTC oscillator is fairly sensitive to temperature, increasing linearly with rising temperature but with inconsistent "jumps" in frequency depending upon the supply voltage of the MCU. The internal high precision oscillator, on the other hand, has a frequency nearly independent of temperature, although it uses much more power and is not suitable for the general clock. Therefore, the RTC oscillator is calibrated each time the MCU wakes up from the sleep mode by quickly comparing its frequency against the high precision internal oscillator to ensure the correct timing for next wake up.

The comparator of the MCU is disabled at high temperature to avoid accidental wake up. At high temperatures during the detection state, the solar cell output voltage that is connected to the MCU comparator for optical triggering can have large variations that may inadvertently wake up the system from the sleep mode or even reset the system. The reason for this large signal variation is unclear; possible sources were found to be the solar cell or the TI nanowatt comparator used for the Schmitt trigger. Since charging or triggering is not needed at high temperature, the

comparator is simply disabled when the temperature goes above 60°C and is re-enabled after the temperature drops below it.

2.3. System Fabrication and Packaging

The system components are assembled on a flexible polyimide PCB and then folded into a stack for encapsulation into a stainless steel package. The folded structure reduces the system footprint by a proportion of 3, the total layer number. The flexible polyimide PCB is fabricated and assembled by All Flex Inc., a commercial PCB service provider. The PCB includes a top and a bottom metal layers. The polyimide used for the PCB is DuPont® Pyralux AP, which has a maximum elongation of >50% after curing. This elongation is enough for the board to fold 180°C without damaging the material and metal traces. All the electronic components except the battery are assembled on the top layer of the PCB using commercial assembly service from All Flex. Figure 2.10 shows the configuration of the folded system stack. The stack has three layers: the solar cell and LEDs on the top layer, the battery sandwiched in the middle layer, and the MCU and other components on the bottom layer. The thickness of the polyimide PCB is 300 µm in the component area and 200 µm in the fold. An extra 127 µm FR-4 rigid stiffener is added to the component area to further stabilize the components and prevent the soldered pins from breaking during the folding process. The overall stack size is 6.5×6.3×4.5 mm^3 (L×W×H).

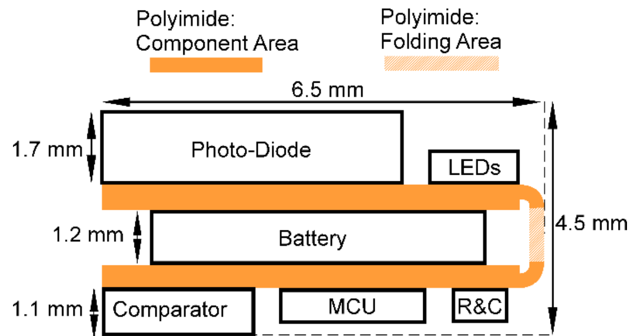

Figure 2.10: Configuration of the folded system stack. Top layer: solar cell and LEDs. Middle layer: battery. Bottom layer: Electronics. Flexible polyimide PCB is used for electrical interconnect between layers.

The system is manually assembled with the battery and then folded into the stack. During the assembly, the two tabs of the MS412FE is removed in the first step. The sidewall of the battery is protected by a thin film of cured enamel paint. In the next step, the polyimide PCB is folded along the folding line, and the top (positive electrode) and bottom (negative electrode) surface of the battery is bonded to the two power pads of polyimide PCB by conductive Duralco 120 silver epoxy (Cotronics Corp). After the silver epoxy is fully cured, the enamel painting is applied on the bottom surface of the stack for insulate protection of the surface mounted electronics. Figure 2.11(a) is the photo of the polyimide PCB and Fig. 2.11(b) is the photo of the folded stack.

The assembled stack is then placed into the 8.9×8.9×6.85 mm^3stainless steel package[1]. A 1 mm thick sapphire lid is assembled to the bonding ring of the package for encapsulation. The epoxy for assembly is baked for 7 hours at 90°C and 15 minutes at 125°C. A parylene layer of 3 µm is coated on the outer surface of the package for anti-corrosive protection. This concludes the integration process of the ELM1.0 system. Figure 2.11(c) is the photo of the folded stack in the package in an angled view.

[1] Folded systems were packaged by Dr. Yushu Ma.

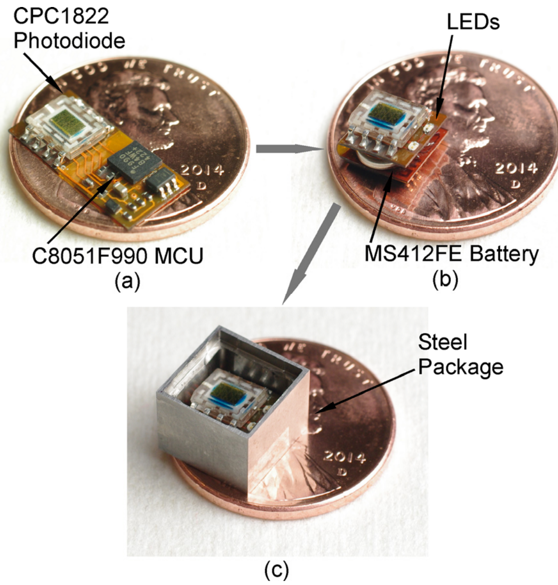

Figure 2.11: Photos of the ELM1.0. (a) Photo of ELM1.0 flexible polyimide PCB before assembly. (b) Photo of the folded ELM1.0 stack. (c) Photo of the ELM1.0 in the package.

Table 2.3 summarizes the overall design parameters of the ELM1.0 system. The physical parameters were measured with caliper. The electrical parameters were measured in the system characterization tests, which are explained in detail in Section 2.4.

Table 2.3: Overall design parameters of the ELM1.0.

Physical Parameters	
Stack size	6.5×6.3×4.5 mm^3
System size with packaging	8.9×8.9×6.85 mm^3
Integration topology	Polyimide flexible PCB
Packaging topology	Stainless steel shell covered by sapphire lid
Electrical Parameters	
Battery nominal voltage	3.0 V
Current (Active, ADC on, RT)	600 μA
Current (Active, ADC off, RT)	84 μA
Current (Active, ADC off, 125°C)	150 μA
Current (Sleep, RT)	5 μA
Current (Sleep, 125°C)	12 μA
Battery capacity & size	1 mA·h Φ4.8 mm x 1.2 mm
Wireless charging time	≈10 h (100 μA, from 2.0 to 3.0 V)
System storage time	≈1 week
Operating frequency	32.768 kHz
Program size	2 KB

2.4. Experimental Methods and Results

Tests of the ELM was carried out in three stages: (a) Characterization of the ELM components and circuits; (b) High temperature tests of the unpackaged ELM systems, with an emulated operational flow; (c) High pressure high temperature (HPHT) tests of the packaged ELM systems at Total (Exploration and Production R&D Division). Test results from (a) and (b) suggest that the system achieved all the intended functionalities for temperature measurement, low power operation, wireless charging and communication. In a high temperature test in Step (b), the unpackaged system operated in detection state at 125°C for 6 hours and recorded all the temperature data. In Step (c), the packaged system survived >1 h in the emulated downhole environment of 125°C, 7200 psi and corrosive solution, and reported the temperature data successfully.

2.4.1. Characterization of ELM1.0 Components and Circuits

Schmitt trigger circuit was tested at room temperature to verify the hysteresis behavior of the circuit and measure the threshold voltages V_H and V_L. In the test, a variable DC power supply provided the supply voltage (V_B) to the Schmitt trigger. The output voltage of the Schmitt trigger (V_O) was monitored by an Agilent multimeter. During the test, V_B was increased slowly from 1.0 V to 3.0 V, and then decreased from 3.0 V to 1.0 V. The value of V_O at each V_B was recorded and is plotted in Fig. 2.12. The measured threshold voltages are V_H = 2.45 V and V_L = 1.95 V, which matches the calculation results (V_H = 2.4 V and V_L = 1.9 V) from equation (2.1) (2.2).

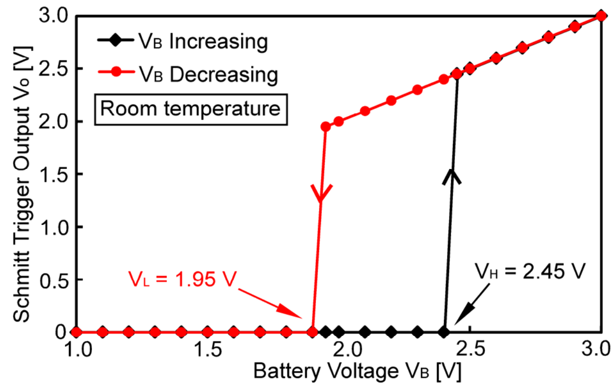

Figure 2.12: Results of the Schmitt trigger circuit test. The measured threshold voltages were V_H = 2.45 V and V_L = 1.95 V. These voltages matches the calculated threshold values.

The power consumption of the ELM electronics was characterized at various temperatures, in both active and sleep modes. The unpackaged system was buried in sand for uniform heating. A 2.4 V supply voltage was provided to the system (positive and negative pins) by a variable DC power supply. This voltage is the average of the range of the battery voltage that is necessary for system operation (1.8-3.0 V). The current consumption of the system at different temperatures was recorded by an Agilent multimeter. In the sleep mode, the only modules that were on in the MCU were the power management unit and the 32 kHz low frequency oscillator. The

corresponding current consumption was 5 μA at 25°C, 7 μA at 80°C, 12 μA at 125°C and 30 μA at 150°C. When the system was in the active mode, with the MCU processor turned on and the temperature sensor and ADC turned off, the current consumption went from 84 μA at 25°C to 325 μA at 150°C (Fig. 2.13). The components that were turned off for this characterization are not expected to significantly affect the measurement results because the time when these components are active is less than 1% of the total system active time. According to the measurement results, the system is not well suited for operation at temperatures exceeding 150°C. At this temperature, the high sleep mode current consumption can quickly deplete the battery. At a temperature of 125°C or lower, the power consumption of the system remains relatively low, allowing the system to operate with the selected battery for an extended period of time.

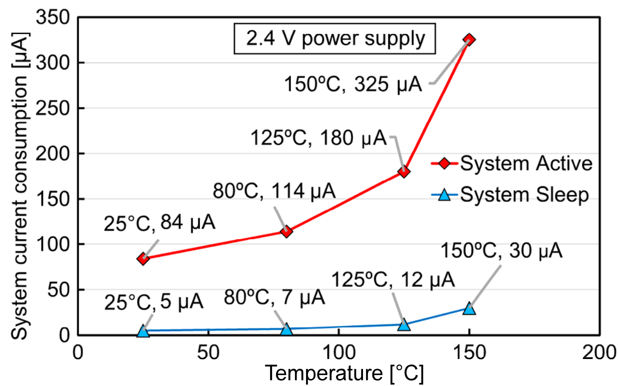

Figure 2.13: The static current consumption of the system in active / sleep mode at various temperatures. Power supply V_B = 2.4 V is selected for representing the average voltage in the system operation cycles.

The temperature calibration test was performed on the ELM1.0 to verify the accuracy of temperature measurement. The ELM1.0 was buried in a glass container filled with sand for uniform heating and the environment temperature was monitored by a thermocouple during the test. In this test, the environment temperature increased from 22°C to 125°C with a ramp-up time of 30 min and a hold time of 5 min. The temperature data from the thermocouple was recorded at

the same time when the MCU took temperature measurement. From the testing results shown in Fig. 2.14, the temperature readings from the ELM follows the thermocouple reading closely at low temperature (<80°C). At elevated temperature the offset increases and reaches 3.5°C at the environment temperature of 128.9°C.

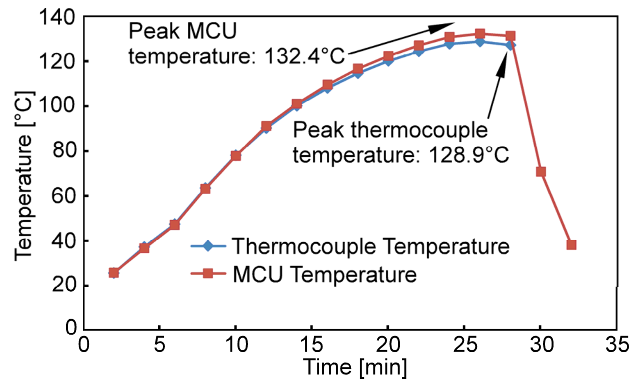

Figure 2.14: The temperature data recorded in the system calibration test. The offset increases with temperature and reaches 3.5°C at the environment temperature of 128.9°C.

2.4.2. High Temperature Tests of Unpackaged ELM

The integrated unpackaged ELM was tested in an emulated operation flow to verify the design validity, system functionality and system lifetime, particularly at the target temperature. To emulate the typical operation flow shown in Fig. 2.7, but on a shorter timeframe, three major steps were carried out in this test. In Step 1, the system was placed in the deep sleep state for 36 hours at 25°C. The decrease of the battery voltage during this period was monitored to estimate the maximum system storage time. In Step 2, the assembled system was recharged until a certain battery voltage was reached (2.8 V in this test). The charging current, charging time and battery voltage were recorded. In Step 3, the recharged system was optically triggered into the detection state and buried in hot sand with the temperature raised up to 125°C. The detection state lasted 6 h in total and the voltage of the battery was recorded during the process. When the detection period

is reached, the system was cooled down, triggered into the readout state, and the data were reported to a laptop computer.

In Step 1, the assembled ELM was put in the sleep mode (State 3) and maintained at 25°C. The fresh battery was at 2.64 V, which represents ≈80% of the full capacity [Sei14]. After 36 h, the battery voltage dropped to 2.49 V (Fig. 2.15(a)). As shown by the trend line, this battery is expected to support the system in the sleep mode for more than 180 hours (7.5 days), dropping to a projected value of 2.3 V. The ending voltage 2.3 V is still within the linear discharge region of the battery characteristic, thus a linear trend line is effective. In a separate depletion test, the system entered error state with battery voltage <2.3 V due to an instant current peak generated by a MCU wake up event. This behavior is explained in detail in the discussion section.

The same system after Step 1 was recharged by an external light source at 25°C. After charging for 1 hour, the battery voltage increased from 2.55 V to 2.8 V, and charging current dropped from 100 μA to 80 μA (Fig. 2.15(b)). The battery voltage recovered slightly from 2.49 V to 2.55 V before recharging. The 2.8 V battery voltage represents over 90% capacity of the battery [Sei14].

Next, this recharged ELM was triggered into detection state (State 4) and then buried in hot sand for a high temperature test. A thermocouple was buried within 1 mm of the system to record the environment temperature as a reference. During the test, the temperature of the sand was ramped up for 0.5 hour to 125°C, and then stabilized at 125°C for 5 hours. Cool-down was then initiated. At the end of the 6 h test, the system temperature dropped to 71.2°C as measured by the thermocouple. The temperature was measured by the system every 2 minutes and the data were stored in the flash memory of the MCU. As shown in Fig. 2.15(c), the battery voltage

dropped from 2.71 V to 2.48 V during the 6 h test. After the test, the system was triggered into the readout state (State 5) to verify the wireless data reporting capability. The LED indicators flashed as expected, indicating that the temperature data was successfully stored in the flash memory and could be transmitted through the optical link. The temperature data stored in the flash memory of the MCU was then reported to a laptop computer. Figure 2.15(d) shows the measured temperature data, compared to the values obtained by the thermocouple. The two sets of data match very well, with a small discrepancy <5°C.

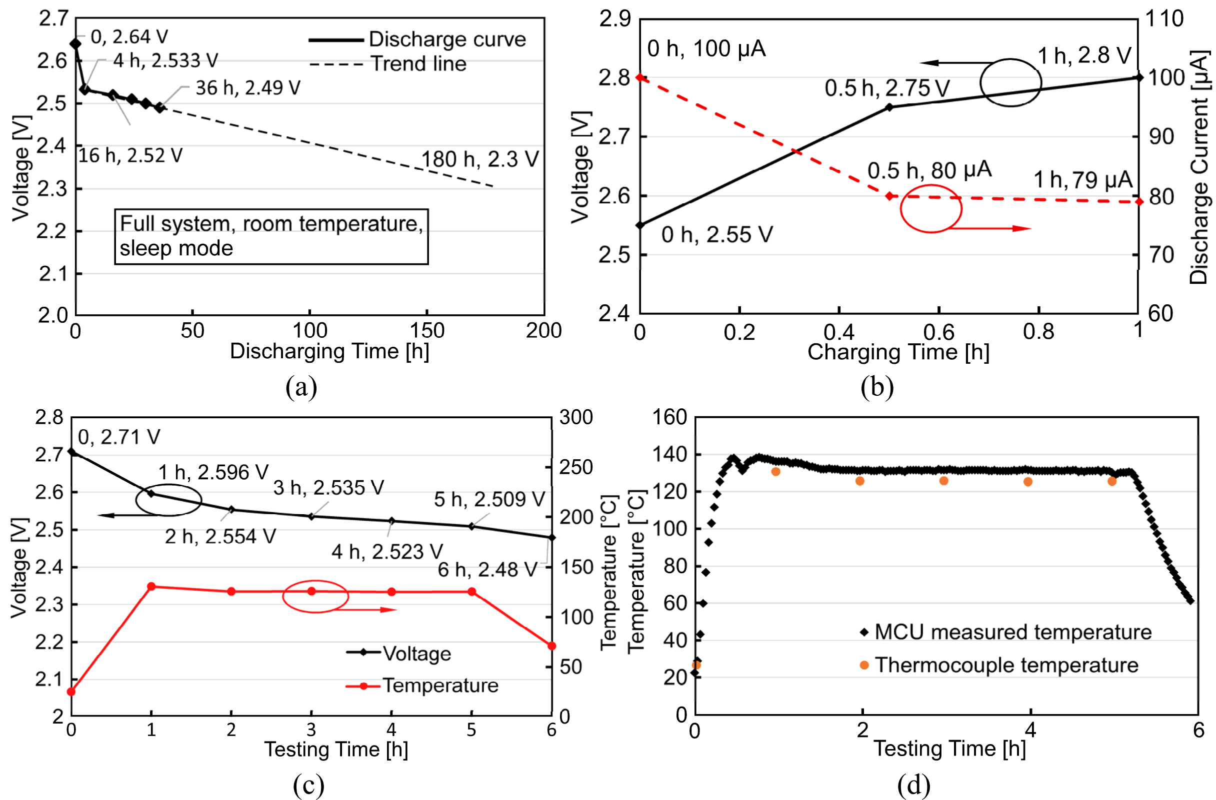

Figure 2.15: The results of the high temperature system test in an emulated operational flow. (a) Step 1, the discharge curve of the system battery in storage. (b) Step 2, the charging curve of the system battery. (c) Step 3, the discharge curve of the system battery in the high temperature test. (d) Step 3, the temperature data stored in the MCU flash memory during the high temperature test.

Tests were also performed on the ELM1.0 system at temperatures higher than 125°C. During these tests, the systems under test were heated in sand, and were held at target temperatures

for 5 minutes. The systems were then retrieved from the hot sand; the tests were stopped after the systems cooled down. Figure 2.16 shows the temperature data recorded in one of the tests at 150°C. The ELM1.0 system was able to successfully measure and store temperature data at 150°C, and later correctly reported the stored data. The ELM1.0 system electronics without an integrated battery was also separately tested at 160°C when connected to an external DC power supply. The system electronics survived this higher temperature, and correctly recorded and stored the temperature data. The battery was not used in this test in order to allow the independent assessment of the electronics.

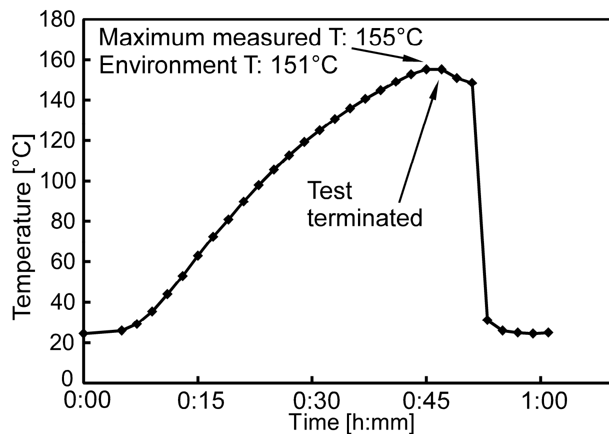

Figure 2.16: The reported temperature curve during the stressed high temperature test. The system is able to measure temperature up to 150°C.

2.4.3. HPHT Tests of the ELMs at Pau, France

The packaged ELMs were subjected to a series of HPHT tests at Total (Exploration and Production R&D Division in Pau, France). There were three major steps in the HPHT tests (Fig. 2.17). In Step 1, the ELM systems were fully recharged using a light source and triggered into the detection state. The systems were then sealed into plastic bags, each of which was filled with one of the three selected test solutions: API standard brine, Isopar^{TM}-L and uncured cement slurry (Table 2.4). In Step 2, the plastic bags, with the systems and test solution inside, were inserted

into an HPHT instrument for tests. This instrument was custom-built by Total and had three separate testing cells, each of which was filled with mineral oil and could generate HPHT conditions according to settings programmed in the instrument. For each cell, the maximum temperature allowed was 180°C and the maximum pressure allowed was ≈10,000 psi. In each test, the temperature was ramped to the target value in ≈30 min., and the target pressure was then switched on. The target pressure and temperature were held stable for a specified period of time. Afterwards, the pressure was switched off, and the temperature was ramped down for ≈30 min. In Step 3, the systems were retrieved from the testing cells and cleaned up. The systems reported recorded temperature data wirelessly to a laptop.

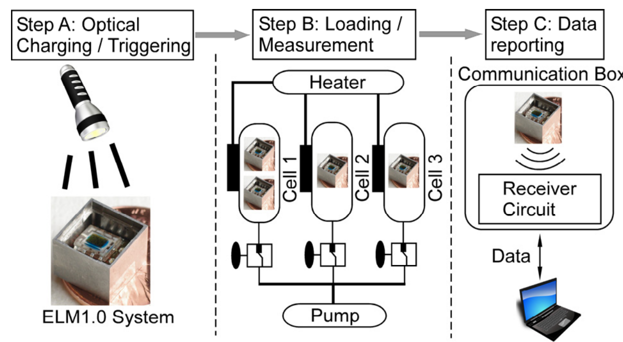

Figure 2.17: The HPHT testing procedure for ELM1.0 system at Pau, France.

Figure 2.18 summarizes the HPHT test results. The ELM successfully passed the tests and survived the conditions identified in the figure. Measured temperature data were successfully reported wirelessly in each test. The ELM systems survived the HPHT conditions at up to 125°C and up to 10,000 psi. The ELM survived all three test solutions: API brine, Isopar^{TM}-L, and cement slurry, at separate temperature and pressure condition. The ELM systems also survived longer test hold time at the a slightly reduced temperature, including 3 hours at 100°C and 7200 psi. Figure 2.19(a) shows the temperature and pressure data reported by HPHT equipment during a typical

test with HPHT condition of 125°C, 7200 psi, 1 hour hold time in API brine. The temperature data reported by ELM in this test is shown in Fig. 2.19(b), which matches the temperature data from the equipment.

Table 2.4: Testing solutions used in the HPHT tests in Total, France.

Testing Solutions	Description
API Brine	$CaCl_2$ 2 wt% + NaCl 8 wt%
Isopar^{TM}-L	Synthetic isoparaffinic hydrocarbon solvent from Exxon Mobil
Cement	Uncured cement slurry

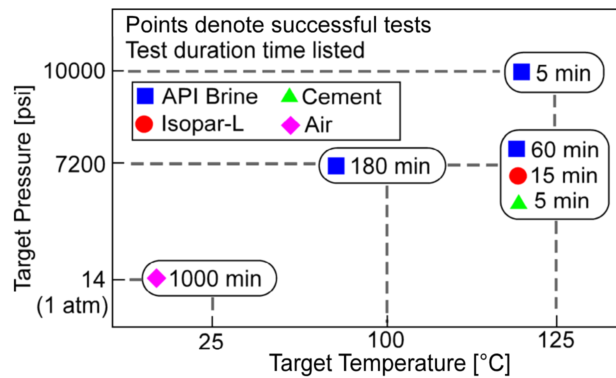

Figure 2.18: The summary of the testing results at Total Research Center, Pau, France. The ELM1.0 survived 125°C and 7200 psi in API brine. It also survived 10000 psi and cement slurry solution.

Additional tests were performed, including a hermeticity test with Isopar^{TM}-L or cement at 125°C and 7200 psi, a high pressure test at 10000 psi, and an extended duration test at 103°C with longer hold time (3 hr.). The ELMs successfully passed these tests with no evident package deformation or leakage, and the temperature data were successfully reported to client. The temperature and pressure data reported by the HPHT equipment are plotted in Fig. 2.19(c) and the temperature data reported by ELM1.0 is plotted in Fig. 2.19(d).

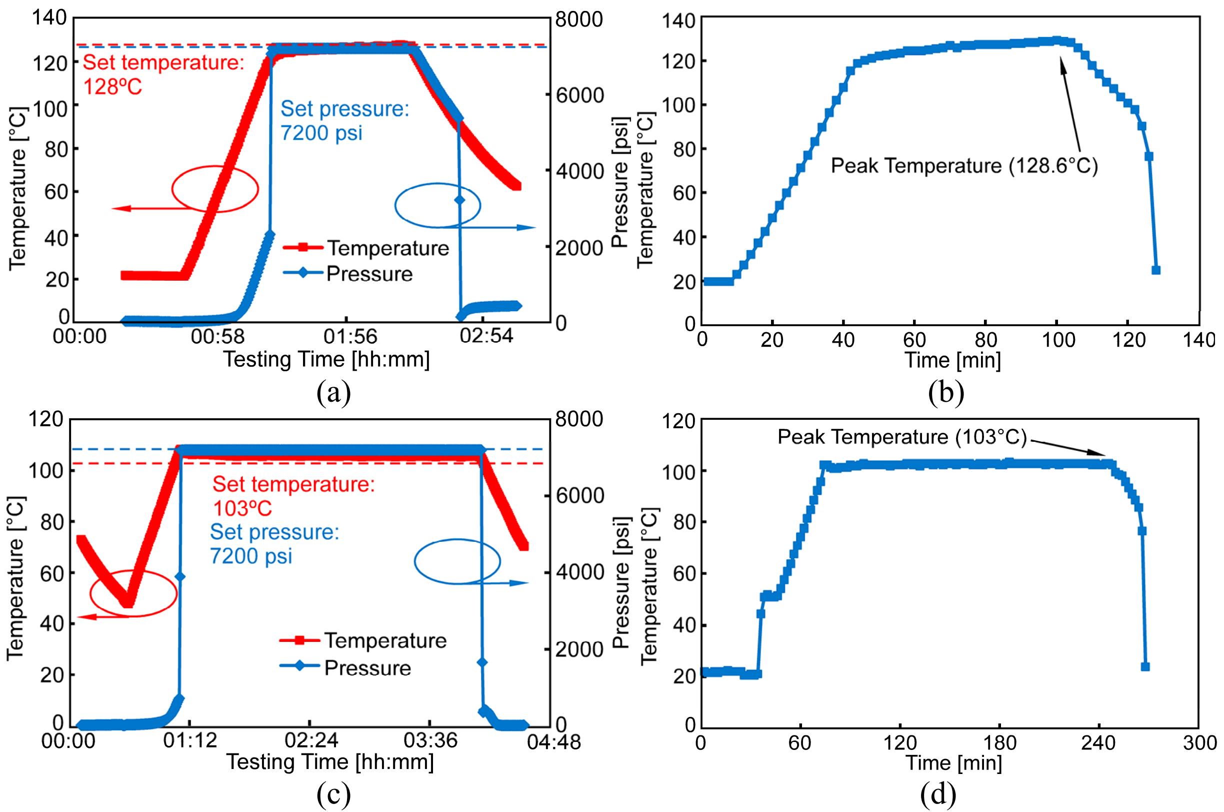

Figure 2.19: (a) Temperature and pressure in the testing cell reported by the HPHT instrument from the standard HPHT test. (b) Temperature data reported by the system during the standard HPHT test. (c) Temperature and pressure reported by the HPHT instrument from the extended duration test. (d) Temperature data reported by the system during the extended duration test.

A trans-Atlantic flight test was performed by keeping one of the ELM systems running in checked luggage during the return flights from Pau, France to Detroit, USA, with a connection in Paris, France. The microsystem was recharged overnight before departure in order to maximize the battery charge. The system was triggered into the detection state just before departure from Pau. The checked luggage with the system went through the regular airport examination procedures. The system was retrieved and triggered out of the detection mode after arriving in the laboratory at the University of Michigan. The overall transit time was over 20 hours. The system was recharged and >16 hours of effective temperature data was successfully transmitted to a laptop computer (Fig. 2.20).

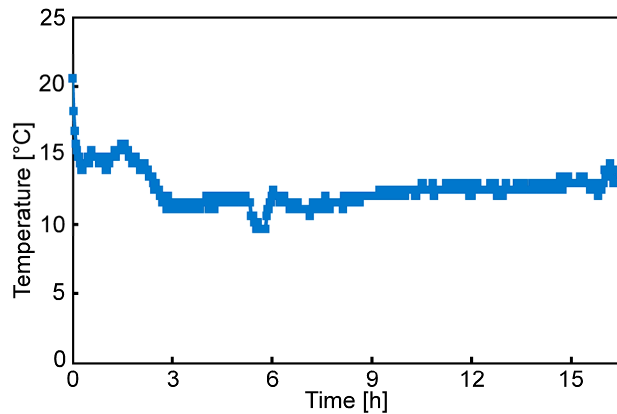

Figure 2.20: The measured temperature during the flight test from Pau, France to Detroit, USA. A total amount of 16 hours data were collected.

2.5. Discussion and Summary

The encapsulated ELM1.0 systems were successfully tested in HPHT conditions in corrosive ambient environments. This suggests that both systems can potentially survive certain downhole environment with similarly harsh conditions. The electronic and software configurations used in the ELM allowed operation at temperatures reaching 150°C despite the use of standard commercial components that are rated only to 85°C. The selected batteries for both systems could support system operation at these high temperatures. The system packages were shown to provide adequate protection from the high pressure and corrosive conditions for at least three hours.

The electronic chips for both systems were fabricated using standard CMOS technology that is not optimized for high temperature operation. Specialized electronics for temperatures well above 200°C use technologies such as trench isolation, silicon-on-insulator (SOI) substrates, and other variations of the standard CMOS process [Wat12, Web-Har]. Among these, the trench isolation approach uses enhanced isolation between adjacent transistors, whereas the SOI substrate approach uses an insulation oxide layer buried beneath the transistor layer to reduce the leakage

current from the source or drain of the transistor to the substrate. Silicon carbide electronics also have excellent high temperature performance, but will serve as an option only after the scale of integration has been significantly advanced [Yan13].

Rechargeable batteries at the millimeter scale that also provide enduring high temperature operation remain a challenge. The commercially available coin battery used in ELM1.0 uses manganese silicon lithium [Sei14]. It has high energy density, but its miniaturization is limited by its package. It has a rated temperature range up to 60°C, and its performance is degraded significantly at higher temperatures. Batteries based on lithium thionylchloride ($LiSOCl_2$) become appealing for oil field applications due to outstanding performance at high temperature [Hen98]. Non-rechargeable batteries based on this chemistry have been developed by Tadiran Batteries for operation at 150°C. However, the smallest available option has a cylinder shape with a size of Φ24.5 mm×5.8 mm [Tad11]. Even though this chemistry is excellent at high temperature, the inability to recharge is a problem for the intended application. Batteries with smaller form factor have not been made available yet for this chemistry.

A buffer component is needed in parallel with power supply to handle high instantaneous current peaks. The instantaneous current peaks are generated during each wake up event and can reach >1 mA, which exceeds the maximum continuous discharging current of the battery [Sei14]. With this current peak, the battery can drop below the V_L of the Schmitt trigger circuit for a short period, which causes the Schmitt trigger to turn off unexpectedly. As a result, the measured turn-off voltage of the system is 2.3 V instead of the low threshold voltage of the Schmitt trigger V_L (2.0 V). In the current design, a 4.7 μF decoupling capacitor is placed in parallel with the battery to provide the demanded instantaneous current. Integration of larger capacitor will increase the

lifetime by allowing larger instantaneous current peaks and reducing the turn-off voltage of the system.

The system size can be further reduced by removing the packages of the commercial electronic chips. Currently, each individual chip in the system is encapsulated in plastic package with surface mount pads. The bare chip die inside the package has much smaller size. To reduce the system size, bare dies of these components can be acquired and assembled onto the PCB. By estimation, replacing all packaged components with their bare die version would results in at least 20% smaller system size.

In summary, this work has demonstrated that autonomous microsystems can be made for downhole environments for operating temperatures at least as high as 110-150°C using conventional junction-isolated CMOS processes and lithium-based batteries. Microsystems that use commercial off-the-shelf electronics, coin cell batteries, and flexible PCB substrates, can be designed to mitigate certain temperature effects; these microsystems can be implemented in a volume of $6.5\times6.3\times4.5$ mm^3. The larger volume of such systems is consumed by larger batteries that are necessary to accommodate the higher current draw and the surface mount chip packages that are necessary to facilitate the commercial PCB assembly. As shown, the microsystem can be hermetically encapsulated to tolerate corrosive and high pressure environments.

Additional sensing modalities are of high interest for integration into the ELM1.0 system, including pressure, acoustic, inertial, and chemical sensors. In this work, the integration with pressure and inertial sensors is described in Chapter 3.

CHAPTER 3:

AUTONOMOUS MICROSYSTEM FOR DOWNHOLE TEMPERAUTRE AND PRESSURE LOGGING

This chapter first describes the second generation of ELM (ELM2.0) which provides functions of recording both the downhole temperature and pressure. As described before, the downhole pressure is a critical environmental parameter in oil well logging; however, ELM1.0 system does not provide the function to record it. To achieve the pressure sensing functionality and maintain the existing system size and lifetime, the second generation of ELM system has been developed. ELM2.0 inherits the majority of circuit blocks of ELM1.0, and adds a micromachined pressure sensor. This can be chosen from two pressure sensors which cover different pressure ranges, one at a lower pressure up to 2.5 MPa for demonstration, and the other up to 50 MPa for actual use. The ELM2.0 components are integrated on a flexible circuit board and folded into a stack shape, which has a size of 7.2×6.6×6.5 mm^3. The folded systems are encapsulated in steel packages filled with transparent polymer. The ELM2.0 systems were successfully tested up to 125°C and 7200 psi in API brine for over 3 hours. An alternate version of ELM2.0, ELM2.1, included an inertial measurement unit (IMU) for geolocation tracking and an RFID tag for device identification.

A third generation of the ELM system (ELM3.0) is also described in this chapter. The ELM3.0 system has been upgraded from the ELM2.0 system with several modifications. It has a pre-assembled Seiko battery to reduce the assembly time. A mechanical slide switch is connected

in series with the battery to avoid draining the battery during storage. A trial implementation of a low-cost polyimide pressure sensor (LC sensor) is integrated into the ELM3.0 system for potential application to downhole pressure sensing. This LC sensor is discussed in detail in Chapter 4, and is expected to provide lower resolution and sensitivity than the customized MEMS pressure sensor described in this chapter.

Both the ELM2.0 and ELM3.0 systems were tested in a brine well with a maximum depth of 1235 m, and both systems successfully survived the tests and recorded the temperature and pressure.

A general sensor calibration method was introduced for MEMS pressure sensors with uncalibrated pressure-capacitance relationship. This method was then applied to interpret the ELM capacitance data obtained by the pressure sensors during the brine well tests. The interpreted pressure matched to the pressure obtained by the commercial pressure logging equipment.

The capacitance output from the long duration tests exhibited a drift issue. A principal component analysis method was used as a preliminary attempt to analyze the causes of this capacitance drift and to correct it.

3.1. ELM2.0 & ELM2.1 System Design

The functional block diagrams of the ELM2.0 and ELM2.1 systems are shown in Fig. 3.1. ELM2.0 inherits the existing ELM1.0 components, including a low power MCU with integrated temperature sensor, a solar cell, a charging circuit with Schmitt trigger, two LED indicators, and a 3V miniature rechargeable lithium battery. In ELM2.0, one of two capacitive MEMS pressure sensors with different dynamic ranges is integrated. One of the pressure sensors is a commercial capacitive pressure sensor from the Murata Manufacturing Company for pressure measurement

over 0-2.5 MPa. The operating range of this sensor is significantly below the downhole environment pressure, and this sensor is mainly used for evaluating the system capacitance readout functionality. The other pressure sensor is fabricated at the University of Michigan and is used for downhole pressure measurement over 0-50 MPa. A reference capacitor is included to compensate for the temperature dependency of the MCU capacitance sensing module. In ELM2.1, a 6-axis IMU from STMicroelectronics is integrated for inertial sensing. An RFID tag is also integrated for device identification. Figure 3.2 shows the ELM2.0 and ELM2.1 circuit schematics.

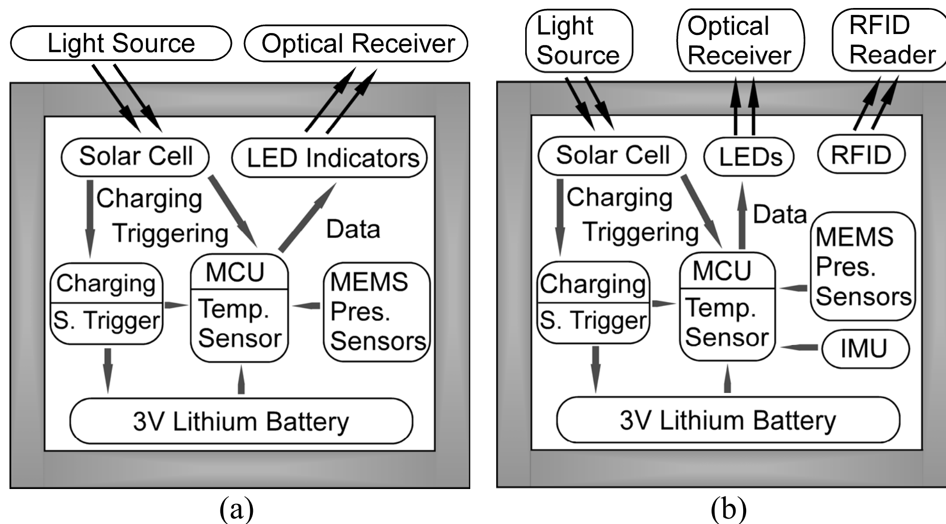

Figure 3.1: (a) The block diagram for ELM2.0. (b) The block diagram for ELM2.1.

Table II summarizes the overall design parameters of the ELM2.0. The size of the ELM2.0 stack is 7.2×6.6×5.5 mm^3 and the size of the encapsulated system with the steel/silicone package is 9.5×9.5×6.5 mm^3. The ELM has a temperature measurement range of 25-125°C with a resolution of 0.5°C, and a pressure measurement range of 0-50 MPa with a resolution of 0.025 MPa. The system has a sleep mode current consumption of 5 µA at 25°C, and 12 µA at 125°C. The average active current during the detection state is 150 µA at 125°C, similar to ELM1.0. The shelf life of the system at room temperature before battery depletion is ≈2 weeks.

Table 3.1: Overall design parameters of the ELM2.0 system.

Physical Parameters	
Stack size	7.2×6.6×5.5 mm^3
System size with packaging	9.5×9.5×6.5 mm^3
Integration topology	Polyimide flexible PCB
Packaging topology	Stainless steel shell with silicone filling
Electrical Parameters	
Temperature range	25-125°C
Temperature resolution	0.5°C
Pressure range	0-50 MPa
Pressure resolution	0.025 MPa
Battery nominal voltage	3.0 V
Current (Sleep, RT)	5 μA
Current (Sleep, 125°C)	12 μA
Current (Active, 125°C)	150 μA
Wireless charging time	≈10 h
System shelf life	≈2 week
System operating frequency	32.768 kHz
System memory size	4 KB

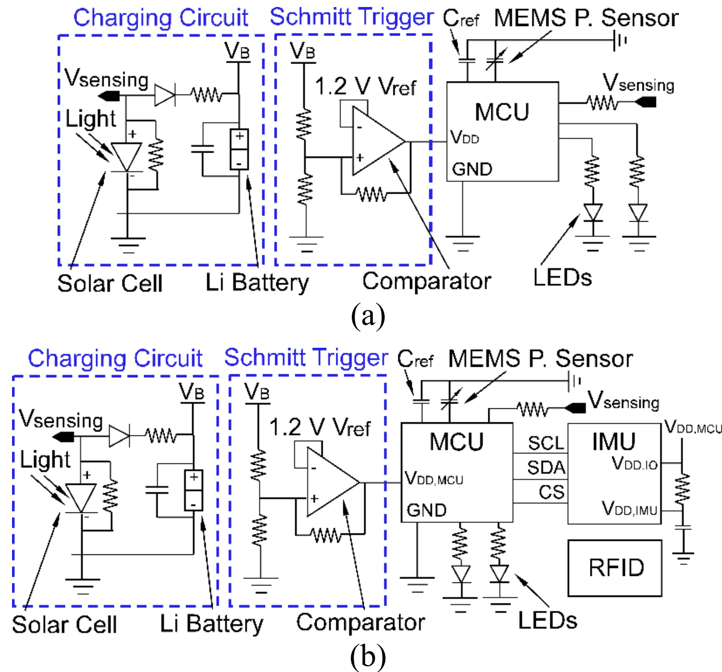

Figure 3.2: (a) The circuit schematic of ELM2.0. The ELM2.0 includes one Murata pressure sensor and one custom pressure sensor. (b) The circuit schematic of ELM2.1. The ELM2.1 has all the components of ELM2.0, and incorporates one STM inertial sensor and one Murata RFID tag.

A new battery MS518FE from Seiko Instruments is used to replace the original battery MS412FE [Sei14]. The new battery is from the same product family. It has a slightly larger size (5.8 mm diameter and 1.8 mm height, compared to 4.8 mm diameter and 1.2 mm height) and >3x capacity (3.4 mAh compared to 1 mAh). This new battery only will increase the system height by 0.6 mm without affecting the footprint. With its larger capacity, the lifetime of ELM2.0 & ELM2.1 is expected to be increased by three times at room temperature. The high temperature performance of this battery model is expected to be similar to that of the old model.

The Murata pressure sensor is a commercial product for pressure measurement up to 2.5 MPa (362 psi), with a footprint of 1.4×1.4×1.0 mm^3 (Fig. 3.3). It has a dynamic range of 0-2.5 MPa, and sensitivity of 1.3 fF/kPa at 100 kPa (14.5 psi) and 6.5 fF/kPa at 2.5 MPa (362.6 psi) [Mur15]. The expected capacitance change over the dynamic range is 7.3-13.9 pF, which can be

easily picked up by the C8051F990 MCU [Mur15]. Although the dynamic range of this sensor is significantly below the downhole environment pressure, the use of this sensor allows early testing and evaluation of corresponding system functions while the sapphire substrate sensors are in fabrication. It also demonstrates system compatibility with other commercial products.

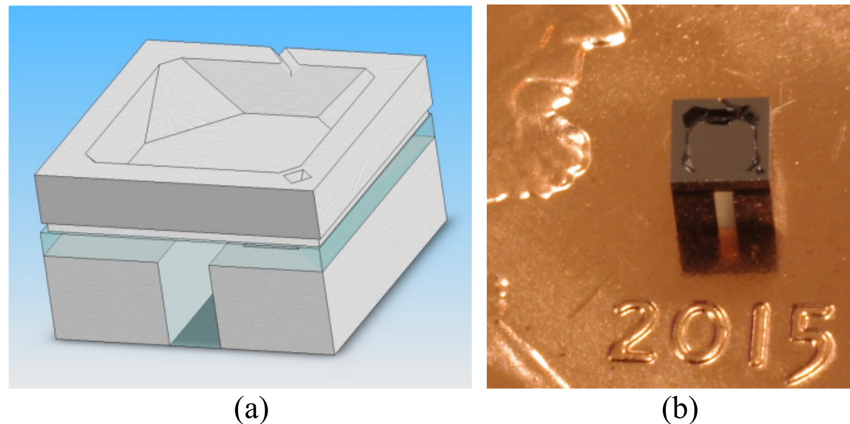

(a) (b)

Figure 3.3: (a) Schematic diagram and (b) photo of the Murata capacitive pressure sensor.

The second capacitive MEMS pressure sensor has been developed at the University of Michigan for downhole pressure sensing (denoted as "AEC pressure sensor" in later sections)[1]. The sensing diaphragm is formed by a SiO_2-Si_3N_4-SiO_2 (ONO, 0.15/1.4/0.15 μm) sandwiched film. The sensing diaphragm has a rounded shape with 100 μm diameter (denoted as C100 pressure sensor, indicating one diaphragm per sensor). The sensing gap is 1 μm. The material of the sensing electrodes is aluminum. A thin film ALD Al_2O_3 with a thickness of 20 nm is used as the dielectric contact material. Sapphire has been selected as the substrate material due to its good thermal mismatch coefficient with the ONO film. The sensor is encapsulated under vacuum with 3.9 μm Si_3N_4 followed by 100 nm ALD Al_2O_3. To enhance the capacitance change, a sensor with 4 diaphragms in an array has been designed for the ELM platform (denoted as 4C100 pressure sensor,

[1] Pressure sensor was designed, fabricated and tested by Mr. Alexander Benken.

indicating four diaphragms per sensor). With an input pressure range of 0-50 MPa (0-7200 psi), the output capacitance change of the sensor is >2 pF with relatively good linearity. This capacitance change can be easily picked up by the C8051F990 capacitive sensing module and a pressure resolution of 0.025 MPa (1 fF capacitance resolution of the CS module) is achieved with noise ignored. Fig. 3.4 shows the SEM photo of the 4C100 pressure sensor.

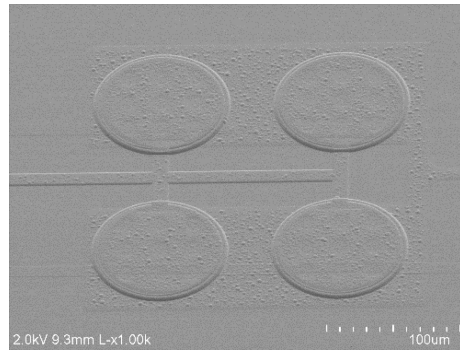

Figure 3.4: The photo of the micromachined pressure sensor developed at the University of Michigan, denoted as “U. Michigan pressure sensor”.

A Murata RFID tag is integrated with the ELM 2.1 system for wireless identification [Mur14]. The device identification code can be stored in the RFID tag. This data can later be wirelessly read by an RFID reader, thus allowing identification of the corresponding system unit. The selected RFID tag has a miniaturized footprint of 2×1.2 mm^2 to fit the system size. This tag uses the EPC^{TM} Class 1 Gen. 2 UHF RFID protocol. It has a communication frequency of 860-960 MHz and a maximum communication distance of $\approx$1 cm. The RFID tag has been tested on ELM2.1 system and the functionality is verified.

The software of ELM2.0 has been upgraded from the software embedded in ELM1.0 and Fig. 3.5 shows the new system state diagram[1]. In the detection state, the system will turn on the

[1] Portions of the software were developed by Mr. Ryan Meredith and Ms. Wenching Tsai.

capacitive sensing module in addition to the temperature sensor and ADC, measure temperature and pressure, and then go back to sleep. Two new states are implemented: State 6 is a battery check state in which the MCU measures the battery voltage and reports back via the LEDs; State 7 is a parameter change state in which the user sets the measurement interval and pressure sensors to be used. A new data storage scheme is used to properly store the pressure and temperature data in the flash memory to improve the data storage efficiency. With the new data storage scheme, about 40 hours of temperature and pressure data can be stored. The software for ELM2.1 is still under development. The inertial sensing state will be implemented to control and read out the motional data from the IMU.

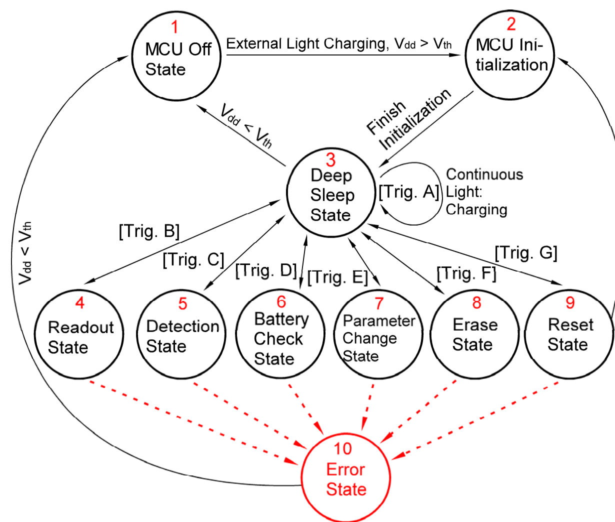

Figure 3.5: The software state diagram for the ELM2.0 system. The detection state has been upgraded and two new states – the battery check state and the parameter change state – have been implemented.

3.2. ELM2.0 and ELM2.1 System Fabrication and Packaging

The electronic components of ELM2.0 are integrated on a flexible polyimide PCB, folded in accordion fashion into three-fold stacks, and then encapsulated in a stainless steel tube filled with soft polymer (Fig. 3.6). The flexible PCBs are fabricated and assembled by All Flex, as with

ELM1.0. The flexible PCB has two metal layers for interconnection of components. The two MEMS pressure sensors (Murata and AEC pressure sensor) are manually assembled onto the fabricated PCBs with conductive epoxy.

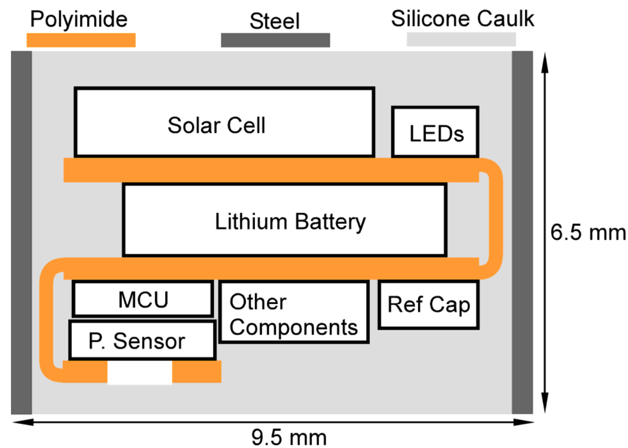

Figure 3.6: Configuration of the folded ELM2.0 PCB in steel package. Top layer: solar cell and LEDs. Middle layer: lithium battery. Bottom layer: MCU, pressure sensors and other electronics. The stack is packaged in the stainless steel tube filled with transparent silicone. The overall encapsulated stack is 9.5×9.5×6.5 mm^3 (L×W×H) in size.

The folded PCB stack has three separate layers: the solar cell and LEDs are in the top layer, the battery is sandwiched in the middle fold, and the MCU, pressure sensors and other components are in the bottom layer. Figure 3.7(a) shows a photo of the ELM2.0 polyimide PCB before folding and Fig. 3.7(b) shows a photo of ELM2.0 after one fold. The overall integrated stack after two folds has a size of 7.2×6.6×6.5 mm^3 (L×W×H) with a volume of 308.9 mm^3. Approximately 50% of this volume is occupied by the surface mount packages of the electronics chips, which is expected to be reduced as the flexible PCB assembly process become compatible with the unpackaged chips. Figure 3.7(c) shows a photo of ELM2.1 polyimide PCB before folding.

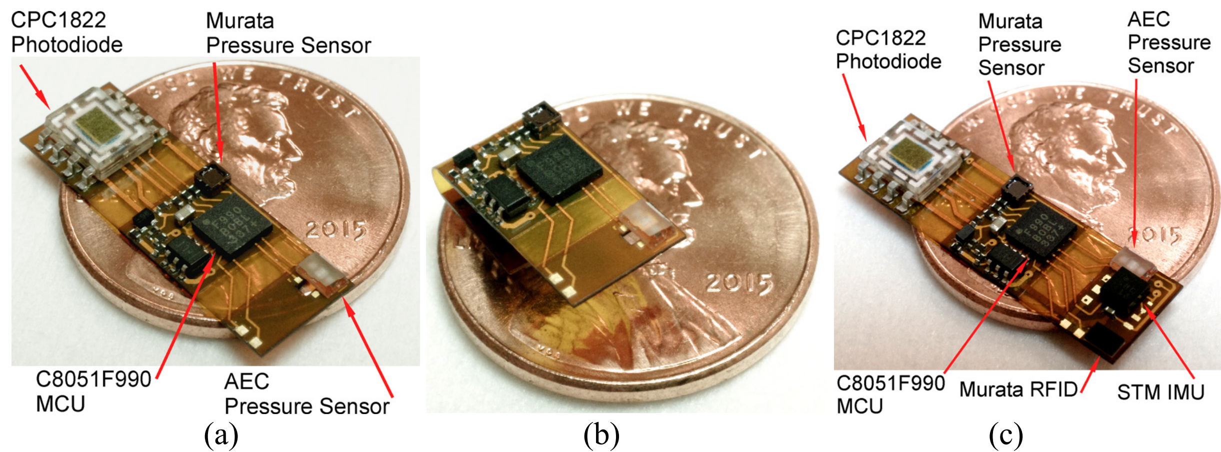

Figure 3.7: Photos of ELM2.0 and ELM2.1 before packaging. (a) Photo of ELM2.0 before folding. (b) Photo of the ELM2.0 after one fold. (c) Photo of ELM2.1 before folding.

The system is then encapsulated in 4-sided shells made from 17-4PH stainless steel, which provides impact and abrasion tolerance[1]. The steel shell was 1 mm thick, and was filled with transparent polymer for anti-corrosion protection. Three types of filler material are used – PDMS, silicone caulk and RTI epoxy – which are cured under different conditions and maintain different material properties. The filler polymer material also transfers the external pressure to the AEC pressure sensors with low attenuation. The transparent nature of the epoxy allows the optical charging and communication of the system. Figure 3.8 shows the encapsulation process for the silicone caulk filler material. During the process, the stainless steel shell is first diced into short tubes. A base layer of silicone is deposited inside the tube. The system is then buried into the silicone and extra silicone is deposited. The silicone is then cured at room temperature for 48 hours. Other filler materials have similar encapsulation processes but different curing conditions. Figure 3.9 shows a photo of the encapsulated ELM2.0 system filled with silicone caulk. The

[1] Folded systems were packaged by Dr. Yushu Ma and Ms. Neeharika Vellaluru.

encapsulated ELM2.0 system has a size of 9.5×9.5×6.5 mm^3 (L×W×H) with a volume of 586.6 mm^3.

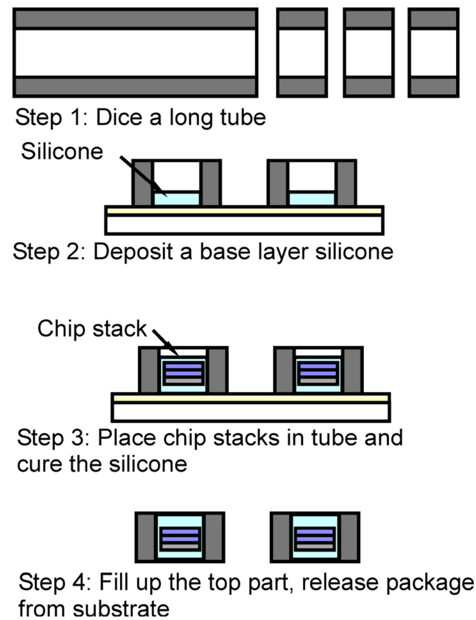

Figure 3.8: The encapsulation process of the ELM2.0 system with silicone as filler material.

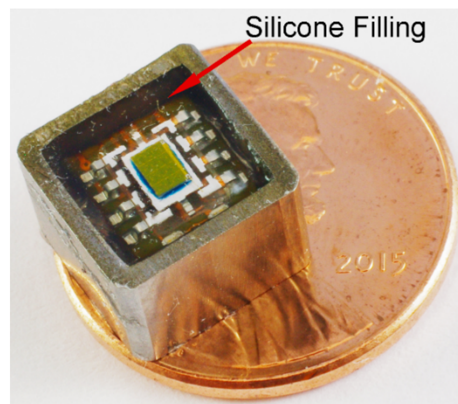

Figure 3.9: The ELM2.0 system in a steel package filled with silicone caulk.

3.3. ELM3.0 System Design

A third generation ELM system (ELM3.0) is developed to improve the manufacturing efficiency and extend the system's on-shelf storage time. The circuit schematic of ELM3.0 is

shown in Fig. 3.10. In the ELM3.0 system, the battery is soldered by the PCB manufacturer using commercial assembly equipment, which greatly reduces the system's manual assembly time. A mechanical slide switch is added in series with the battery, which can break the power during storage and eliminate the sleep mode current consumption. The system lifetime is thus greatly extended during storage. Since the battery is soldered, the flat ELM3.0 PCB is functional and does not need to be folded before use. A hydrophone site is added in parallel with the AEC pressure sensor and they share one MCU capacitance readout pin. A trial polyimide pressure sensor is fabricated and connected with one MCU capacitance readout pin, which is discussed in detail in Chapter 4. The unpackaged ELM3.0 system has an unfolded footprint of 28.8 × 8.6 mm^2 and a folded stack size of 9.5 × 8.7 × 7.9 mm^3.

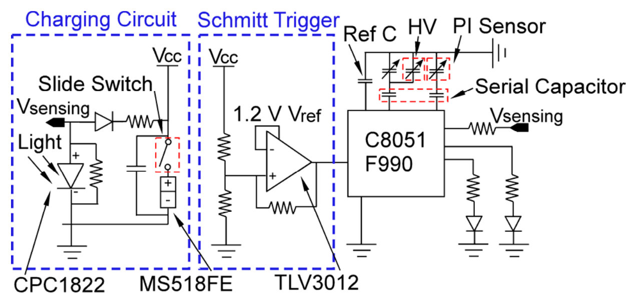

Figure 3.10: The circuit schematic of the ELM3.0 system.

Figure 3.11 shows the folded stack diagram of the ELM3.0 system. The ELM3.0 stack contains four layers in total. The first layer includes the photodiode and the LEDs for charging and communication. The second layer is the sandwiched battery. Since the battery is directly assembled by All Flex, the battery pins are kept and attached to the PCB. The third layer includes the MCU, comparator and other passive components. The fourth layer includes the slide switch, the site for the AEC pressure sensor and hydrophone, and the trial polyimide pressure sensor.

Similar to ELM2.0, an opening is cut on the fourth layer of the PCB so the diaphragm of the AEC pressure sensor or hydrophone is exposed to the exterior pressure.

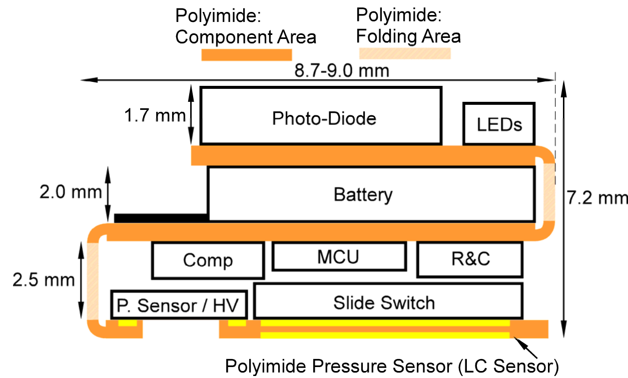

Figure 3.11: The folded stack diagram of the ELM3.0 system. The stack consists of four layers in total.

This system can be packaged in the same way as the ELM2.0 system. After folding, the system can be encapsulated in a 4-sided steel shell. The shell should be slightly larger than the shell of the ELM2.0 system to fit the system size. The package can be then filled with a transparent polymer for anti-corrosion protection. The compliant polymer can transfer the external pressure to the AEC pressure sensor as well as to the LC sensor.

In addition to the packaging approach described above, the ELM3.0 system can also be unfolded and then encapsulated in a transparent polymer mold for anti-corrosion protection[1]. The steel shell is not used in this approach. Two different types of filler material are used: silicone caulk and RTI transparent epoxy. The filler material helps transfer the external pressure to the AEC pressure sensors with low attenuation. The transparent nature of the epoxy allows the optical charging and communication of the system. Figure 3.12(a) shows the ELM3.0 molding process. During the molding process, an aluminum mold with several slots is first cut from bulk aluminum.

[1] Systems packaged by Mr. Andrew Trickey-Glassman.

Those slots are half filled with either RTI epoxy or transparent silicone caulk. The ELM3.0 systems are then dropped into those slots, and then the slots are filled with corresponding epoxy and cured. After curing, the systems are cut out from the mold. Figure 3.12(b) shows the ELM3.0 in RTI epoxy and Fig. 3.12(c) shows the ELM3.0 in silicone caulk.

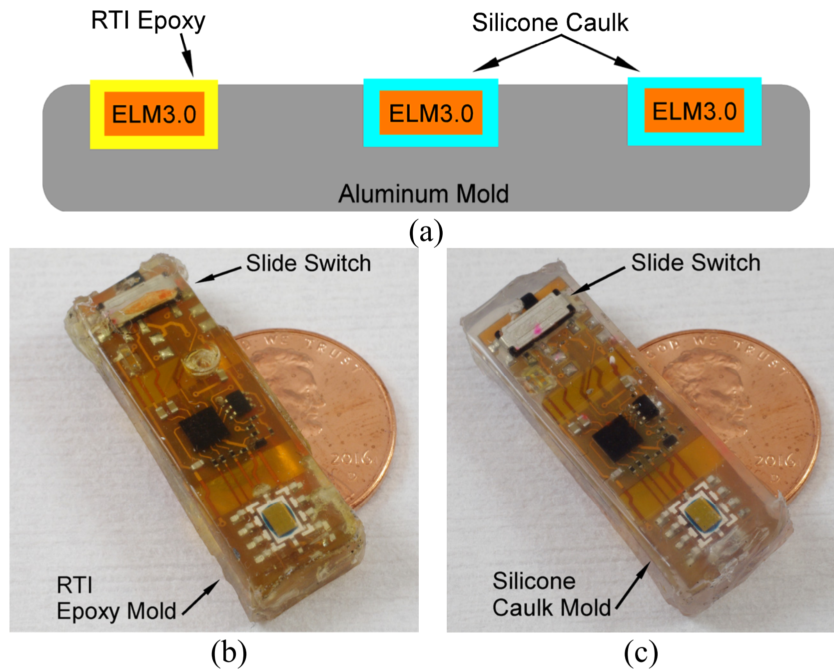

Figure 3.12: (a) The molding process of the ELM3.0 system. (b) Photo of the ELM3.0 system in RTI epoxy. (c) Photo of the ELM2.0 system in silicone caulk.

3.4. ELM2.0 and ELM2.1 Experimental Results from Laboratory Tests

3.4.1. Characterization of the ELM electronics

A. Transient Current Measurement

The transient current of ELM2.0 during each wake up event in the detection state was measured at 25°C, 125°C and 150°C. According to the datasheet, the wake up event in the detection state consisted of several steps. In the beginning, the 24.5 MHz precision oscillator in the MCU was turned on briefly and used to calibrate the RTC, then turned off to save power. Next,

the MCU was operated at 32 kHz for ≈1 seconds to perform several tasks. In the end, the temperature sensor, ADC and CS in the MCU were turned on briefly to measure environmental data. These data were written to the flash memory afterwards. In the test, the ELM was powered with 2.7 V supply and triggered into the detection state with a modified wake-up period of ≈3 s for oscilloscope sampling. The transient current over several detection events was then converted to a voltage through a series resistor. The voltage was amplified via a feedback amplifier and then picked up by an oscilloscope (Fig. 3.13). The closed-loop gain of the feedback amplifier is 102. The original current values were then converted back with the amplification gain and series resistance.

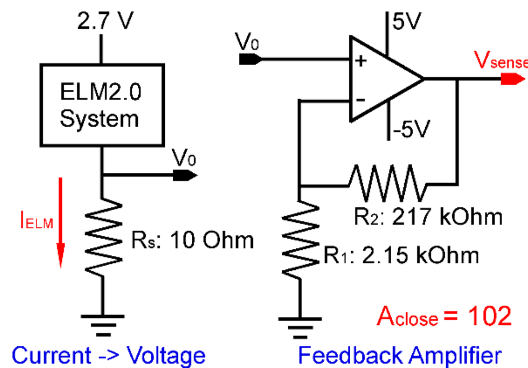

Figure 3.13: The amplification circuit for ELM3.0 transient current measurement.

The converted original transient currents are plotted in Fig. 3.14(a). According to the plot, the system stayed in the active state for 1.18s in each detection event, and the static active current I_{on} was measured to be 151 µA at 125°C. Figure 3.14(b) and Fig. 3.14(c) shows a magnified view in the beginning and end of each detection event. At the beginning of a detection event, the system consumed I_{ini} (387 µA at 125°C) during precision oscillator preparation followed by a short I_{pk1} (2.71 mA at 125°C) during RTC calibration. At the end of a detection event, the system consumed I_{pk2} during flash page erasing (1.05 mA at 125°C) followed by current spikes during flash writing

(< 1 mA at 125°C). According to the test results, the peak current appears during the RTC calibration and the flash memory writing.

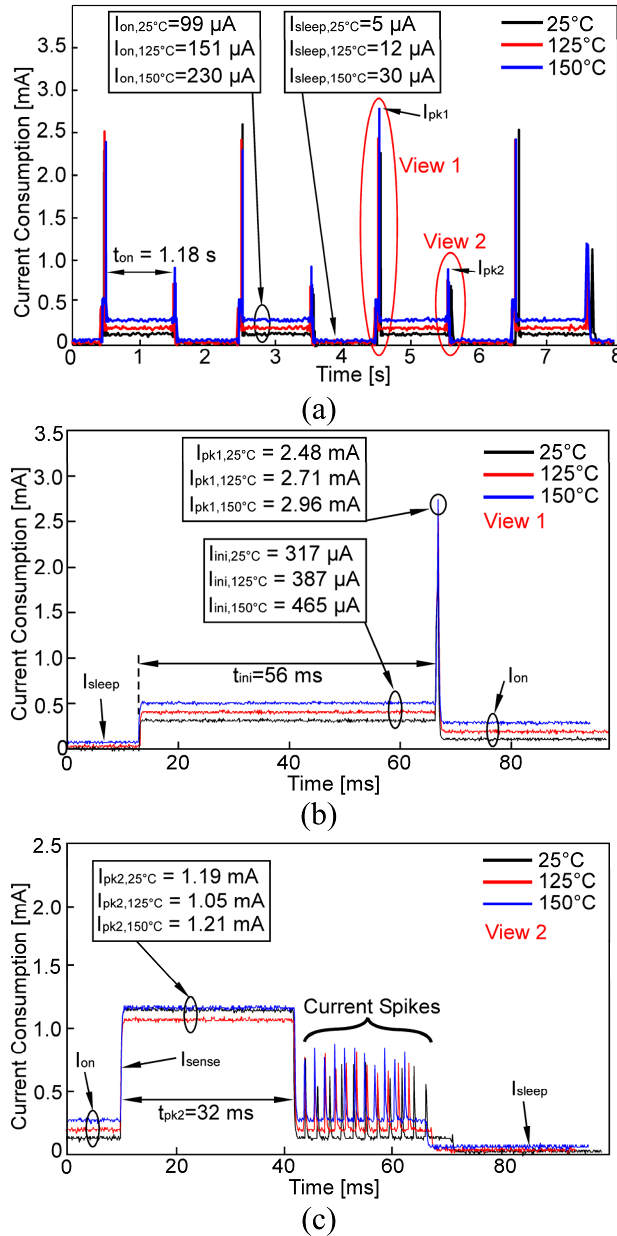

Figure 3.14: Transient current consumption of ELM at 25°C, 125°C and 150°C. (a) The transient current of ELM during multiple full detection events. The wake-up period is set ats 3 s for oscilloscope measurement. (b) The magnified view of the current at the beginning of each detection event, view 1. (c) The magnified view of the current at the end of each detection event, view 2.

B. Temperature Effect of Capacitance Sensing Module

The temperature effect of the capacitance sensing module in the C8051F990 MCU was tested. This module converts the input capacitance from the pressure sensor to digital data for storage and reporting. Such electronic circuits have inevitable temperature-dependent variations, which directly affect the recorded data for applications at varying temperatures if no calibration is performed. In the experiments, three ceramic capacitors with selected capacitance values (10 pF, 2 pF and 0.2 pF) were connected to the three MCU capacitance sensing ports. These capacitors have very small temperature variation of ±0-30 ppm/°C. During the tests, the system with these three capacitors was triggered into the detection state and then heated up in hot sand (Fig. 3.15a). The ramp up time was ≈30 minutes. The temperature went up to 125°C before cooling down. The temperature and capacitance at the three sensing ports were recorded during the tests.

The ΔC recorded by the MCU for all three capacitors from one test session is shown in Fig. 3.15(b). The test results show that the three ΔC curves are very close to each other. This indicates that the temperature-related variation of the MCU capacitance sensing module has negligible dependence on the capacitance value in the capacitance range of interest, and that the temperature-related gain error of the module, if any, can be safely ignored. The temperature-related ΔC can be considered offset error. This allows us to use a single ceramic capacitor in the ELM2.0 system as a reference to generate the offset data, and then to calibrate the temperature effect of the recorded sensor capacitance data by simply subtracting the offset data from it.

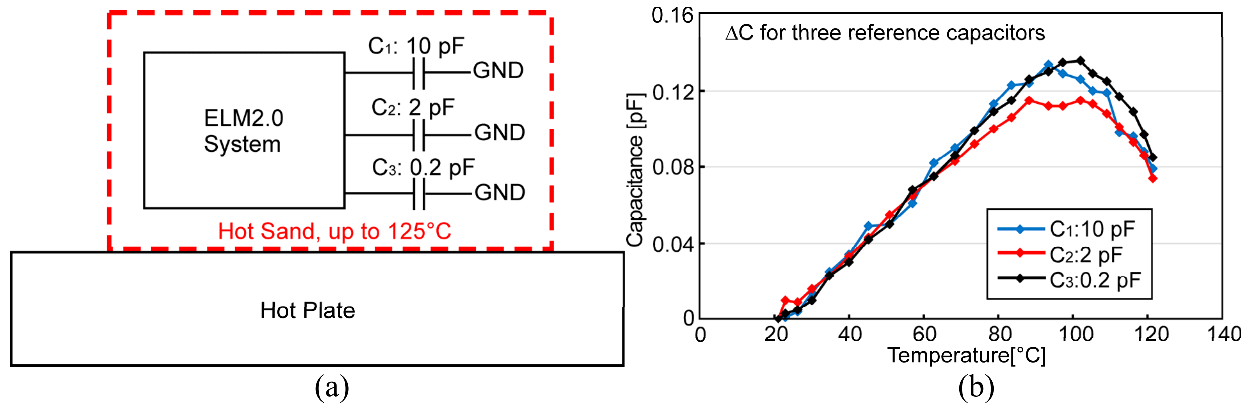

Figure 3.15: (a) Setup for characterization of temperature effect of the MCU capacitive sensing module. (b) Change of capacitance measured by the MCU at different temperatures for different ceramic capacitors.

C. Cycled Lifetime Test

A cycled lifetime test was performed to evaluate the maximum number of high temperature cycles (125°C) the system can survive before electronic failure. This number indicates the maximum number of times the system can be used in the oil well before replacement. In each test cycle, the ELM was triggered into the detection state and placed under 125°C for 3 hours, including 30 minutes ramp-up and 30 minutes ramp-down. The 3 hour duration was selected to emulate a real-time sensor deployment event, including lowering the sensor into the well, holding the sensor in the well for measurement and retrieving the sensor afterwards. After each cycle, the battery was recharged to 3 V and then disconnected from the system to save power. The system was then stored at room temperature for 21 hours until the next testing cycle. During the cycled lifetime test, the system survived 6 testing cycles and failed in the 7th cycle. This failure may have been caused by a flash memory writing error. The recorded temperatures over the 6 successful testing cycles are plotted in Fig. 3.16.

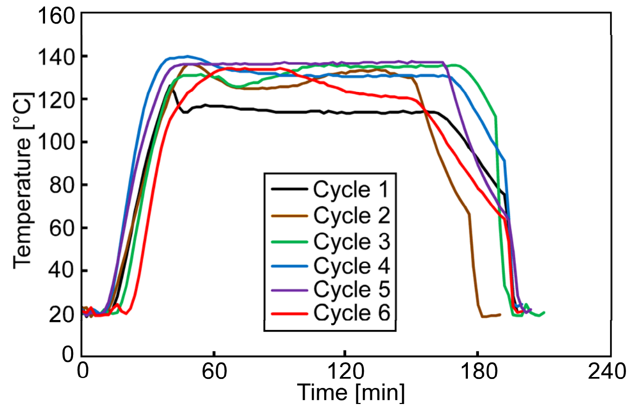

Figure 3.16: The measured temperature during the cycled lifetime test. The system survived six 3-hr test cycles at 125°C. The system failed at 7th cycle due to possible flash writing error.

3.4.2. Intermediate Pressure Tests of ELM2.0 System

The ELM2.0 system with the integrated Murata pressure sensor has been characterized under medium pressure (up to 380 psi or ≈2.6 MPa) at room temperature. The experiment setup includes a hydraulic hand pump from the High Pressure Equipment Company (HiP) to generate pressure, a chamber connected to the pump for loading the system PCBs without packaging, and a reference pressure transducer from Honeywell (0-1500 psi) for pressure monitoring. During the tests, the ELM systems with the integrated Murata sensor were loaded into the chamber, one in each session, and the pressure was elevated to 380 psi in ≈30 min. The pressure was held at 380 psi for ≈10 minutes (with a slow leak) and then released. The capacitance of the Murata pressure sensor was recorded by the ELM2.0 system and retrieved after the tests. Figure 3.17 shows the change in the recorded capacitance (ΔC) during the test, which was ≈8 pF for pressure change from 10-380 psi.

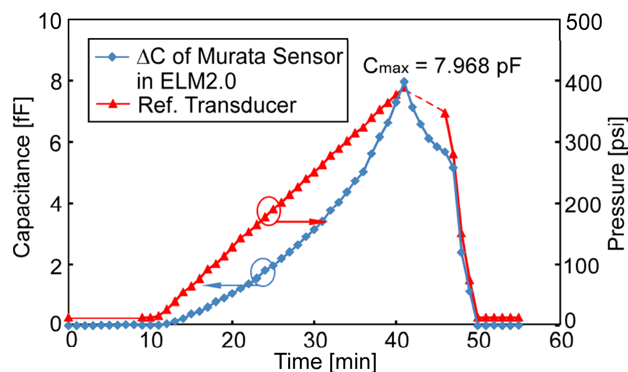

Figure 3.17: The change in capacitance of the Murata pressure sensor recorded by the ELM system and the applied pressure recorded by a reference pressure transducer during one of the medium pressure tests.

3.4.3. HPHT Tests of ELM2.0 System

The encapsulated ELM2.0 systems assembled with the U. Michigan pressure sensors were subjected to a series of HPHT tests. These HPHT tests were performed using the facility in RTI international, Durham-Raleigh, North Carolina and Total, Pau, France. The test setup was similar to that of the HPHT equipment described in Chapter 2. There were three major steps in the HPHT tests. In Step 1, the systems were fully charged at room temperature and then triggered into detection states in which temperature readings were taken at predefined time intervals. The systems were then sealed into plastic bags, each of which was filled with one of the selected test liquid media: API brine, Isopar^{TM}-L, silicone oil, Total mud and fracking gel (Table 3.2). The bags were made from a high grade nylon 6 film that can tolerate the target temperatures. In Step 2, the plastic bags, with the systems and test solutions inside, were inserted into HPHT testing cells that were filled with mineral oil. Following this, the cells were elevated to the target pressure. The temperature was then elevated in ≈30 min. After the prescribed soak time, the pressure was released and the temperature was allowed to cool off gradually for ≈30 min. In Step 3 the systems were retrieved from the cells, cleaned, and interrogated by optical means.

Table 3.2: Testing solutions used in the ELM2.0 HPHT tests.

Testing Solutions	Description
API Brine	$CaCl_2$ 2 wt% + NaCl 8 wt%
Isopar^{TM}-L	Synthetic isoparaffinic hydrocarbon solvent
Silicone Oil	Liquid silicone oil, electrically non-conductive, chemically inert
Total Mud	73.68% water, 15.26% Barite
Fracking Gel	Proprietary medium provided by Total, pH = 6.5

The ELM2.0 electronics and the U. Michigan pressure sensors survived the target HPHT conditions (up to 125ºC and up to 7200 psi) and Fig. 3.18 summarizes the testing results. Temperature and pressure data were successfully recorded and retrieved. The maximum test duration was 13 hours at temperatures as high as 100ºC, and 2 hours at temperatures as high as 125ºC, with pressure as high as 7200 psi for both temperature conditions; the ELM systems survived both types of tests. With regard to tolerance of corrosive environments, the ELM systems packaged using silicone caulk and RTI epoxy as filler material survived the HPHT tests in API brine and fracking gel. The ELM system packaged with silicone caulk survived HPHT tests in Total mud. However, both the RTI epoxy and PDMS were attacked by Isopar-L, leading to package failure. A special coating material is thus necessary to protect the system against Isopar-L. The stainless steel encasement survived all HPHT conditions separately in all testing solutions.

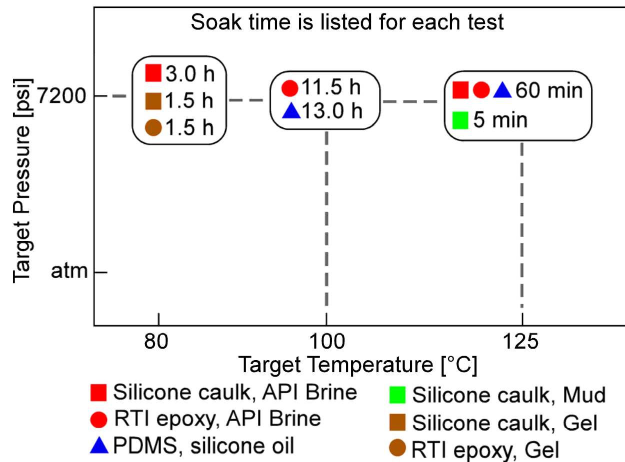

Figure 3.18: The summary of the successful HPHT tests performed on the ELM2.0 system. The testing durations are indicated.

The ELM2.0 system successfully reported the temperature and capacitance after the HPHT tests. One test was performed at 125°C temperature and 7200 psi pressure in an environment of API brine with 10 minutes hold time. The total duration of this test including temperature and pressure ramping up and ramping down was 1 hour. Temperature data was recorded every 2 minutes during the tests. The ELM system passed the test, and no leakage or deformation in the package was observed. The temperature data recorded by ELM, interpreted pressure data recorded by ELM, and the equipment temperature and pressure data were plotted in Fig. 3.19(a). The pressure data were interpreted from the measured capacitances, and the pressure interpretation method is described in detail in Section 3.5. In Fig. 3.19(b), the raw measurement data retrieved from the ELM system were plotted in four curves, including the temperature measured by the MCU (*Temp.MCU*), raw capacitance change measured from the pressure sensor (*ΔC.PS.Raw*), raw capacitance change measured from a reference capacitor (*ΔC.RefCap*), and corrected ΔC of the pressure sensor (*ΔC.PS.Cor*). The reference capacitor is located adjacent to the pressure sensor on the ELM circuit board and used for compensation of the offset in capacitance readout caused by

the temperature effect of the MCU capacitance sensing circuit. The corrected ΔC of the pressure sensor (*ΔC.PS.Cor*) is calculated by subtracting *ΔC.RefCap* from *ΔC.PS.Raw*:

$$\Delta C.Ps.Cor = (\Delta C.Ps.Raw) - (\Delta C.RefCap) \tag{3.1}$$

The resulting *ΔC.PS.Cor* is interpreted as the capacitance change caused by applied pressure P_A.

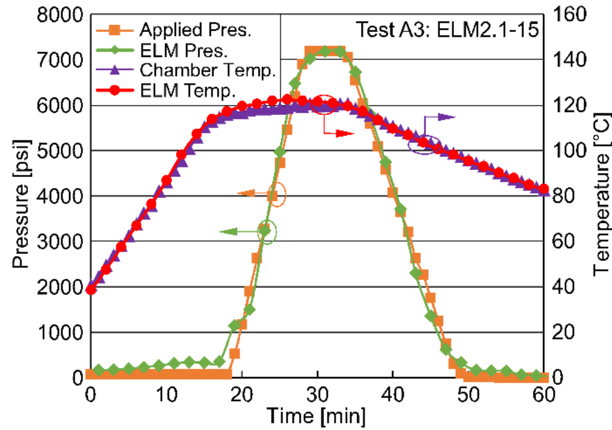

(a)

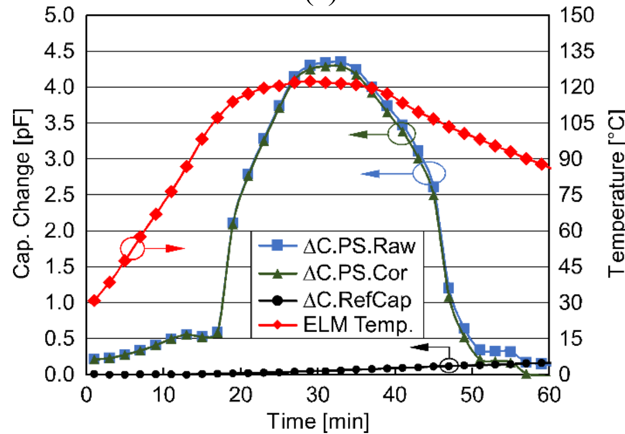

(b)

Figure 3.19: (a) Temperature and pressure reported by the testing equipment, and the MCU temperature and interpreted pressure from ELM2.0 during the HPHT test. (b) Temperature (*Temp.MCU*) and capacitance changes (*ΔC.PS.Raw*, *ΔC.PS.Cor*, and *ΔC.RefCap*) recorded by ELM during the HPHT test.

Another HPHT test was performed at a reduced temperature of 100°C and 7200 psi pressure in silicone oil for 13 hours. This test was used to evaluate the battery endurance under the HPHT condition. The system survived the test, and the temperature data were recorded and

matched machine logged data. The pressure data were recorded but invalid due to a possible pressure sensor malfunction. This test demonstrates that the electronics and the battery have over 13 hours of operational lifetime in combined HPHT conditions. Separately, a high temperature test was performed at 118°C in hot sand for 15 hours, and the system survived the test and recorded the temperature data. The long time endurance of the packaging material in a corrosive environment was not characterized in this set of tests, and needs to be further investigated.

3.5. Field Tests of ELM2.0 and ELM3.0 Systems in a Brine Well[1]

Field tests were performed on packaged ELM2.0 and ELM3.0 systems in a brine well in Vauvert, France to demonstrate the system functionality in an actual wellbore. The well was approximately 1800 m deep and there were trace hydrocarbons presented in the well. The ELM systems were placed inside stainless steel clamps developed by RTI. The two clamps were bolted around a plastic rod. The plastic rod was then attached to the end of a cable, which was operated by a winch and used to lower the plastic with the attached ELM systems into the brine well. An Openfield™ Technology apparatus that can record temperature and pressure was also attached to the plastic rod, and was used as a reference for the ELM reported data in each test. Fig. 3.20 shows the brine well test setup. During the test, the plastic with the attached ELM systems was lowered into the well with a maximum depth of 1235 m, hold for a certain period of time and then returned to the surface. In some of the tests, a temperature and pressure staircase was produced by stopping the cable at uniform time intervals. After the test, the clamp was gently removed and the device was rinsed before readout was initiated.

[1] Tests were performed by Mr. Andrew Trickey-Glassman and Dr. Tao Li with help from corporate collaborators.

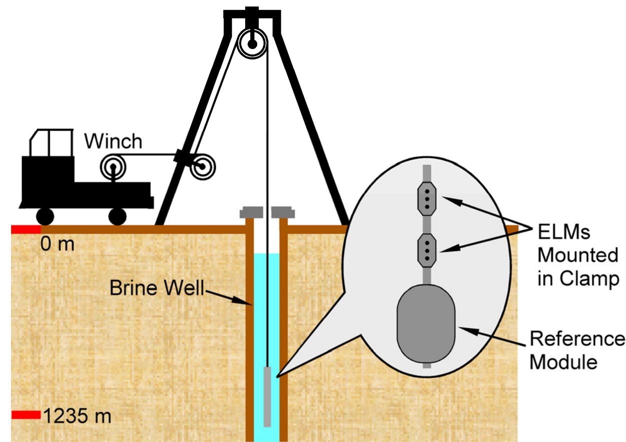

Figure 3.20: The setup for the brine well test. The ELMS are mounted in clamp together with reference modules. The systems were lowered into the well via the steel cable controlled by a winch. The systems were lowered to a maximum depth of 1235 m.

The brine tests were successfully and the ELM systems recorded the downhole temperature and pressure data. The longest duration the ELM system survived was 12 hours at a depth of 1235 m. In one of the pressure staircase tests (Test B6), the system was lowered to a depth of 1000 m in 60 min. It was then returned to the top, and Fig. 3.21(a) shows the recorded temperature and pressure. The recorded pressure was interpreted using the data from the Openfield^{TM} apparatus and the method described in Section 3.6. Other successful tests showed similar temperature and pressure data.

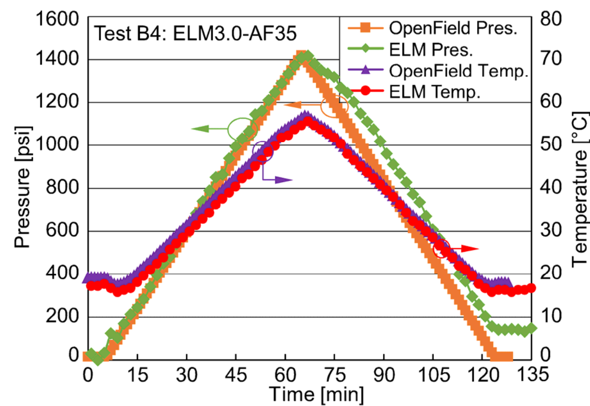

Figure 3.21: Pressure and temperature data collected by the Openfield^{TM} apparatus, and ELM temperature data and ELM converted pressure data.

3.6. ELM Pressure Sensor Calibration and Pressure Interpretation

3.6.1. A General Polynomial Calibration Method for MEMS Pressure Sensor

Micromachined pressure sensors typically show device-to-device variations in capacitance offset, pressure sensitivity, and temperature dependency. These variations may originate from residual stress in the diaphragms, packaging materials, and lead transfer. The C100 U. Michigan pressure sensor for 0-50 MPa pressure measurement has a small typical output capacitance (200-400 fF), and the factors noted above can cause a relatively significant shift of the sensor output capacitance. To achieve the pressure recording function in the downhole environment, a calibration method for individual systems is required, and needs to be performed before system deployment.

Normally, to accurately calibrate a sensor, the sensor should be swept across its dynamic range at many input data points, and the sensor output value at each input point should be recorded. The corresponding relationship between sensor output and input values can be obtained by fitting the recorded data obtained in the sweep. However, the ELM system can only take up to one measurement every minute, and it would take 72 minutes for each system to record all output capacitance if the pressure is swept every 100 psi from 0 to 7200 psi. This method is laborious and time consuming for calibration of a large number of sensors. To save the time for calibration, an efficient calibration method should be developed. With this method, only a few calibration measurements of a new sensor should be taken, and the relationship between the sensor output and input should then be estimated using these calibration data along with sensor data from past tests.

Progressive polynomial calibration is a general method for sensor calibration [Hor98]. Conventionally, the sensor transfer function is defined as the mathematical relationship between

sensor output and physical input. In this calibration method, a sensor transfer function is assumed to be linear [Hor98]:

$$g(x) = k \times x \tag{3.2}$$

in which k is pre-defined by users. The ratio k, which represents the ideal sensor sensitivity, is regarded as an average value for multiple sensors. The transfer function of a new sensor can be represented by an unknown transfer function $f(x)$. Since $f(x)$ is an unknown transfer function which may or may not be linear, in order to use g(x) to interpret the pressure, the output of the new sensor must be transformed by an n-point linearization function $h_n(x)$. After the output is transformed by $h_n(x)$, $g(x)$ can be used to interpret the physical input of the new sensor. To obtain $h_n(x)$, the n measured data points of the new sensor from $f(x_1)$ to $f(x_n)$ are used along with the expected output values from $g(x_1)$ to $g(x_n)$. The recursion expression for $h_n(x)$ is given by [Hor98]:

$$h_1(x) = f(x) + a_1 \tag{3.3a}$$

$$h_n(x) = h_{n-1}(x) + a_n \prod_{i=1}^{n-1} [h_i(x) - g(x_i)] \; (n \geq 2) \tag{3.3b}$$

in which $f(x)$ is the data point measured by the new sensor, a_1 is the offset calibration coefficient given by [Hor98]:

$$a_1 = g(x_1) - f(x_1) \tag{3.3c}$$

and a_n is the n-th calibration coefficient given by [Hor98]:

$$a_n = [g(x_n) - h_{n-1}(x_n)] \cdot \prod_{i=1}^{n-1} \left(\frac{1}{h_i(x_n) - g(x_i)} \right) \; (n \geq 2) \tag{3.3d}$$

As can be seen from the equations 3.2-3.3, this method uses an incremental approach to construct the linearization function $h_n(x)$, from $h_1(x)$, $h_2(x)$…to $h_{n-1}(x)$. The $h_0(x)$ is zero in this expression and n starts with 1. After each calibration step, the calibrated output from the new sensor progresses towards the idealized output of $g(x)$. The physical input of new sensor can then

be interpreted using $g(x)$ with minimal error. Some conventions for the number of calibration steps are: (1) When performing only one calibration step (n = 1), the calibration measurement is best taken with a reference input signal x_l at the middle of the input range; (2) When performing two calibration steps (n = 2), the calibration measurements should be done for input signals at about 25% and 75% of the input range; (3) For three or more calibration steps (n ≥ 3), generally a good linearization is obtained when the calibration points are selected in the following sequence: the first point at one end of the sensor range of operation, the second point at the other end of the range, and further calibration points halfway between two previously selected points [Hor98].

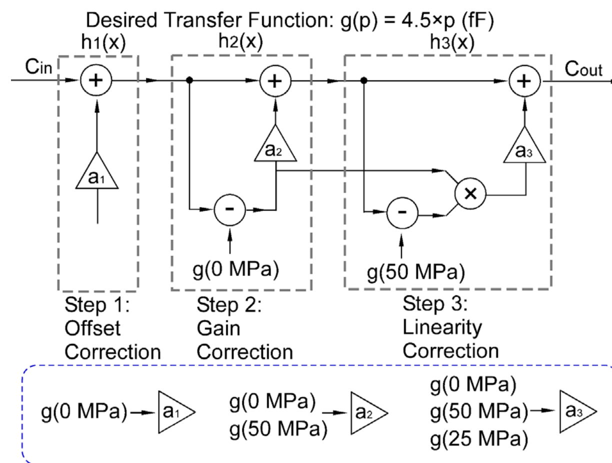

Figure 3.22: The proposed calibration procedure for the ELM2.0 system. These three steps correct offset, gain and linearity. More steps can be added to further correct the transfer function.

The effect of this calibration method is demonstrated by applying the linearization functions to the ELM pressure sensor data. The flow chart is shown in Fig. 3.22. A Labview™ program has been developed following the flow chart. In this demonstration, an arbitrary sensor transfer curve $g(p) = 4.5\times p$ (fF) is used, in which p is the environmental pressure in MPa. Three calibration points are selected at 0 MPa, 50 MPa, and 25 MPa respectively. These pressure values are selected following the conventions discussed above. The corresponding $h_n(p)$ after each linearization step is calculated following equations from (3.3a) to (3.3d). Figure 3.23(a) shows the

idealized transfer function *g(p)* and the output capacitance from a sample ELM system after each linearization step. According to the figure, the linearized output capacitance approaches the *g(p)* gradually. Figure 3.23(b) shows the interpreted pressure errors using the initial transfer function *g(p)* after each linearization step. The average pressure error of this system drops from 22.9 MPa to 2.1 MPa after the three-point calibration steps, which can be further reduced by adding more calibration points.

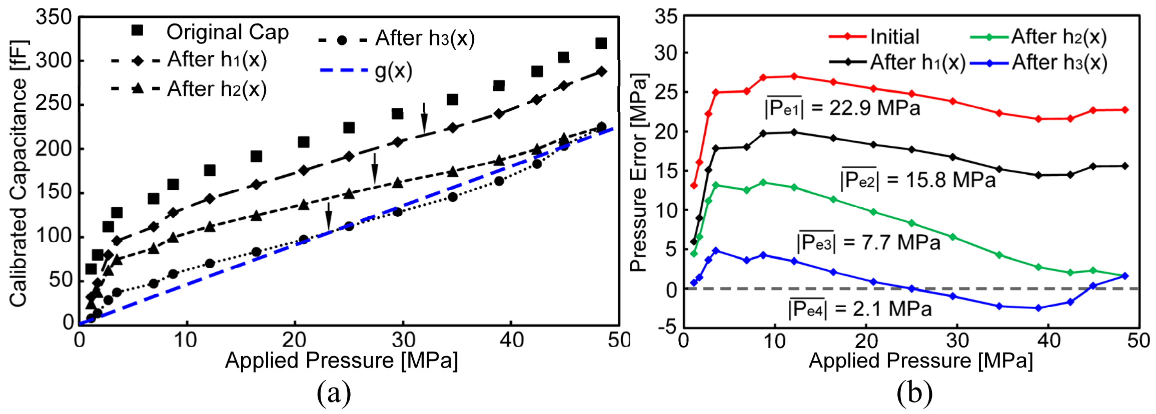

Figure 3.23: (a) The idealized transfer function *g(p)*, the output capacitance from an ELM2.0 system over applied pressure, and the capacitance after each step of calibration. (b) The interpreted pressure error using *g(x)* after each calibration step.

As described before, the sensor output depends not only on pressure, but also on operating temperature. The temperature dependency can also be calibrated by using a two-dimensional calibration. The basic principle is to fix the value in one dimension first (temperature in this case), and then proceed to calibrate the values in the other dimension (pressure). This process is repeated until the capacitances for all the temperature of interest are calibrated. The details of this two-dimensional calibration method are explained in [Hor98].

3.5.2. Calibration of the ELM3.0 Pressure Sensor Output

The pressure measured by ELM is interpreted using a similar method as described above, with a few alternations. First, the idealized transfer function *g(P)* is generated using data from sensors used in previous tests. In this case, the sensor data from system ELM2.1-15 in Pau Test A1 is used, and the machine pressure, interpreted pressure and the ELM capacitances are plotted in Fig. 3.24(a) and Fig. 3.24(b), respectively. Figure 3.24(c) shows the corrected capacitance change *ΔC.PS.Cor* at each applied pressure *P* during the first half of the test. A two-segment trend line is fitted, and its equation is given by:

$$g(P) = k_1 \cdot P \ (P < P_c) \tag{3.4a}$$

$$g(P) = k_2 \cdot P + C_0 \ (P \geq P_c) \tag{3.4b}$$

in which k_1 and k_2 are the slopes of the trend line in two segments, representing the responsivity in each segment, C_0 is the offset capacitance in the second segment, and P_c is the estimated contact pressure of the pressure sensor. This two-segment trend line is used because it represents the two operating modes of the capacitive pressure sensor: non-contact mode and contact mode. When the applied pressure exceeds the contact pressure P_c, the diaphragm of the sensor will be in contact with the substrate. The responsivity of the sensor reduces from k_1 to k_2 after contact. For this sensor, the calculated k_1 is 1.408 fF/psi, k_2 is 0.193 fF/psi, P_c is 1521 psi and C_0 is 2.142 pF. The fitted transfer function *g(P)* is then used to interpret the corrected ΔC of the pressure sensor over the full set of test data.

In the next step, the capacitance data from a new set of sensor data, in this case, the capacitance data from device ELM2.1-15 in Pau Test A3 is calibrated using the method described in Section 3.5.1. With a selected input pressure point (P_1 = 7190 psi) and its corresponding output

capacitance (C_1 = 4.356 pF), and assuming the transfer function passes (P_0 = 0, C_0 = 0), the calculated linearization function is:

$$h_1(x) = f(x) = C,\ a_1 = 0 \tag{3.5a}$$

$$h_2(x) = f(x) + a_2 \times f(x) = 0.708 \times f(x) = 0.708 \times C \tag{3.5b}$$

$$a_2 = \frac{g(x_2) - h_1(x_2)}{h_1(x_2) - 0} = \frac{g(P_1) - h_1(P_1)}{h_1(P_1) - 0} = \frac{3.085 - 4.356}{4.356} = -0.292 \tag{3.5c}$$

The capacitances from this sensor in Pau Test A3 are then processed by $h_1(x)$ and $h_2(x)$, and interpreted using *g(P)* from (3.5a) and (3.5b). The pressure data from the system ELM3.0-AF35 in the Vauvert Test B4 shown in Fig. 3.21 was also interpreted with the same method.

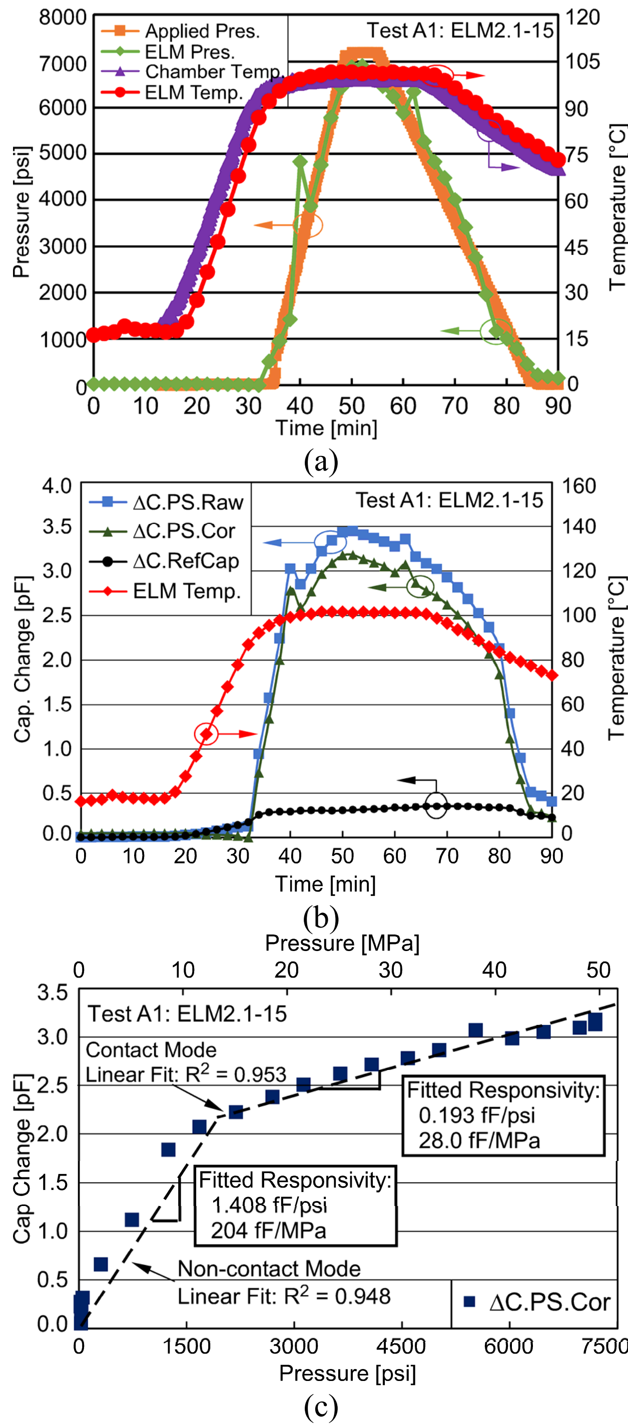

Figure 3.24: (a) Temperature and pressure reported by the testing equipment, and the MCU temperature and interpreted pressure from ELM2.0-15 in Pau Test A1. (b) Temperature (*Temp.MCU*) and capacitance changes (*ΔC.PS.Raw*, *ΔC.PS.Cor*, and *ΔC.RefCap*) recorded by ELM2.0-15 in Pau Test A1. (c) Corrected ΔC of the pressure sensor (ΔC.PS.Cor) plotted as a function of the applied pressure for ELM in HPHT test. The trend line uses second order fit.

3.7. Capacitance Drift Analysis and Correction

During the long duration HPHT tests, the ELM capacitance readout continued to drift after the temperature and pressure were stabilized. Figure 3.25(a) shows an example of the capacitance drift during one of the HPHT tests (Vauvert Test B2, device AF-3-4). This capacitance drift could lead to inaccurate interpretation of the pressure sensor output, and should be corrected based on quantitative analysis. To characterize the capacitance drift and understand the causes, the drift rate (DR), which is defined as the capacitance drift per minute, was calculated for each long duration test. The drift rate was assumed to be constant at the test conditions during each test. The system used to generate the data plotted in Fig. 3.25(a) was held at 55°C, 1400 psi for 10 hours, and the drift rate for *ΔC.PS.Raw* was 0.28 fF/min, and for *ΔC.RefCap* was 0.11 fF/min. Figure 3.25(b) shows the temperature reported by the equipment and MCU, pressure reported by the equipment and interpreted pressure from the ELM data without drift correction during that test. The interpreted pressure drifted up for a significant amount while the environment pressure was stable during the hold. This section summarizes the capacitance drift behavior for the long duration tests performed to date, provides a preliminary analysis of the contributing factors based on the principal component analysis method, and presents a preliminary method to correct the capacitance drift.

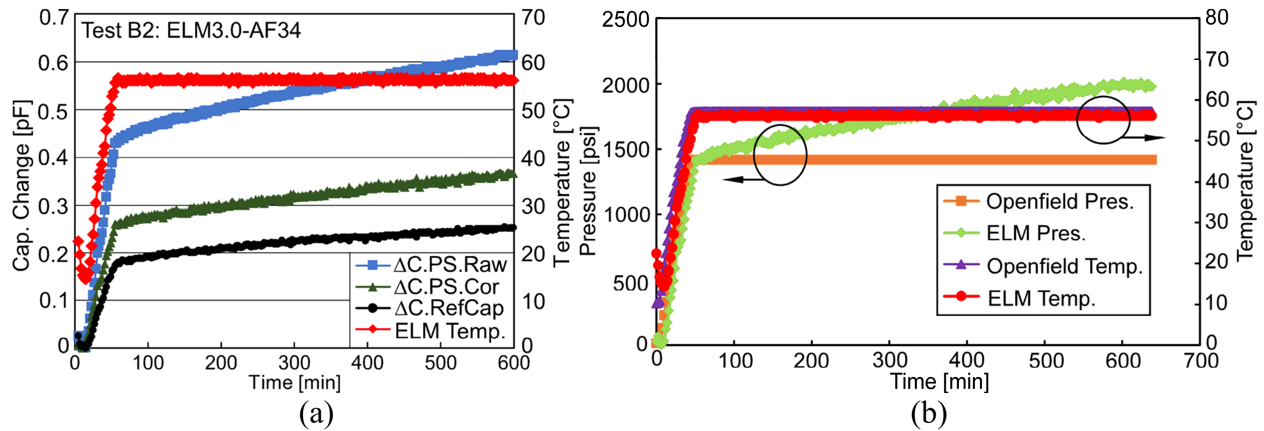

Figure 3.25: (a) Temperature (*Temp.MCU*) and capacitance changes (*ΔC.PS.Raw*, *ΔC.PS.Cor*, and *ΔC.RefCap*) recorded by one ELM during the HPHT test at 55°C, 1400 psi. The capacitance drifted over time with certain drift rate. (b) Temperature and pressure reported by the testing equipment, and the MCU temperature and interpreted pressure from the ELM3.0 during the HPHT test. The interpreted pressure drifted up while the environment pressure was stable.

3.7.1. Characterization of CDC Drift Rate at Varying Temperatures

The CDC drift rate under high temperature and atmospheric pressure was characterized first to understand temperature dependency of the MCU CDC drift rate. In the tests, two ELM3.0 systems were used, ELM3.0-DR1 and ELM3.0-DR2. The ELM3.0-DR1 was assembled with 0.2 pF and 10 pF ceramic capacitors, and the ELM3.0-DR2 was assembled with 0.2 pF and 2 pF ceramic capacitors. The different capacitance values could provide information about the correlation between capacitance drift rate and capacitance scale. The systems were fully charged and placed in hot sand at 100°C for up to 10 hours. The capacitances of both capacitors were recorded, and the drift rate of the recorded capacitances was calculated by fitting the capacitance data at stabilized temperature & pressure. Figure 3.26(a) and (b) shows the recorded capacitance and calculated drift rate for the ELM3.0-DR1 system. The 10 pF capacitor had a drift rate of 0.028 fF/min and the 0.2 pF capacitor had a drift rate of 0.027 fF/min, which were both much smaller than the drift rate observed in the HPHT tests. Similar drift rates were obtained from the system

ELM3.0-DR2 in the tests. Additionally, long duration tests were performed on other ELM3.0 systems at room temperature or intermediate temperature (70°C), at atmospheric pressure, and similar drift rates were obtained. These test results are summarized in Fig. 3.26(c). Based on these, the CDC drift rate does not have strong correlation with either temperature or capacitance scale.

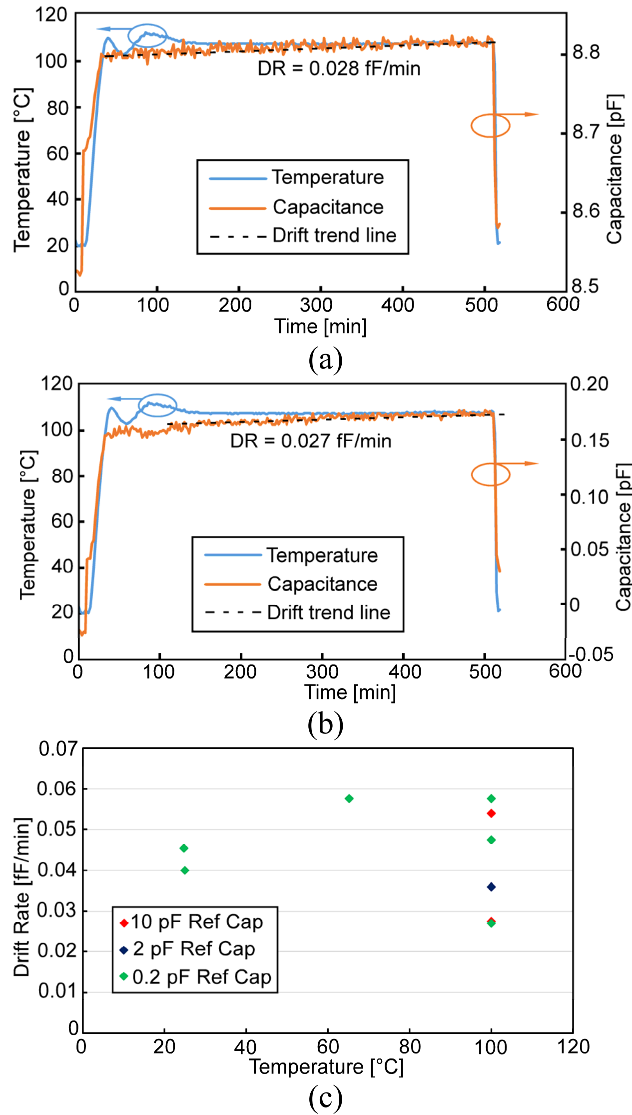

Figure 3.26: (a) The recorded temperature and capacitance of the 10 pF reference capacitor, with a capacitance drift rate of 0.028 fF/min; (b) The recorded temperature and capacitance of the 0.2 pF reference capacitor, with a capacitance drift rate of 0.027 fF/min. The ELM3.0-DR1 was used for the tests. (c) Summary of capacitance drift rates of the ELM reference capacitors from the in-lab long duration test.

The drift rate for ELMs with C100 sensor from the previous long duration HPHT tests in the laboratory and in the brine well were calculated using the same method and summarized in Table 3.3. The ELMs with C100 sensor were packaged in RTI epoxy. These data show a better consistency in the drift rate at the temperature and pressure conditions in the tests. It can be directly

observed from the table that the systems with bare board tested at atmospheric pressure have much slower drift rate than the packaged systems tested under high pressure. Other hidden trends in this dataset cannot be interpreted directly, and require further quantitative analysis.

3.7.2. Principal Component Analysis of the ELM Drift Rate and Drift Rate Correction

To quantitatively understand how the different environmental parameters are contributing to the capacitance drift, principal component analysis (PCA) is performed on the data in Table 3.3. The PCA is a statistical method to find out the patterns of the high dimensional data and is normally used for data compression purpose [Web-Smi]. The principal component, which is a vector calculated from the given data set, represents the correlations between different variables inside the data. In this drift rate analysis, PCA is used to find out the correlations between temperature, pressure and the capacitance drift rate. The calculated principal components can be used to predict the drift rate for a new test. Typically, a large dataset is preferred for the PCA method, which is not yet available at the time of this dissertation. The work presented below serves as a first attempt to address this drift issue. Additional PCA can be performed in the future when more data becomes available.

Table 3.3: The summary of the ELM3.0 drift rate from various tests.

Test Name & Condition	Device ID	Packaging Material	Pressure Sensor / Capacitor	Raw C_0 from MCU ($C_{0,MCU}$)	Drift rate (fF/min)	Estimated Drift for 10 Hours (fF)
In-Lab Test						
CDC Drifting Test 1, 100°C, atm, hot sand	ELM3.0-DR1	Bare Board	10 pF Cap	17.187 pF	0.028	16.8
			0.2 pF Cap	7.387 pF	0.027	16.2
	ELM3.0-DR2	Bare Board	2 pF Cap	9.187 pF	0.036	21.6
			0.2 pF Cap	7.387 pF	0.048	28.8
CDC Drifting Test 2, 100°C, atm, mineral oil	ELM3.0-DR1	Bare Board	10 pF Cap	17.187 pF	0.054	32.4
			0.2 pF Cap	7.387 pF	0.057	34.2
LC Sensor Test, 25°C, atm, pump oil	ELM3.0-Jan	Bare Board	0.2 pF Cap	7.387 pF	0.040	24
France Test						
Vauvert Test B2, 55°C, 1400 psi, brine well	ELM3.0-AF3.4	RTI Epoxy	AEC C100	7.262 pF	0.28	168
			0.2 pF Cap	7.387 pF	0.11	66
	ELM3.0-AF3.5	RTI Epoxy	AEC C100	7.262 pF	0.29	174
			0.2 pF Cap	7.387 pF	0.17	102
Vauvert Test B5, 68°C, 1750 psi, brine well	ELM3.0-AF3.4	RTI Epoxy	AEC C100	7.262 pF	0.33	198
			0.2 pF Cap	7.387 pF	0.14	84
	ELM3.0-AF3.6	RTI Epoxy	AEC C100	7.262 pF	0.41	246
			0.2 pF Cap	7.387 pF	0.16	96

For the principal component analysis in this study, the temperature, pressure and the drift rate are used in order to find their correlation. The other factors, such as pressure sensor type, packaging material and ambient solution are ignored at this time since they are non-parametric. Then for any data point $\boldsymbol{X_i}$ used in the PCA, the dependencies include temperature T_i, pressure P_i, and drift rate DR_i, which can be written as $\boldsymbol{X_i} = (T_i, P_i, DR_i)$. The bolded font means this variable is a vector with multiple elements. In the PCA, the temperature (25-100°C) and pressure (0-7200 psi) are first scaled between 0-1 using equations:

$$T_1 = \frac{T_0 - 25}{100 - 25} = \frac{T_0 - 25}{75};\ P_1 = \frac{P_0}{7200} \tag{3.6}$$

in which T_0 is the temperature before scaling, T_1 is the temperature after scaling, P_0 is the pressure before scaling and P_1 is the pressure after scaling. This step ensures that the relative weights of those variables are not biased. Second, for each data point in the dataset $\{\boldsymbol{Xi}\}$, the mean values of temperature, pressure, and drift rate are subtracted from their measured values, respectively. This

process helps to center the mean value of the full dataset at (0, 0, 0) in the temperature, pressure, and drift rate axes. Third, a 3×3 covariance matrix C_{ov} of the temperature, pressure, and drift rate is calculated using the processed data:

$$C_{ov} = \begin{bmatrix} C_{ov}(T,T) & C_{ov}(T,P) & C_{ov}(T,DR) \\ C_{ov}(P,T) & C_{ov}(P,P) & C_{ov}(P,DR) \\ C_{ov}(DR,T) & C_{ov}(DR,P) & C_{ov}(DR,DR) \end{bmatrix} \tag{3.7}$$

in which each element is the covariance between two variables. As an example, the covariance between temperature T and pressure P is given by:

$$C_{ov}(T,P) = \frac{\sum_{i=1}^{n}(T_i - \overline{T})(P_i - \overline{P})}{n-1} \tag{3.8}$$

in which the $\overline{T}$ and $\overline{P}$ are the average temperature and pressure, respectively, and n is the total number of measurements. The T and P in equation 3.9 can be replaced with any of the T, P or DR variable. Apparently, the matrix C_{ov} is symmetric along the diagonal since for any two variables such as T and P, $C_{ov}(T, P) = C_{ov}(P, T)$.

The next step is to find the principal component of the dataset $\{\boldsymbol{X_n}\}$. The principal component is defined as the direction in which the projections of the data set have the largest variance. For an individual data point $\boldsymbol{X_i}$, the projected scalar value on to unit vector $\boldsymbol{u_1} = (u_{1T}, u_{1P}, u_{1DR})$ is:

$$\boldsymbol{u_1^T} \cdot \boldsymbol{X_i} = T_i u_{1T} + P_i u_{1P} + DR_i u_{1DR} \tag{3.9}$$

in which $\boldsymbol{u_1}^{\boldsymbol{T}}$ indicates that the column vector $\boldsymbol{u_1}$ is transposed into a row vector, so that it can be multiplied with a column vector to obtained the projected scalar value. The variance of the projected scalar values from $\boldsymbol{X_1}$ to $\boldsymbol{X_n}$ projected onto the unit vector $\boldsymbol{u_1}$ can be calculated by:

$$\frac{1}{n-1}\sum_{i=1}^{n}\{\boldsymbol{u}_1^T\boldsymbol{X}_i-\boldsymbol{u}_1^T\overline{\boldsymbol{X}}\}^2=\frac{1}{n}\sum_{i=1}^{n}\{\boldsymbol{u}_1^T(\boldsymbol{X}_i-\overline{\boldsymbol{X}})\}^2=\boldsymbol{u}_1^T C_{ov}\boldsymbol{u}_1 \tag{3.10}$$

in which the C_{ov} is the covariance matrix of the dataset $\{\boldsymbol{X_n}\}$ given by:

$$C_{ov}=\frac{1}{n-1}\sum_{i=1}^{n}(\boldsymbol{X}_i-\overline{\boldsymbol{X}})(\boldsymbol{X}_i-\overline{\boldsymbol{X}})^T \tag{3.11}$$

in which $\overline{\boldsymbol{X}}$ is the vector comprised of the mean value the dataset $\{\boldsymbol{X_n}\}$ with 3 component ($\overline{T}$, $\overline{P}$, $\overline{DR}$). This equation 3.12 is exactly same as equation 3.8 with *T*, *P* and *DR* written in the vector form of $\boldsymbol{X_i}$.

To find the unit vector $\boldsymbol{u_1}$ that identifies the maximum variance $\boldsymbol{u_1}^T C_{ov}\boldsymbol{u_1}$, and with the constraint of $||\boldsymbol{u_1}|| = 1$ since $\boldsymbol{u_1}$ is defined as a unit vector, the Lagrange multiplier method can be used. Basically, to find the maximum value of a multi-variable function *f(x, y)* with a known condition *g(x, y)* = 0, at the maximum point (x_0, y_0), there must exist a parameter λ such that:

$$\nabla f(x_0,y_0)+\lambda\nabla g(x_0,y_0)=0 \tag{3.12}$$

in which $\nabla f(x_0,y_0)$ is the gradient of *f(x,y)* at (x_0,y_0) and $\nabla g(x_0,y_0)$ is the gradient of *g(x,y)* at (x_0,y_0). This equation has to be satisfied since *g(x, y)* = 0 defines a curve in the xy plane. Then since *g(x, y)* = 0 is always true, the vector $\nabla g(x,y)$ at any point on that curve must be orthogonal to the curve; otherwise the *g(x, y)* will change since there is a gradient component along the curve. At the same time, since (x_0,y_0) is the maximum value of *f(x,y)*, $\nabla f(x_0,y_0)$ must also be orthogonal to the *g(x,y)* = 0 curve; otherwise there would be a point adjacent to (x_0, y_0) on the curve with larger value along the direction of $\nabla f(x_0,y_0)$. Figure 3.27 illustrates the maximum point of function *f(x,y)* on the curve *g(x,y)* = 0.

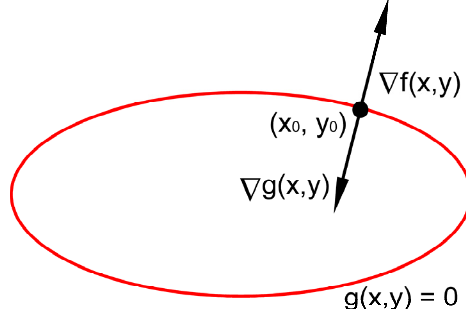

Figure 3.27: The illustration of the LaGrange multiplier method. At the maximum point (x_0, y_0), both $\nabla f(x_0,y_0)$ and $\nabla g(x_0,y_0)$ should be orthogonal to the $g(x,y) = 0$ curve.

To implement this Lagrange method, the Lagrange function $L(\boldsymbol{X}, \lambda)$ can be defined:

$$L(\boldsymbol{X}, \lambda) = f(\boldsymbol{X}) + \lambda g(\boldsymbol{X}) \tag{3.13}$$

and by setting $\nabla_X L(\boldsymbol{X}, \lambda) = 0$, which is the gradient of $L(X, \lambda)$ for all the variables in $\boldsymbol{X}$, equation 3.13 is obtained and the corresponding $\boldsymbol{X}$ and λ can be calculated. In this application, the Langrage function is constructed as:

$$L(X, \lambda) = \boldsymbol{u}_1^T C_{ov} \boldsymbol{u}_1 + \lambda_1(1 - \boldsymbol{u}_1^T \boldsymbol{u}_1) \tag{3.14}$$

in which λ_1 is the Lagrange multiplier, and $g(x) = \lambda_1(1-\boldsymbol{u}_1^T\boldsymbol{u}_1)$. To maximize the variance $\boldsymbol{u}_1^T C_{ov} \boldsymbol{u}_1$, the gradient of the above equation with respect to $\mathbf{u}_1$ should be equal to zero, and the following relationship is obtained:

$$C_{ov}\boldsymbol{u}_1 = \lambda_1 \boldsymbol{u}_1 \tag{3.15}$$

which indicates that the $\boldsymbol{u}_1$ is indeed the eigenvector of the covariance matrix of the dataset C_{ov}. Indeed, if $\boldsymbol{u}_1^T$ is multiplied on both side of the equation above, then:

$$\boldsymbol{u}_1^T C_{ov} \boldsymbol{u}_1 = \lambda_1 \tag{3.16}$$

which means that the maximum value of the variance $\boldsymbol{u}_1^T C_{ov} \boldsymbol{u}_1$ is indeed the eigenvalue λ_1 of the covariance matrix C_{ov}. As a result, the eigenvector with the largest eigenvalue is the principal

component, and along that direction the variance of the projected data is maximized [Web-Smi, Bis06].

The principal component analysis method described above is performed on the recorded data listed in Table 3.3. The calculated principal component for this data set is (0.856, 0.240, 0.457) with an eigenvalue of 0.013. Figure 3.28(a) and (b) show the selected data set and the principal component between drift rate and temperature, and between drift rate and pressure, respectively. From the calculated principal component and the plots, the drift rates for these pressure sensors show a strong correlation with temperature and with pressure. As shown in Fig. 3.26(c), the temperature is proved to be irrelevant with the CDC drift rate. Based on past experience, the drift rate of the sensor is also assumed to have minimum dependence on temperature for the purpose of this analysis, although additional experiments are necessary in the future to verify this assumption. The high correlation between the temperature and drift rate is assumed to be caused by the coincidence that the temperature and pressure in the HPHT tests were changed together with each other. Based on this assumption, the temperature variable is not considered further in the preliminary drift rate estimation.

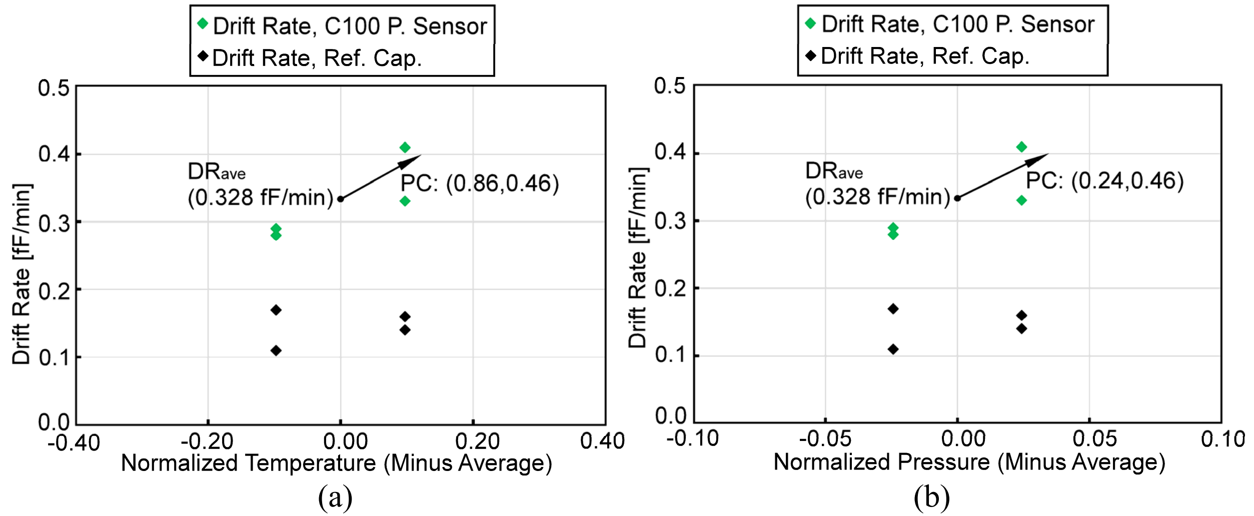

Figure 3.28: (a) The drift rate, normalized temperature for C100 sensors and their reference capacitors, and the principal component between drift rate and temperature. (b) The drift rate, normalized pressure for C100 sensors and their reference capacitors, and the principal component between drift rate and pressure. The data are from the C100 sensors and their reference capacitors.

With this high correlation between the variables, the calculated principal components can then be used to predict the drift rate for ELMs with C100 sensor, given the specific pressure. The principal component of the C100 sensor data is (0.856, 0.240, 0.457). With the known pressure, the drift rate can be estimated by:

$$DR_{est} = DR_{ave} + P_{nor} \times w_3 / w_2 \tag{3.17}$$

in which DR_{est} is the estimated drift rate, DR_{ave} is the average drift rate for C100 sensor at the average pressure, which is 0.328 fF /min at 1575 psi in this data set, P_{nor} is the normalized pressure, w_2 is the pressure value of the principal component, and w_3 is the drift rate value of the principal component. Using this equation, for the HPHT test conducted at 55°C, 1400 psi, the estimated drift rate is 0.282 fF/min and for the HPHT test conducted at 68°C, 1750 psi, the estimated drift rate is 0.374 fF/min. The average drift rate for the reference capacitors in these tests is 0.145 fF/min, which is assumed to be constant since the drift rates for the reference capacitors are close to each other, and do not have high correlation with temperature or pressure. Table 3.4 summarizes

the calculated drift rates of the ELMs with the C100 sensor. The actual drift rates derived from measurement data of the HPHT tests are also listed in the table for comparison, and they are very close to the calculated drift rates.

Table 3.4: The estimated drift rate for the AEC C100 device under different testing condition.

<table>
<tr><th>Test and Condition</th><th>System ID</th><th>Packaging</th><th>Sensor Type</th><th>Actual Drift rate</th><th>Estimated Drift rate using PCA</th></tr>
<tr><td rowspan="4">Vauvert Test B5, 55°C, 1400 psi, brine well</td><td rowspan="2">ELM3.0-AF3.4</td><td rowspan="2">RTI Epoxy</td><td>AEC C100</td><td>0.28</td><td>0.282</td></tr>
<tr><td>0.2 pF Cap</td><td>0.11</td><td>0.145</td></tr>
<tr><td rowspan="2">ELM3.0-AF3.5</td><td rowspan="2">RTI Epoxy</td><td>AEC C100</td><td>0.29</td><td>0.282</td></tr>
<tr><td>0.2 pF Cap</td><td>0.17</td><td>0.145</td></tr>
<tr><td rowspan="4">Vauvert Test B5, 68°C, 1750 psi, brine well</td><td rowspan="2">ELM3.0-AF3.4</td><td rowspan="2">RTI Epoxy</td><td>AEC C100</td><td>0.33</td><td>0.374</td></tr>
<tr><td>0.2 pF Cap</td><td>0.14</td><td>0.145</td></tr>
<tr><td rowspan="2">ELM3.0-AF3.6</td><td rowspan="2">RTI Epoxy</td><td>AEC C100</td><td>0.41</td><td>0.374</td></tr>
<tr><td>0.2 pF Cap</td><td>0.16</td><td>0.145</td></tr>
</table>

To correct the capacitance drift based on the calculated drift rate, the amount of the capacitance drift over time is first calculated, and then subtracted from the raw capacitances for both the C100 pressure sensor and the reference capacitor:

$$\Delta C.PS.Cor(t)_{DR} = \Delta C.PS.Raw(t) - DR_{est,C100} \times t \quad (3.18a)$$

$$\Delta C.PS.Ref(t)_{DR} = \Delta C.PS.Ref(t) - DR_{est,Ref} \times t \quad (3.18b)$$

in which $\Delta C.PS.Cor(t)_{DR}$ is the C100 capacitance change at time t with drift correction, $\Delta C.PS.Raw(t)$ is the raw C100 capacitance at time t, $DR_{est,C100}$ is the calculated drift rate for C100 pressure sensor, $\Delta C.PS.Ref(t)$ is the corrected reference capacitor capacitance with drift correction, $\Delta C.PS.Raw(t)$ is the raw reference capacitor capacitance and $DR_{est,Ref}$ is the calculated drift rate for the reference capacitor. The corrected pressure sensor capacitance $\Delta C.PS.Cor(t)$ for both drift and CDC temperature dependence is then calculated by:

$$\Delta C.PS.Cor(t) = \Delta C.PS.Cor(t)_{DR} - \Delta C.PS.Ref(t)_{DR} \quad (3.19)$$

Figure 3.29(a)-(b) show the *ΔC.PS.Cor* with and without the drift rate correction for two of the systems tested in Vauvert. From the data, it can be clearly seen that the capacitance drift is reduced by significant amount with the drift rate correction.

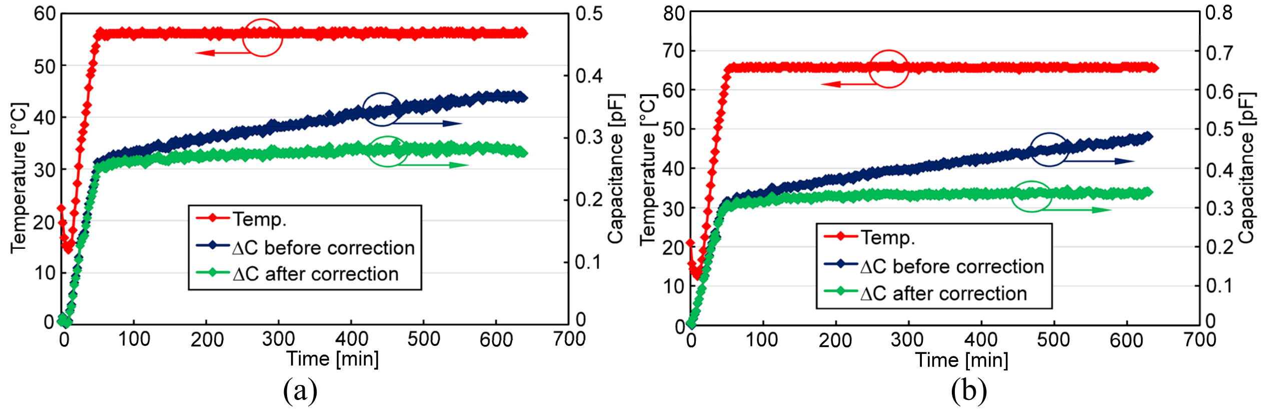

Figure 3.29: (a) The *ΔC.PS.Cor* with and without drift rate correction for ELM3.0-AF3.4, Vauvert test B2. (b) The *ΔC.PS.Cor* with and without drift rate correction for ELM3.0-AF3.6 Vauvert test B5. Both systems were assembled with C100 pressure sensors and packaged in RTI epoxy.

The drift rate correction described above assumes that the environmental pressure is known to the user before the correction. Indeed, the environmental pressure in the actual deployment is unknown to user, and the only information recorded by the ELM system is the capacitance. To correct the capacitance drift and interpret the pressure, a numerical approach can be used. An average drift rate can be derived from the calibration data such as those in Fig. 3.25. The capacitance drift based on this average drift rate can be subtracted from the *ΔC.PS.Raw:*

$$\Delta C.PS.Cor(t)_{DR1} = \Delta C.PS.Raw(t) - DR_{ave,C100} \times t \tag{3.20}$$

in which $\Delta C.PS.Cor(t)_{DR1}$ is the corrected raw capacitance after this first correction iteration, $\Delta C.PS.Raw(t)$ is the initial raw capacitance, and $DR_{ave,C100}$ is the average drift rate. The estimated external pressure P_1 can then be determined from $\Delta C.PS.Cor(t)_{DR1}$ using the pressure interpretation method described in Section 3.5. In the next iteration, to obtain more accurate

capacitance drift amount, the drift rate at pressure P_1 can be calculated by equation 3.18, and the updated raw capacitance is:

$$\Delta C.PS.Raw(t)_{DR2} = \Delta C.PS.Raw(t) - DR_{P1,C100} \times t \tag{3.21}$$

in which $\Delta C.PS.Raw(t)_{DR2}$ is the corrected raw capacitance after second correction step and $DR_{P1,C100}$ is the drift rate at pressure P_1. By repeating this process, the capacitance $\Delta C.PS.Cor(t)_{DRn}$ obtained after nth correction step will converge. With the numerical method described above, the drift of the ELM capacitance output with unknown pressure can be corrected, and can be used for accurate pressure interpretation.

3.7.3. Pressure Interpretation for the Long Duration Test Result

The ELM pressure sensor data after drift correction using the approach in Section 3.7 is then calibrated to generate the pressure information. To quickly find the transfer curve and interpret the pressure from each individual ELM system, the calibration method from section 3.6.1 can be used. Firstly, the capacitance is assumed to be a linear function *g(P)* to the pressure. When the applied pressure is lower than the touch mode pressure of the sensor diaphragm (20 MPa typically), the capacitance can be approximated as a linear function with the applied pressure. Therefore, this assumption is valid for C100 sensors which were used in the brine well test at a relatively low pressure (<2000 psi). Then the idealized transfer function is:

$$g(P) = k \times P \tag{3.22}$$

which is obtained by fitting a typical set of pressure and capacitance data from one of the systems, in this case, the ELM3.0-AF34 from Vauvert Test B2. The calculated k is 0.182 fF/psi and the pressure interpreted using the transfer function *g(P)* is plotted in Fig. 3.30(a). Then this transfer function is used as *g(x)* to interpret the data for other systems. For example, for ELM3.0-AF36 in

Vauvert Test B5, the linearization function $h_1(x)$ and $h_2(x)$ is calculated following equations from 3.3a to 3.3d using a selected input pressure point (P_1= 1751 psi) and its corresponding output capacitance (C_1= 0.316 pF), assuming the transfer function curve passes ($P_0 = 0$, $C_0 = 0$):

$$h_1(x) = f(x) = C,\ a_1 = 0 \tag{3.23a}$$

$$h_2(x) = f(x) + a_2 \times f(x) = 1.01 \times f(x) \tag{3.23b}$$

$$a_2 = \frac{g(x_2) - h_1(x_2)}{h_1(x_2) - 0} = \frac{g(P_1) - h_1(P_1)}{h_1(P_1) - 0} = \frac{319 - 316}{316} = 0.01 \tag{3.23c}$$

The capacitance values are then processed by $h_1(x)$ and $h_2(x)$ and interpreted using $g(P)$. Fig. 3.30(b) shows the interpreted pressure of this device. The interpreted pressure follows closely with the equipment pressure before holding, then the pressure starts to drift up slowly.

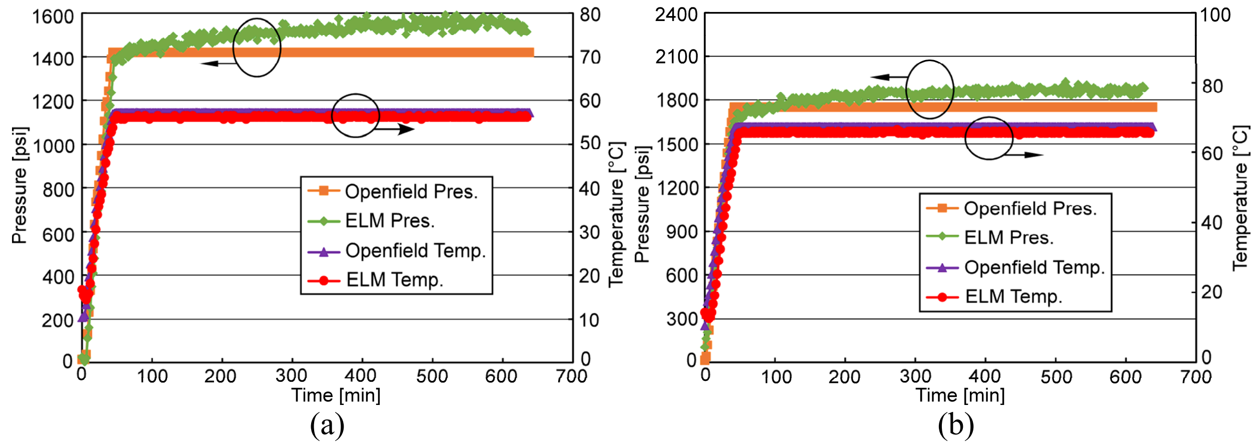

Figure 3.30: (a) Temperature and pressure reported by the testing equipment, and the MCU temperature and interpreted pressure for Vauvert Test B2, AF-34 device. (b) Temperature and pressure reported by the testing equipment, and the MCU temperature and interpreted pressure for Vauvert Test B5, AF-36 device. Linear transfer curve is used to interpret the environment pressure.

The linear transfer curve fitting is justified by the physical principal of the capacitive pressure sensor, and the general sensor calibration method; however, small residue drift after drift correction of the sensor data can still significantly affect the pressure interpretation results. As shown in Fig. 3.30(a) and (b), the interpreted pressure still drifts upward at stabilized environment

pressure even after the drift rate was corrected by PCA method. As an attempt to improve pressure interpretation accuracy while coping with the capacitance drift effect, a modified data calibration method using a second order polynomial function as the fitting transfer curve is proposed:

$$g(C) = a \cdot C^2 + b \cdot C \tag{3.24}$$

in which a and b are transfer function coefficients. This function curve passes the origin point ($C_0 = 0$, $P_0 = 0$). Instead of running the progressive calibration method from section 3.5.1, two additional measurement points (C_1, P_1), (C_2, P_2) are used as calibration points to determine the coefficient a and b. This approach allows higher flexibility on the shape of the transfer function. The pressure P_1 can be selected at a high pressure, and P_2 can be selected at an intermediate pressure during the test. Using this method, the pressure from ELM3.0-AF34 in Vauvert Test B2 and ELM3.0-AF36 in Vauvert Test B5 are re-interpreted. Figure 3.31(a) and (b) show the temperature and interpreted pressure for those two devices, and Fig. 3.31(c) and (d) show the fitted transfer function P(C) for each device. During the pressure rising region, the interpreted pressure follows the environmental pressure. During the pressure stabilized region, the drifting is slower than the pressure generated by linear transfer curve fitting. This indicates that the second order transfer function has better fitting behavior in this application.

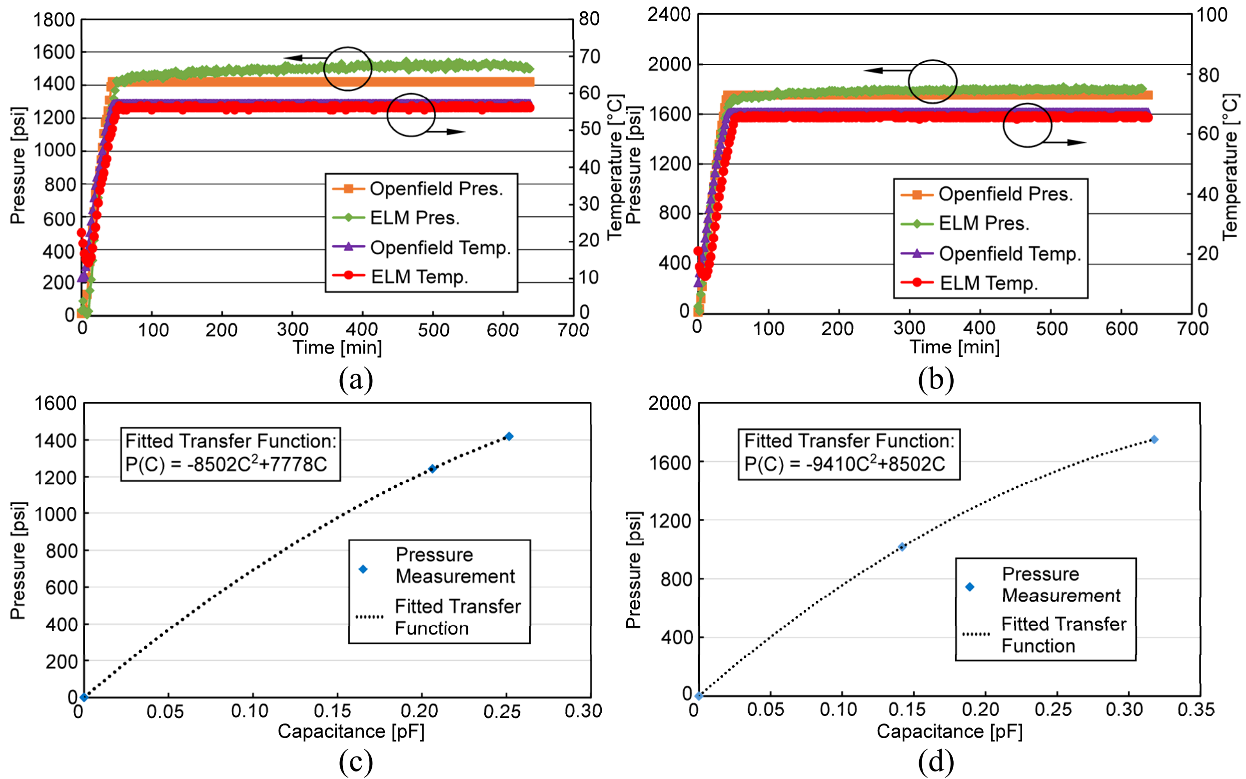

Figure 3.31: (a) Temperature and pressure reported by the testing equipment, and the MCU temperature and interpreted pressure for Vauvert Test B2, AF3.4 device. (b) Temperature and pressure reported by the testing equipment, and the MCU temperature and interpreted pressure for Vauvert Test B5, AF3.6 device. (c) The fitted second order transfer function for pressure interpretation used in (a). (d) The fitted second order transfer function for pressure interpretation used in (b).

3.8. Discussion and Summary

The second generation of environmental logging microsystems (ELM2.0) was developed for downhole temperature and pressure logging up to 125°C and 50 MPa, using commercial off-the-shelf electronics, MEMS pressure sensors and lithium-based batteries. Capacitive MEMS pressure sensors with output capacitance change on the order of pF were integrated into the ELM systems. The microsystem was assembled on a flexible substrate and folded with a stack size of 7.2×6.6×6.5 mm^3. This volume was mainly consumed by the larger battery that was necessary to accommodate the higher current draw, and the surface mount chip packages that were necessary

to facilitate the commercial PCB assembly. The microsystem had a maximum operating time of 15 hours at 118°C. The microsystem was hermetically encapsulated to tolerate corrosive and high-pressure environments, with low pressure attenuation and good optical transparency. The ELM2.0 system successfully passed multiple HPHT tests in different types of ambient solutions.

The third generation of environmental logging microsystems (ELM3.0) was developed based on ELM2.0 to improve the manufacturing efficiency and extend the system's on-shelf storage time. The Seiko battery was directly assembled into the system with commercial equipment to reduce the system assembly time. By including a slide switch in series with the battery, the system storage lifetime was significantly improved. A low-cost polyimide pressure sensor was also included in the ELM3.0 system. The ELM3.0 system was packaged in either silicone caulk or RTI epoxy mold.

A brine well test was performed on the ELM2.0 and ELM3.0 systems. Both the ELM2.0 and ELM3.0 systems successfully survived the brine well test, with a maximum depth of 1235 m and a maximum duration of 12 hours. The pressure was interpreted using a polynomial progressive calibration method. The temperature and interpreted pressure closely matched the data recorded by a commercial Openfield™ apparatus.

The measured capacitance has a slow drift over time during the HPHT test. A principal component analysis of the temperature, pressure and the drift rate was proposed and performed to identify the correlations between the drift rate and environmental factors. The calculated principal component was used to correct the drifted capacitance for ELMs with C100 sensors. The corrected capacitance data was then interpreted to provide the environmental pressure information for the long duration tests.

CHAPTER 4:

INVESTIGATION OF A POLYIMIDE PRESSURE SENSOR

This chapter describes the concept and preliminary study of a low-cost polymer pressure sensor that can be directly fabricated on an ELM flexible PCB for downhole pressure monitoring. As described in Chapter 3, the MEMS pressure sensor used for downhole pressure monitoring provides excellent resolution over a large pressure range; however, it also has a need for a specialized fabrication process. Where high resolution pressure sensing is not required, an innovative, low-cost polyimide pressure sensor (LC sensor) is proposed and investigated.

The LC sensor can be fabricated with standard flexible PCB technology with two metal plates on the top and bottom as the sensing electrodes, and the sandwiched polyimide as the dielectric material. Preliminary FEA was performed on LC sensors with different geometries and sizes, and the results showed that the ΔC of a 20 mm^2 polyimide sensor over 0-50 MPa can achieve 165 fF, which can be detected by a C8051F990 MCU. An LC sensor used for initial testing was designed and fabricated on the ELM3.0 system and connected with the C8051F990 MCU through capacitance sensing pins. A high pressure test was performed on the ELM3.0 system with the LC sensor.

The experimental validation showed a large drift in capacitance readout was observed. A baseline correction method was proposed to correct the capacitance drift over time. After this correction, a capacitance change of 205 fF was observed over 0-50 MPa applied pressure. Other

factors that can affect the sensor capacitance output, including temperature, material selection for the dielectric and metal, and other environmental factors are also discussed in this chapter.

4.1. Motivation and Literature Review

Traditionally, the high temperature fabrication process used for some types of MEMS pressure sensors makes it difficult to integrate these sensors with silicon-based electronics on a single chip. As a result, these MEMS pressure sensors are often individually attached to the electronics in a hybrid form, which increases the manufacturing cost and limits the yield. To eliminate this integration step and improve system yield, polymer has been used as the structural material for pressure sensor fabrication [Ped97]. Compared with MEMS pressure sensors fabricated with inorganic material, the polymer-based pressure sensors are attractive for post-processing on a CMOS chip because the conventional bonding step is eliminated. For the ELM system, the polymer pressure sensor can potentially be fabricated directly on the flexible PCB by using the polymer material of the PCB substrate as the sensor structure. Either a diaphragm type or cavity-less type pressure sensor can be implemented. Both types are reviewed below. Some common limitations of polymer pressure sensors include the lower operating temperature and anti-corrosion capability [Ko07, Ped97].

Several research institutes have worked on diaphragm type pressure sensors with polymer as the sensing diaphragm. Ko et al. have reported a piezo-resistive pressure sensor using SU-8 as the sensing diaphragm (Fig. 4.1(a)) [Ko07]. This sensor was fabricated using a glass wafer and a silicon wafer. A thick layer of SU-8 was used to define the sidewalls of the cavity on the glass wafer. A thin SU-8 layer was deposited and patterned on a silicon wafer to form the diaphragm, which was followed by deposition and patterning of polysilicon for the piezoresistors. The silicon wafer was then flipped and bonded to the thick SU-8 layer to seal the cavity, and the silicon

substrate was etched away to release the SU-8 diaphragm. This sensor had a size of 150 × 150 μm^2 and a diaphragm thickness of 9 μm, and a pressure dynamic range of 0-350 KPa. Pederson et al. have reported a capacitive pressure sensor using polyimide as the diaphragm was developed (Fig. 4.1(b)) [Ped97]. During the fabrication process, a polyimide layer was first deposited and patterned on top of an aluminum sacrificial layer on silicon substrate. The polyimide was then released by wet etching of the aluminum and backside etching of the silicon substrate. This pressure sensor had a side length of 700 μm and a diaphragm thickness of 16 μm. A 100 KPa external pressure applied resulted in 100 fF output signal.

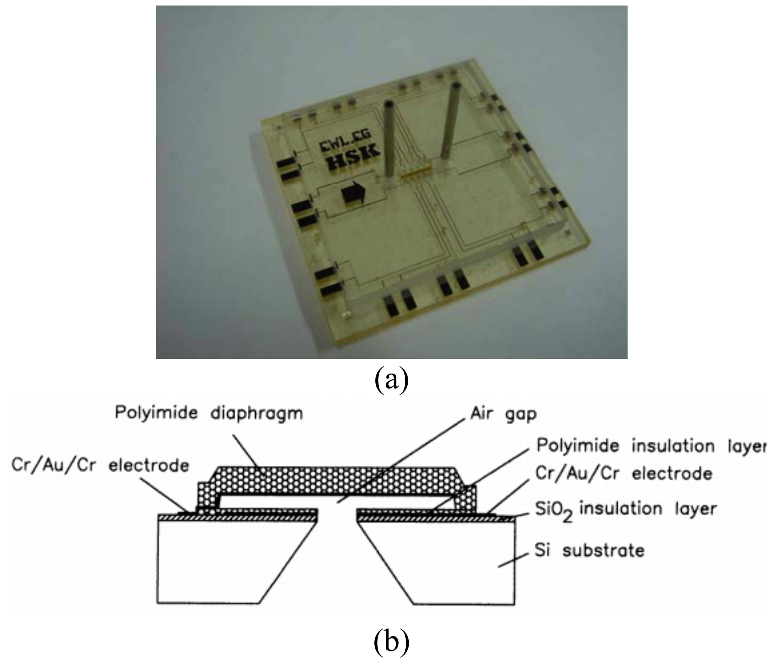

Figure 4.1: (a) The photo of the piezo-resistive pressure sensor fabricated using SU-8 at National Cheng Kung University [Ko07]. (b) The schematic of the polyimide capacitive pressure sensor fabricated in at the University of Twente [Ped97].

The polymer-based pressure sensors described above were operated below 1 MPa, which is significantly lower than the target downhole pressure in this thesis (50 MPa). The polymer diaphragm structure of these pressure sensors would have large deformations under even moderate

pressure because of the low Young's modulus of these polymer materials (SU-8 or polyimide), which would cause the diaphragm to come into contact with the counter surface. Once the diaphragm is in the contact mode, the sensitivity will drop significantly and quickly saturate due to the compliant nature of the polymer. This makes it very difficult, if possible at all, to use polymer diaphragms at the target high pressure. As a result, to use polymer as the structural material of downhole pressure sensor, a sensor structure that can accommodate a much higher pressure dynamic range needs to be investigated. A reasonable capacitance change over the dynamic range and relatively small footprint are also preferred for integration with the existing ELM system.

Takahata et al. have reported a micromachined capacitive pressure sensor using a cavity-less structure [Tak08]. The sensor was constructed with two metal plates and in between these plates was sandwiched polyurethane, a liquid rubber elastomeric layer (Fig. 4.2). The polyurethane layer was deformed under applied pressure, which caused the capacitance between the metal plates to change. The polyurethane had a thickness of 38 μm and an active area of 4 mm^2. Although operating only up to 340 KPa due to the low Young's modulus of the polyurethane (67 KPa at initial condition), this sensor eliminated the diaphragm structure and a sealed cavity to provide higher robustness. With a stiffer sandwiched polymer, a similar sensor structure can achieve higher dynamic range.

The cavity-less type pressure sensor is preferred over the diaphragm type for the higher dynamic range, which is necessary for downhole application. It could be fabricated with the layers in the flexible PCB without additional fabrication steps.

4.2. Device Concept and Theoretical Analysis

A polyimide pressure sensor that can be fabricated directly on a flexible PCB is proposed for downhole pressure monitoring. This can potentially meet the goal of eliminating the hybrid assembly of the MEMS pressure sensor for applications that do not need high resolution in pressure sensing, thus significantly reducing the manufacturing cost and increasing the yield. The proposed LC polyimide sensor structure consists of a top and a bottom metal layer as capacitance electrodes, and a sandwiched polyimide layer as the dielectric. When external pressure is applied, the dielectric polyimide layer will be compressed and the capacitance between the electrodes will increase, and this capacitance change can be picked up by the MCU capacitance sensing module (Fig. 4.2). The polyimide film is squeezed from top and bottom, and no diaphragm bending is involved, assuming the pressure is evenly distributed, so a linear pressure response up to a very high pressure is expected. This sensor can be directly fabricated on the ELM system since the top and bottom metal and the sandwiched polyimide layers are standard structures available in the ELM flexible PCB fabrication process. The Dupont™ Pyralux® AP8515, which is a double sided copper-clad laminate material with sandwiched polyimide film, is used as the flexible circuit material for the ELM system [Dup17].

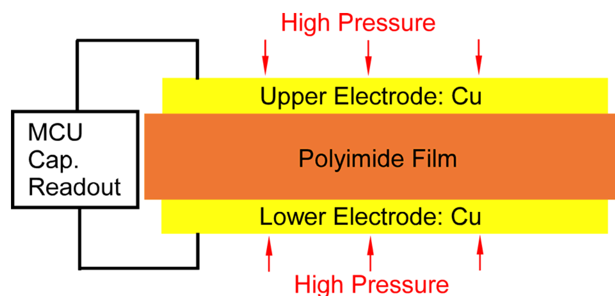

Figure 4.2: The schematic of the low-cost polyimide sensor.

In the simplest scenario, under room temperature, this polyimide pressure sensor can be modeled as a parallel plate capacitor and the initial capacitance is given by:

$$C = \varepsilon_0 \varepsilon_r \frac{A}{d} \tag{4.1}$$

in which ε_0 is the vacuum permittivity (8.85×10^{-12}), ε_r is the relative permittivity of the polyimide film (3.4 from DuPont's datasheet), A is the sensor area (assume to be 20 mm^2) and d is the thickness of the polyimide between the metal layers (24.5 μm defined by the fabrication process). The calculated initial capacitance between the sensing electrodes under zero pressure is 24.6 pF. When external pressure is applied to the top and bottom of the sensor, the polyimide film is squeezed and the distance between the upper and lower electrodes is decreased, thus causing a capacitance increase. The relative change of the electrode distance can be estimated by:

$$\frac{\Delta d}{d} = -\frac{p}{E} = -\frac{50\,\text{MPa}}{4.8\,\text{GPa}} \approx -1\% \tag{4.2}$$

in which p is applied pressure (target downhole pressure 50 MPa) and E is the Young's modulus of polyimide film (4.8 GPa from DuPont's datasheet). The change in capacitance can be calculated with the change in polyimide thickness by:

$$\Delta C = \Delta(\varepsilon_0 \varepsilon_r \frac{a^2}{d}) = -\varepsilon_0 \varepsilon_r a^2 \frac{\Delta d}{d^2} + \varepsilon_0 \varepsilon_r 2a \frac{\Delta a}{d} = C_0(-\frac{\Delta d}{d}) + C_0(2\frac{v\Delta d}{a}) \tag{4.3}$$

in which C_0 is the initial sensor capacitance and v is the Poisson's ratio, which is 0.34 for polyimide film [Dup17]. Using this equation, at 50 MPa applied pressure, the capacitance of the sensor is increased by 247 fF. This value can be detected by the C8051F990 MCU capacitive sensing module, which has a maximum resolution of 1 fF.

The above equations assume the material is perfect linear elastic and the upper and lower surfaces are not bounded. The sensor used in this effort is sandwiched between two copper plates.

Indeed, for an elastomer layer sandwiched between two rigid plates, a higher compression stiffness is expected than without those rigid boundaries. The deformation equation for a rectangular layer of homogeneous elastomer bounded with two rigid plate is given by [Tak08, Lee89]:

$$P = \frac{EA}{2}(S^2 - S_0^2) - E[1 + \frac{1}{3}(\frac{Y^2 - W^2}{Y^2 + W^2})^2]log(1-e) \tag{4.4}$$

in which E is Young's modulus of the elastomer, $2Y$ and $2W$ are the length and width of the rectangular layer, A is a constant given by [Tak08, Lee89]:

$$A = \frac{4}{3} + \frac{W}{Y}(2 - \frac{11W}{10Y}) \tag{4.5}$$

and S is the shape factor after deformation, which is given by[Tak08, Lee89]:

$$S = \frac{YW}{2d(Y+W)} = \frac{S_0}{1-e} \tag{4.6}$$

in which $2d$ is the layer thickness after compression and S_0 is the initial shape factor with initial thickness $2d_0$ before compression. With equations 4.4-4.6, the Δd of the polyimide layer can be calculated and the corresponding ΔC can be calculated with equation 4.3.

Equations 4.1-4.6 assume the sensor shape is rectangular, and ignore several factors such as the fringe field capacitance, and hydrostatic pressure on the sidewall of the sensor. These factors could affect the capacitance change under applied pressure. To more accurately calculate the capacitance change of the sensor, a preliminary FEA for the sensor was performed in COMSOL™ Multiphysics with consideration of all these factors. In the simulation setup, the sensor structure and the corresponding material property were built and imported into the COMSOL™ Multiphysics software. Uniform pressure was applied to all the sensor surfaces to emulate the hydrostatic pressure. The capacitance between the electrodes was then calculated using the built-in calculator. The relationship between the applied pressure and the sensor capacitance change

was then obtained. Four different sensor geometries were simulated in order to understand the effect of sensor shape, including a square-shaped sensor (LC-SQ), a round-shaped sensor (LC-R), a T-shaped sensor (LC-T) that was fabricated on the ELM3.0 system and tested, and a sensor with an array of rectangular strips (LC-RS) (Fig. 4.3). The unique names for these sensor designs are summarized in Table 4.1 for reference. All of these geometries have an active area of 20 mm^2. The sensor LC-SQ with various side lengths from 10 μm to 5 mm were also simulated in order to understand the effect of the sensor area.

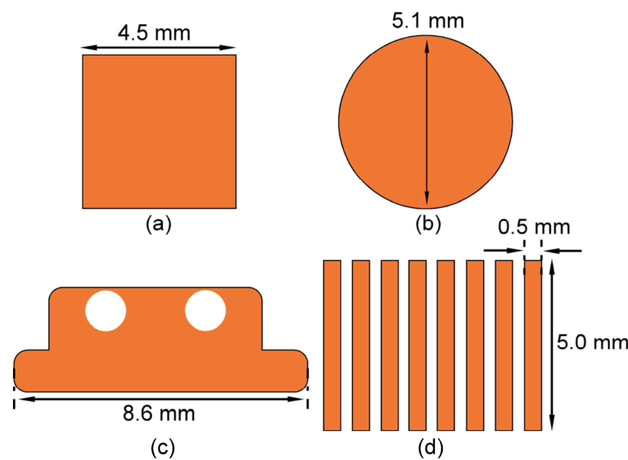

Figure 4.3: The four sensor geometries used for FEA analysis. (a) The square-shaped sensor (LC-SQ). (b) The round-shaped sensor (LC-R). (c) The T-shaped sensor fabricated on ELM3.0 and tested later (LC-T). (d) The rectangular strip array sensor (LC-RS). All of these geometries have an active area of 20 mm^2.

For the four sensor geometries, the simulated capacitance changes over 0-50 MPa were very close to each other, all between 160-170 fF. The ΔC versus applied pressure for the four sensor geometries are plotted in Fig. 4.4. According to the plot, the ΔC has a linear relationship with the applied pressure. The capacitance changes are smaller but comparable to the calculated results using equation 4.1-4.3 (246 fF). The sensitivities of the sensors are close to each other as well. As an example, the T-shaped sensor has a sensitivity of 3.22 fF/MPa. According to the

simulation results, the sensor geometry does not affect the sensitivity a lot when the sensor sizes are in the mm^2 range.

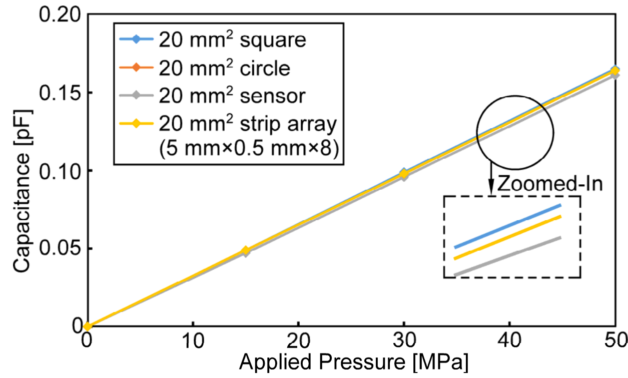

Figure 4.4: The simulated ΔC over applied pressure for various shapes of sensors with an area of 20 mm^2.

The sensor LC-SQ with different sizes are then simulated to understand the dependency of sensor sensitivity on the sensor area and thickness. For the sensor LC-SQ with different sizes, the simulated ΔC per unit area at 50 MPa versus sensor sizes is plotted in Fig. 4.5(a). Three thicknesses of polyimide dielectric are simulated, including 10 µm, 25 µm and 50 µm. According to the plot, this ΔC per unit area starts with a negative value when the sensor size is as small as the dielectric thickness. As an example, for sensor LC-SQ-10-25, the simulated capacitance change per unit square is -2.8 fF/mm^2. This value increases quickly with the sensor size and becomes positive, and then saturates and stabilizes as the size further increases. The sensor with thinner polyimide (i. e., LC-SQ-2000-10) has a higher ΔC per unit area than the sensor with same size but thicker polyimide (LC-SQ-2000-25) due to the larger unit area capacitance indicated by equation 4.1. The simulated capacitance change over the initial capacitance (under zero pressure) is plotted in Fig. 4.5(b). This fractional change in capacitance $\Delta C/C_0$ shows a similar trend as ΔC per unit area when the sensor size increases from small to large, except that the three curves saturate at a

same quantity. This is easily understood since the thickness quantity does not affect the fractional capacitance change when the capacitor size is large enough to be modeled by equation 4.1.

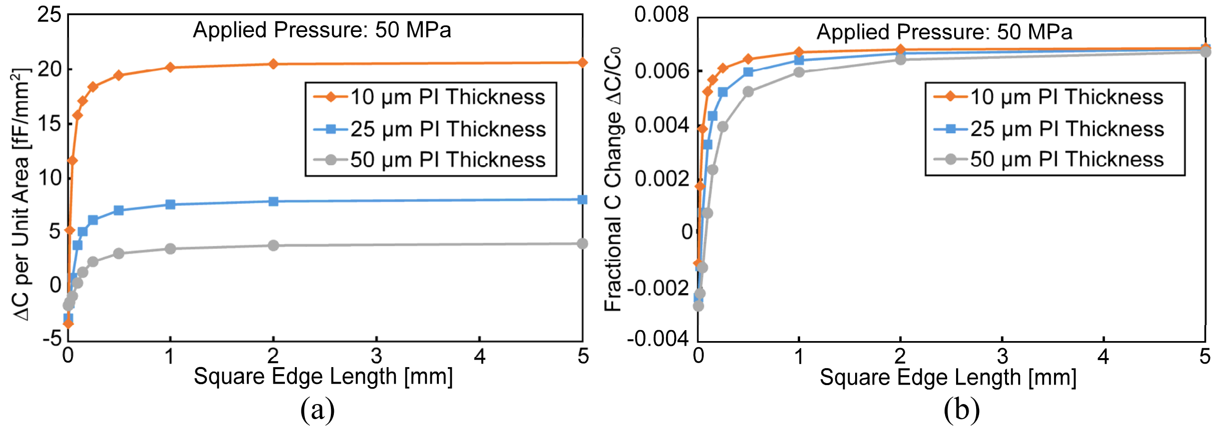

Figure 4.5: (a) The simulated ΔC per unit area (fF/mm^2) of the LC-SQ sensor for different areas and thicknesses. (b) The simulated ΔC over C_0 of the LC-SQ sensor for different areas and thicknesses.

To understand the relationship between the sensor size and the capacitance change per unit area, the deformation of the square-shaped sensor under 50 MPa pressure was further investigated. In Fig. 4.6(a), the deformation of the sensor LC-SQ with a thickness of 25 μm and edge length of 25 μm is plotted. In Fig. 4.6(b), the deformation of the sensor LC-SQ with a thickness of 25 μm and edge length of 1 mm is plotted. For the sensor with an edge length of 25 μm, the sidewall of the polyimide is deformed inward due to the hydrostatic pressure being applied to all surfaces. Although the sensor gap is reduced by the high pressure, the effective capacitance area is also reduced, and a negative ΔC is observed under high pressure. For the larger sensor with a 1 mm edge size, the inward deformation on the sensor sidewall still exists, but can be safely ignored due to the large sensor area. The sensor gap reduction has a more significant impact on the sensor capacitance change in this scenario. As a result, a sensor with a large area will have better pressure

sensitivity. With the sensor area further increasing, the geometry will be closer to the ideal two parallel metal plates and the sensitivity per unit square will tend to saturate at a certain area.

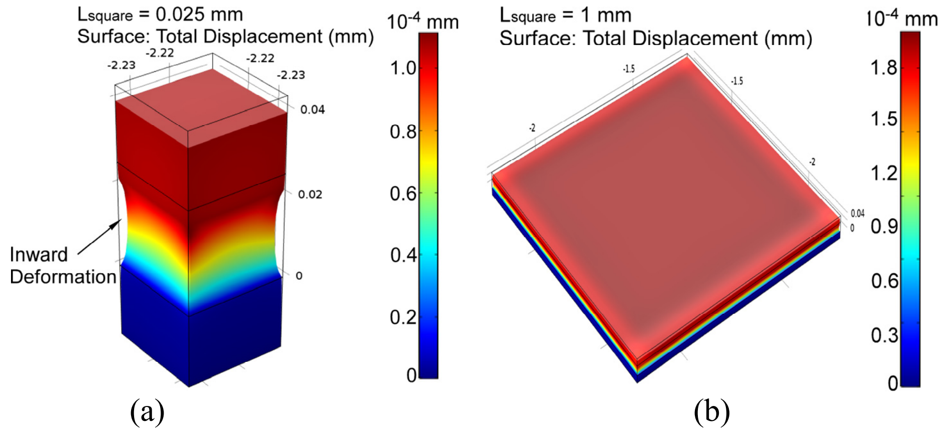

Figure 4.6: The deformation of the polyimide sensor with a 25 μm thickness, under the pressure of 50 MPa. (a) Sensor with 25 μm edge size. (b) Sensor with 1 mm edge size.

In summary, the sensitivity of the sensor structure has a high dependency on the sensor area, but a low dependency on the sensor area. Table 4.1 summarize the sensor geometries and the simulation results performed on each sensor. As a result, a larger sensor area is demanded for enhanced sensitivity, and the shape is accommodated to fit the PCB size.

Table 4.1: The summary of the LC sensor names and simulation results.

Sensor Geometry	**Unique Name**	**Sensor Area Used in Simulation (mm^2)**	**Polyimide Thickness Used in Simulation**	**Sensitivity (fF/MPa)**	**Note**
Square	LC-SQ	0.0001, 0.0006, 0.0025, 0.01, 0.0225, 0.0625, 0.25, 1,4,20,25	10, 25, 50 μm	3.30 for 20mm^2, 25 μm thickness device	Each sensor is named as LC-SQ-side length (in μm)-thickness (in μm)
Round	LC-R	20	25 μm	3.22	N/A
T-shape	LC-T	20	25 μm	3.22	The sensor later fabricated in ELM3.0 for testing
Array of rectangula r strips	LC-RS	20	25 μm	3.28	N/A

4.3. Device Fabrication

An LC polyimide pressure sensor was designed and fabricated with the ELM3.0 system to verify the device concept and was used for future optimization and analysis. To accommodate the ELM3.0 system area and achieve a reasonable capacitance change at downhole pressure, the LC sensor is fabricated on the fourth layer of the system since there is more free space on that layer. The sensor is placed beneath the slide switch (Fig. 3.21). This sensor has a T-shape and an estimated area of 20 mm^2. Two holes are presented in the middle of the sensor to accommodate the dimples of the slide switch. The top and bottom metal layers of the sensor are connected with the C8051F990 capacitance readout pins. The layout of the sensor is shown in Fig. 4.7(a).

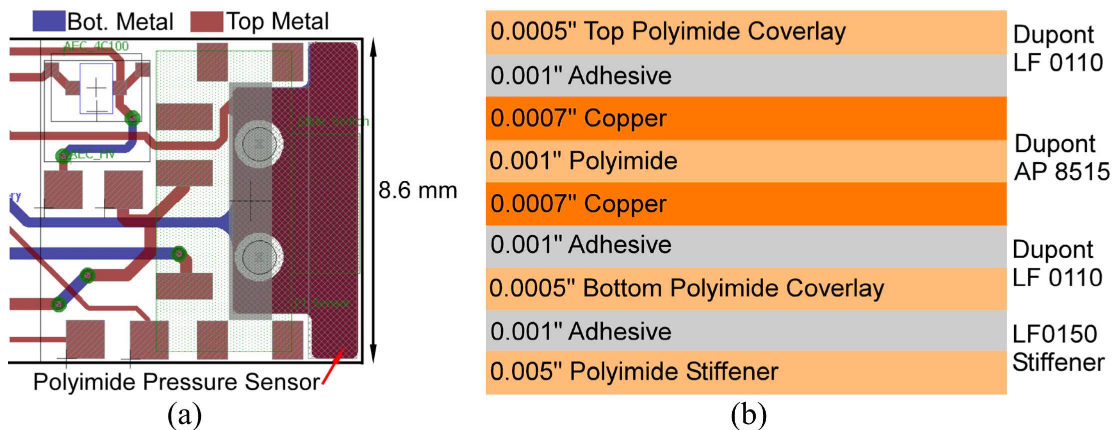

Figure 4.7: (a) The layout of the tested polyimide pressure sensor. The estimated area is 20 mm^2. (b) The stack configuration of the polyimide pressure sensor fabrication process.

The sensor fabrication process is the standard flexible PCB technology from All Flex, Northfield, MN. The stack configuration of the fabrication process is shown in Fig. 4.7(b). The dielectric polyimide layer has a thickness of 1 mil (25.4 µm), the top and bottom copper layers are 18 µm thick, and there is a 1 mil-thick polyimide coverlay layer over the metal layer. A 5 mil-thick stiffener layer is located beneath the polyimide sensor to make the PCB less flexible in regions where the electronic components are mounted. After PCB fabrication and assembly, the

system was packaged inside a silicone mold for anti-corrosion protection. Figure 4.8 shows the photo of the polyimide sensor on a bare flexible PCB board.

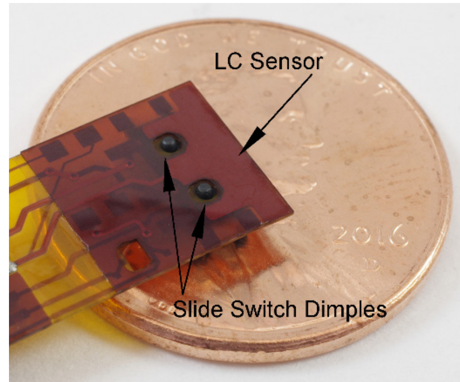

Figure 4.8: Photo of the polyimide sensor on an ELM3.0 flexible PCB. In this photo, the backside of the ELM3.0 PCB is facing up.

4.4. Experimental Results

The ELM3.0 system with the trial polyimide sensor was tested under high pressure (up to 50 MPa) at 25°C. The testing setup included a hydraulic pump connected with a Honeywell pressure transducer (0-10000 psi) for pressure monitoring. The hydraulic pump was connected to a pressure chamber which was filled with dielectric pump oil. The ELM3.0 system was folded once in order to fit inside the pressure chamber. During the test, the ELM system was triggered into the detection state with detection period of 1 minute, and then inserted into the pressure chamber. A staircase of pressure was manually applied, with each pressure step held for 10 minutes. The recorded capacitance and applied pressure during the tests were plotted in Fig. 4.9(a) and a zoomed-in view was plotted in Fig. 4.9(b). In the plot, the capacitance drifted up by over 1 pF over the testing period, and at each pressure transition point, an instant capacitance step of ~50 fF could be monitored. The instantaneous capacitance steps were evidently caused by the pressure change. The capacitance drift, in contrast, was caused by other physical factors such as electrical

or mechanical drift. This drift needs to be corrected in order to extract environmental pressure information.

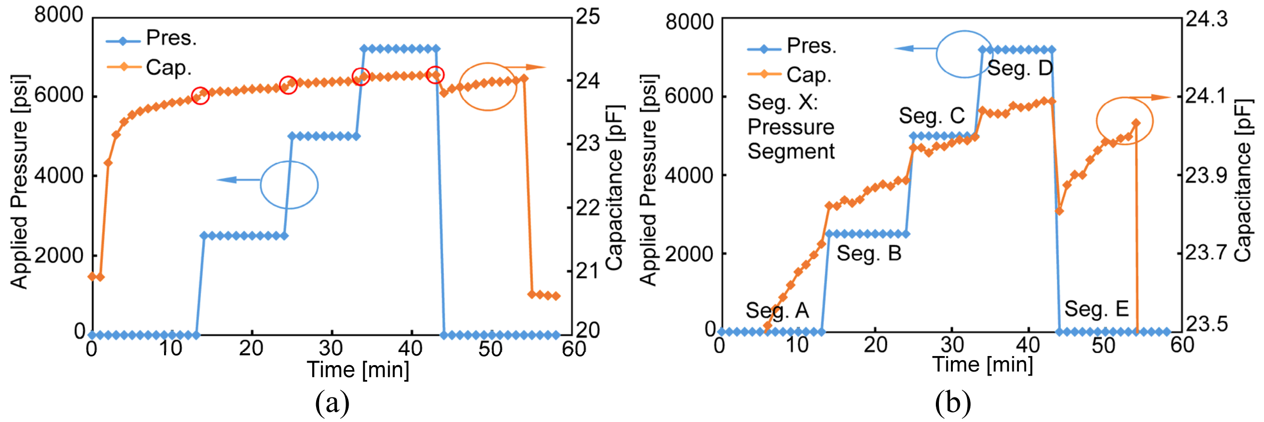

Figure 4.9: (a) The applied pressure and ELM3.0 recorded capacitance of the trial polyimide sensor during the high pressure test cycle. (b) The zoomed-in view of plot (a) at the pressure transition points. The pressure segments are illustrated in plot (b).

To correct the capacitance drift, a baseline correction algorithm is proposed for the capacitance-pressure curve. In this algorithm, the pressure within each segment of the applied pressure staircase is considered to be constant. The corresponding capacitance should also be constant if no drift exists. The time duration in which the pressure is constant is defined as a pressure segment, and is referred in later context. The capacitance drift in each pressure segment is assumed to follow a separate drift function $F_m(t)$ in which m indicates the pressure segment number, starting with m = 1 at atmospheric pressure, and t represents the time. Each $F_m(t)$ is obtained by fitting the observed data (t, C) in pressure segment m into a polynomial. The capacitance change between pressure segments m and $m+1$, ΔC_m, can be estimated as:

$$\Delta C_m = C(t_{m+1}) - F_m(t_{m+1}) \tag{4.5}$$

in which t_m is the last measurement time at pressure segment m, t_{m+1} is the first measurement time at pressure segment $m+1$, $F_m(t_{m+1})$ is the expected capacitance at the beginning of segment $m+1$

based on drift function in segment m, and $C(t_{m+1})$ is monitored capacitance at the beginning of segment $m+1$. In the next step, in each pressure segment m, the capacitance calculated by the drift function $F_m(t)$ in that segment is subtracted from the measured capacitance, and added with the sum of ΔC_m from all the previous pressure segment transitions. The baseline correction equation is:

$$C_{corrected}(t) = C(t) - F_k(t) + \sum_{m=1}^{k-1} \Delta C_m \tag{4.6}$$

assuming time t is in pressure segment k.

As an example, in the high pressure test of the ELM3.0 system, the capacitance increased by 68 fF at the first transition point (ΔC_1), and increased by 77 fF at the second transition point (ΔC_2). To correct the capacitance data within the pressure segment of 5000 psi, the drifted capacitance calculated from the drift function $F_3(t)$ is subtracted from the measured capacitance. The measured capacitance is then added with $\Delta C_1+\Delta C_2$ (145 fF). The resulting value represents the corrected capacitance after drift correction. Figure 4.10 shows the corrected capacitance of the high pressure test based on this baseline correction method. After baseline correction, three segments of applied pressure and capacitance are shown in the plot and the corrected ΔC over 0-50 MPa is 205 fF, which is close to the calculated result.

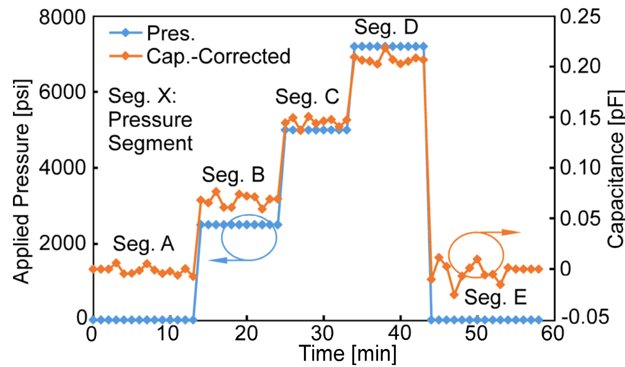

Figure 4.10: The applied pressure and the capacitance change of the trial polyimide sensor after baseline correction.

The previous analysis and experiments were conducted at room temperature. In addition to the nonideality of capacitance drift at room temperature, the LC sensor output also has a large temperature dependency due to the material property change. According to the datasheet, the dielectric constant of the sandwiched polyimide will drop from 3.4 at 25°C to 3.2 at 125°C, the tensile modulus will drop from 2.5 GPa at 25°C to 2.0 GPa at 200°C, and the thermal expansion coefficient of the polyimide film is 20 ppm/°C [Dup17]. These parameters will cause the LC sensor capacitance to change at high temperatures. In addition, the packaging material also has a temperature dependency and would affect the fringe capacitance. A high temperature test was performed on the ELM3.0 system to evaluate these contributing factors. In the experiment, two packaged ELM3.0 systems with RTI epoxy mold (system A) or silicone mold (system B) were triggered into the detection state, heated up in hot sand up to 125°C and cooled down. The temperature, capacitance change of the LC polyimide sensor (*ΔC-PI*), and capacitance change of the reference capacitor (*ΔC-Ref*) of the two systems under test are plotted in Fig. 4.11(a) and Fig. 4.11(b). The temperature dependency of the MCU capacitance readout module is removed by subtracting the *ΔC-Ref* from *ΔC-PI*, and the capacitance change after CDC temperature effect correction is recorded as *ΔC-Cor* and plotted in Fig. 4.11. From the plot, the *ΔC-Cor* changed by over 0.6 pF in system A, and over 0.3 pF in system B from 25°C to 125°C. This capacitance change is even higher than the capacitance change caused by only pressure over 0-50 MPa, which adds the difficulty of pressure data interpretation at high temperature. This needs to be addressed in future work for the sensor to be applied in the target environment.

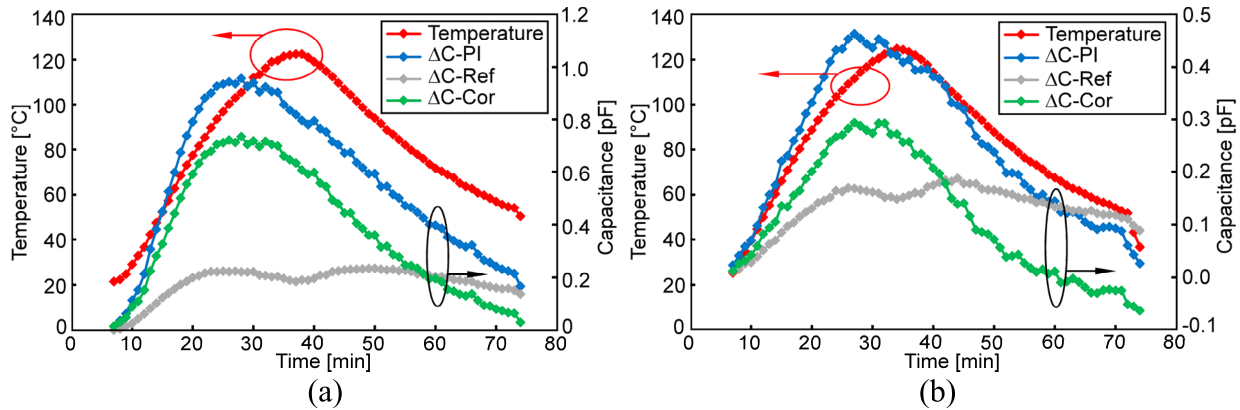

Figure 4.11: (a) The temperature and capacitance change during an ELM3.0 high temperature test, system A with RTI epoxy. (b) The temperature and capacitance change during an ELM3.0 high temperature test, system B with silicone mold.

4.5. Discussion and Summary

The concept of a LC polyimide sensor that can be directly fabricated on the ELM flexible PCB and potentially used for downhole pressure monitoring is proposed in this chapter. Theoretical analysis of polymer deformation under pressure and preliminary FEA results suggest that over 160 fF capacitance change can be obtained for such a sensor with 20 mm^2 area over 0-50 MPa. This capacitance change can be detected by the C8051F990 MCU. This sensor provides advantages over traditional MEMS pressure sensors in terms of low cost and elimination of hybrid integration processes. An LC sensor was fabricated along with the ELM3.0 system, with an effective area of 20 mm^2. A high pressure test of the trial sensor indicated that the sensor capacitance changed with pressure, but a high baseline capacitance drift was also observed, which needed to be corrected for accurate pressure interpretation. The high temperature test indicated that the sensor output had a high temperature dependency, which needed to be compensated for in future work for pressure interpretation at high temperature.

In addition to the capacitance change caused by high pressure, electrical drift (possibly) and temperature, the output capacitance of this LC sensor also will depend on several other

environmental parameters, such as humidity. For instance, according to the material datasheet, the dielectric constant of the polyimide would change from 3.1 to 3.8 over humidity of 0-100% [Dup17]. All these factors can contribute to sensor output capacitance change and make pressure interpretation more difficult. As an example, Fig. 4.12 shows the capacitance change of the LC sensor from one ELM3.0 system during a brine well test cycle described in Chapter 3. Although the hydrostatic pressure only went up to 1800 psi and the temperature went up to 70°C, the capacitance change during the test was more than 5 pF. This capacitance change is much higher than the possible pressure change caused by just pressure and temperature, and further investigation in the future is necessary to extract the pressure interpretation.

In summary, the concept of the LC sensor has been experimentally validated. However, polyimide properties can change under high temperature and humidity, and electrical drift and other environmental factors may add a large capacitance drift to the sensor output. Further investigation into alternative materials and proper techniques to isolate the sensor from these sources of interference will be necessary for the LC sensor to be used in the target applications.

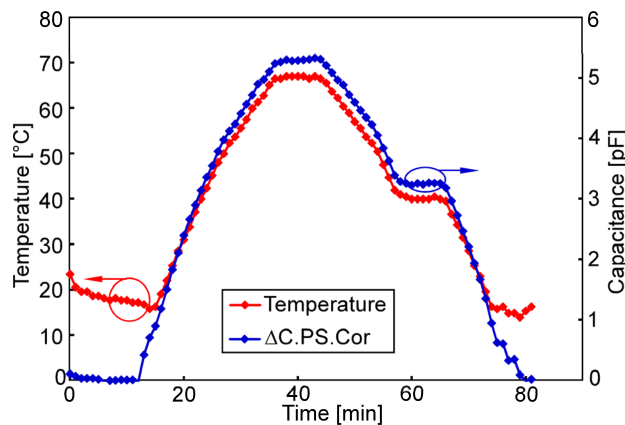

Figure 4.12: The temperature and polyimide sensor capacitance change of an ELM3.0 system during a brine well test cycle. The capacitance changed by 5 pF under 1800 psi pressure and 70°C temperature.

CHAPTER 5:

CONCLUSION AND FUTURE WORK

5.1. Conclusions

This dissertation advances the technology of the environmental logging microsystem (ELM) platform intended for downhole sensing applications that involve high temperature, high pressure, and corrosive chemical ambients. The microsystem developed in this work can perform temperature and pressure logging functions at ≥125°C and ≥50 MPa in brine, oil and drilling mud environments with operation lifetime that exceeds 12 hours. Package size has also met the target of < 1 cm^3.

Towards the first specific goal of the work as stated in Section 1.5, a microsystem platform that can achieve the temperature logging function at high temperature and high pressure in a corrosive environment was designed and fabricated (ELM1.0). The system was implemented with commercial electronics and a custom encasement for packaging. The system was assembled on a flexible PCB and packaged in a sapphire on steel package. The packaged system had a dimension of 8.9×8.9×6.85 mm^3. The system was successfully tested at 125°C, 7200 psi in corrosive solutions for more than 1 hour. The maximum characterized system lifetime was 6 hours under 125°C in hot sands. The highest temperature the system survived was 150°C with the battery connected.

Regarding the second specific goal, two new generations of the ELM (ELM2 and ELM3) were upgraded from the ELM1.0 system. ELM2.0 included everything in ELM1.0, plus pressure

sensing capability. A micromachined pressure sensor was integrated into the system for pressure measurement up to 50 MPa. The ELM2.0 systems were packaged in steel shell filled with transparent polymer for pressure transfer while not affecting the communication. The packaged systems had a dimension of 9.5×9.5×6.5 mm^3. The systems were successfully tested up to 125°C, 7200 psi for 3 hours, and at a reduced temperature of 100°C for 13 hours. The third generation of the ELM (ELM3.0) was upgraded from ELM2.0, with a slide switch for sleep state power saving and a low-cost polyimide pressure sensor for coarse pressure measurement. Both the ELM2.0 and ELM3.0 systems were successfully tested in a brine well with a depth of 1235 m.

Regarding the third specific goal, the preliminary study of a low-cost polyimide pressure sensor for potential application in downhole pressure monitoring was performed. This low-cost sensor can be directly fabricated on the ELM printed circuit board, with two large metal plates as the sensing electrodes, and the sandwiched polyimide as the dielectric. Preliminary FEA was performed on sensors with different geometries and sizes, and the results showed that the ΔC of a 20 mm^2 polyimide sensor over 0-50 MPa can achieve 165 fF. A trial polyimide sensor used for initial testing was designed and fabricated on the ELM3.0 system. The high pressure test of this trial device indicated that a capacitance change of 205 fF could be observed under 0-50 MPa hydrostatic pressure, while a large capacitance drift was monitored. The sensor output had a high dependency on temperature, which was expected. This work indicated the need for proper techniques for material selection, sensor calibration and interference isolation.

Towards the last specific goal, a high power MEMS switch for RF communication applications was designed and fabricated. The capacitive switch had a fixed-fixed actuation bridge structure. The bridge was made of oxide-nitride-oxide (ONO) and the dielectric material was atomic layer deposition (ALD) of Al_2O_3. The estimated pull-in voltage was 22 V, insertion loss

was 0.2 dB and isolation was 20 dB at 2 GHz. The switch was hermetically packaged with an ONO shell and sealed with ALD Al_2O_3. The device was fabricated and a large in-plane deformation of the bridge was observed, which greatly degraded the RF performance of the switch. The best device achieved an on state insertion loss of 4.6 dB, and an off state isolation of 16 dB at 2 GHz. Further fabrication process refinement is required to bring the experimental performances closer to expectation, and thus to apply the switch in ELM system.

5.2. Future Work

5.2.1. A Power Management System with a MEMS Switch for Leakage Current Reduction at High Temperatures

As described in Section 1.2, the CMOS transistors have high leakage current at high temperatures, particularly above 100°C. The leakage current at high temperatures mainly comes from the reverse-biased PN junction. Although various technologies have been invented to reduce this high leakage current, a finite leakage current always exists due to the physical structure of the CMOS transistor. For devices in deep-submicron, the majority of leakage current of an NMOS in the off state can be calculated by [Roy03]:

$$I = I_{PN} + I_{SUB} + I_G \tag{5.1}$$

in which I_{PN} is the reverse-biased PN junction leakage, I_{SUB} is the subthreshold leakage and I_G is the gate leakage. The reverse-biased PN junction leakage dominates at high temperature and it depends on the diffusion current density [Cla92]:

$$J_p = \frac{qD_p n_i^2 [exp(qV/kT) - 1]}{L_{pn} N_{db} \gamma_P} \tag{5.2}$$

in which q is the magnitude of the electronic charge, D_p is the hole diffusion coefficient, n_i is the intrinsic concentration, k is the Boltzmann constant, T is the junction temperature in Kelvin, L_{pn} is

the length of PN junction, N_{db} is the donor density in the N-type region and γ_p is correction factor. From the equation, the junction current density has an exponential dependence on temperature. Experiments have been performed on CMOS transistors to measure the leakage current at various temperatures [Sho89]. As shown in Fig. 5.1, transistors with different gate width to length ratios (*W/L*) experience similar trends in leakage current growth with increased temperature. When the temperature is increased from 25°C to 250°C, the drain leakage current of transistors increases from 10^{-10} A to 10^{-6} A with a *W/L* of 50 µm/10 µm.

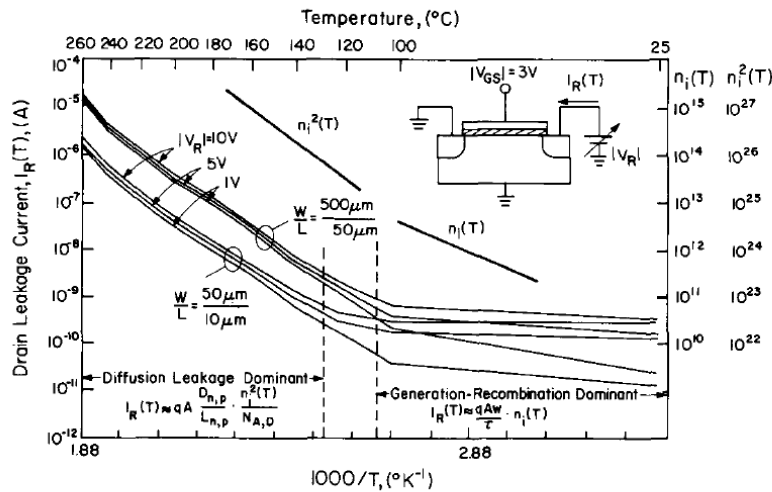

Figure 5.1: The measured leakage current for NMOS transistors with different gate dimensions and temperatures. The leakage current increased by several orders of magnitudes when temperature increased from 25°C to 250°C [Sho89].

A micromachined switch, similar to that in Appendix A, can provide almost zero leakage current as long as no dielectric breakdown occurs. The main reason is that compared to a semiconductor switch, there is no doping layer in the MEMS switch substrate; thus the carrier density remains at an extremely low level even with elevated temperature. To use a MEMS switch in an electronics system, a high actuation voltage is often required. The circuit block used to generate high DC voltage consumes power itself, and this power increases with the level of the

boosted voltage [Dic76, Pal04]. Therefore, the power consumed by the voltage boost block needs to be minimized. At Chung-Ang University, researchers developed an energy scavenging system with a MEMS switch as a gate driver (Fig. 5.2(a)) [Par12]. The energy scavenging system collects power from a solar cell. Under weak light conditions, their previous system using a semiconductor switch as the gate driver cannot harvest energy due to the leakage current caused by a Zener diode and transistors. The MEMS switch greatly reduces these leakage currents. With this device, their system can scavenge energy with an ambient light level as low as 5 lux. However, a switch with low turn on voltage may present a reliability challenge for downhole deployment with sensitivity to operating temperature, acceleration, and surface forces that causes the moving elements to adhere. Additionally, any electrical resistance offered by such a switch will dissipate energy from the battery, reducing the operating lifetime.

In future work, if an appropriate switch becomes available, a power management system can be implemented for reduction of high temperature leakage current (Fig. 5.2(b)). The first part of this research can be to characterize the leakage currents of commercial MOS switches and custom DC MEMS switches, at various operating temperatures. Since the fabrication process is similar, the RF MEMS switch described in Appendix A can be modified to a DC MEMS switch. This experiment can compare the leakage current of the DC MEMS switch with semiconductor switch. The second part is to implement a power management system with MEMS switches. By placing the DC MEMS switches between the power traces and selected individual circuit chips, those chips can be switched on/off as needed. The target current consumption of the new system is expected to be much smaller than that of ELM1.0, which consumes >12 μA at 125°C during the deep sleep state. Finally, the designed power management unit will be integrated into the ELM and tested.

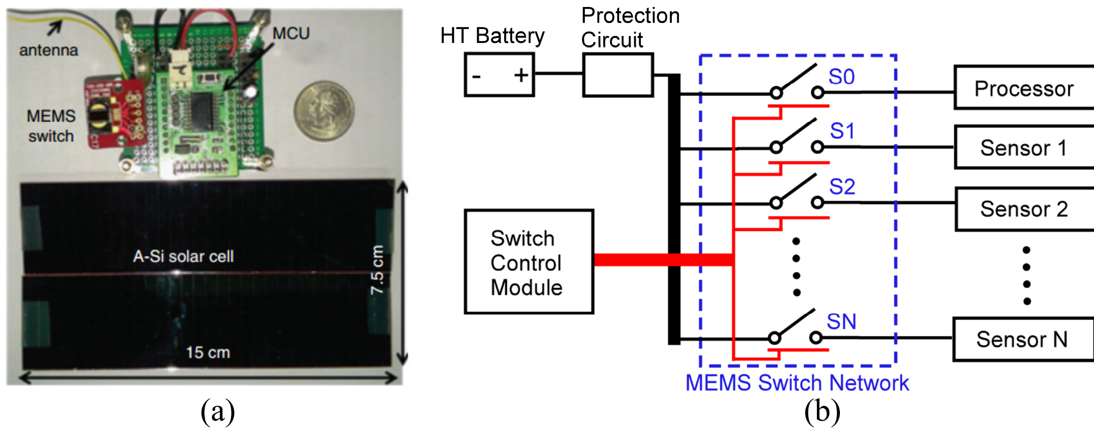

Figure 5.2: (a) An example shows the MEMS switch as a power management unit for energy scavenging of light [Par12]. (b) Proposed power management system circuit schematic.

5.2.2. A Miniaturized Antenna Network with MEMS RF Switches for Passive Communication

The communication method used in the ELM1.0 is bidirectional optical for ultimate miniaturization in the long term. Optical communication is not limited by antenna size as is RF communication. However, this optical communication method requires the MCU to be in the active state and consumes power. Usually, after a deployment cycle at high temperature, the battery is heavily drained and its performance may be degraded as well. The communication efficiency and reliability will be affected if the battery has a low remaining capacity and cannot be effectively charged. A passive communication method is of interest as it allows the system to report the measured data without active power consumption.

There are two challenges to implementing the passive communication method in the ELM system. Firstly, for miniaturized systems such as ELM, the antenna size can only be small, which requires a high communication frequency based on basic antenna theory [Bal05]. Secondly, to accommodate high frequency operation, the components needed to modulate the antenna should support high frequency operation, such as at 10 GHz. RF MEMS switches can serve as a solution to both issues. As explained in the appendix, the MEMS switch has the advantage of low power

consumption, high linearity and high isolation over a wide frequency band, thus making it applicable at high frequency. Meanwhile, the switch has its intrinsic property of turning on and off signal lines, and antenna impedance can be modulated. The MEMS switch has been used as a component for reconfigurable antenna in active communication applications (Fig. 5.3(a)) [Erd07]. By controlling the switches between the antenna patches, the operating frequency of this antenna can be selected between 7.5 GHz, 14 GHz and 23 GHz. Similar ideas can be used for passive communication at high frequencies.

A miniaturized antenna network implemented with MEMS RF switches for passive communication can be implemented in future work. The RF MEMS switches will be used to switch on/off an antenna network and alter the antenna impedance for passive communication. Due to the miniaturized antenna and high operational frequency, MEMS switches are used to enhance the system's performance. The designed antenna network can then be integrated into the ELM system (Fig. 5.3(b)). In the final passive communication system, in addition to the antenna and RF switch network, there is a matching network, an energy harvester module for system wireless power, a modulator and a demodulator for signal processing and a processor for system control. The processor can be the MCU shared with ELM or an individual processor for communication only. With the help of the MEMS switch network, the antenna system can support passive communication at a very high frequencies.

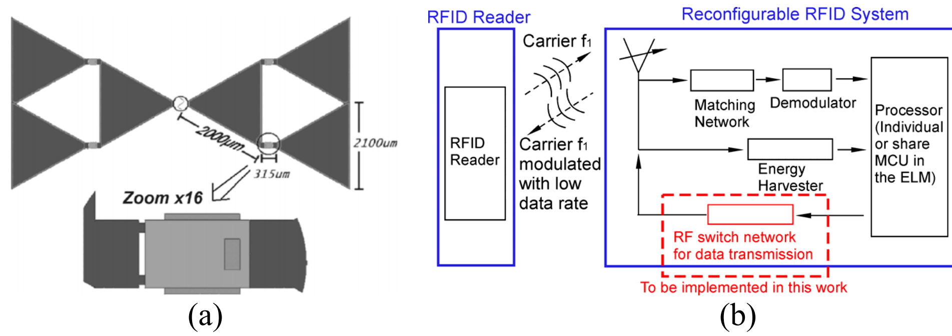

Figure 5.3: (a) An example of reconfigurable antenna implemented with RF MEMS switches [Erd07]. (b) The proposed architecture of the passive RFID system for wireless communication, with assistance from the RF MEMS switch network.

APPENDIX A

A MEMS HIGH POWER TX/RX DUPLEX SWITCH FOR RADIO TRANSCEIVER APPLICATION

This chapter describes the design, fabrication and testing results of a high power RF MEMS switch. The RF switch is an essential component in modern communication and can be used to establish antenna networks for microsystems. Due to a miniaturized antenna size, the required communication frequency of the ELM is high. As described in Chapter 5, the RF MEMS switches can be used to build the miniaturized antenna as an element for a passive communication module of the ELM system. The near-zero current consumption of the MEMS switch also enables it to be used as a switching element for the ELM power management module. One of the MEMS RF switches that we previously reported was electrostatically actuated and consisted of stainless steel cantilevers and Pt-Rh contact tips [Ozk12]. This design has a footprint of 8.4 mm^2 and an actuation voltage of ≈90 V, provides contact and restoring force on the order of mN, and remains functional at a maximum input power of 20 W. The power handling capability significantly exceeds the requirement of switches for cellphones and microsystem applications. The device was also too large for the target application.

In this appendix, a literature review of the state-of-the-art RF MEMS switch is provided first. The common failure mechanisms of DC and capacitive contact switches are discussed. The appendix then describes the design, fabrication and testing results of a surface micro-machined RF switch. The switch employs a series capacitive approach that eliminates the need for large contact

force during actuation, while allowing a small footprint, low actuation voltage, and fast switching speed. It is designed to be self-packaged in vacuum in a shell made from silicon oxide and nitride films on a sapphire substrate. The switch is designed with a footprint of 1.6×0.5 mm^2, actuation voltage of 22 V and actuation speed of 5.5 μs. Simulations indicate that the switch has an on state insertion loss of 0.2 dB at 2 GHz, and an off state isolation of 16.5 dB at 2 GHz, meeting the project needs. The switch was fabricated with a 7-masks surface micromachining process. Despite several fabrication trials, the stress of the deposited dielectric layers proved to be difficult to control and the suspended elements of the switch were bent upon release from the sacrificial layer. Because of issues related to stress control, the RF performance of the switch was greatly compromised, and the best device achieved an on state insertion loss of 4.6 dB, and an off state isolation of 16 dB at 2 GHz. Future opportunities will be pursued to refine the fabrication process, control the residual stresses, and bring the experimental performance closer to expectation.

A.1. Review of the Microelectromechanical Systems (MEMS) RF Switch

The RF switch is a critical component for high frequency switching applications such as switching networks, portable wireless systems, phased arrays, reconfigurable antennas and so on [Reb03, Jac06, Luc04, Boz00]. Conventional semiconductor switches have gained commercial success with excellent device performance and high volume annual production [Per14, Tri14]. With the development of MEMS technology, the concept of the MEMS RF switch was successfully demonstrated in early 1980. Compared with conventional semiconductor switches, MEMS switches have advantages such as low insertion loss, high isolation, and near zero power consumption for switching at frequency ranges of 0-120 GHz. Extensive research has been conducted towards new switching mechanisms, innovative switch structures and improved material. Commercially these micro-machined switches are rapidly gaining market shares.

Regardless of the actuation mechanisms, there are two types of MEMS switches in terms of switched signal type: the DC contact switch and the capacitive contact switch. The DC contact switch simply switches an electrical circuit by breaking or connecting one conductor to another. This type of switch conducts both DC and RF signals. During contact, a finite resistance exists between the contact points. For regular 50 Ω transmission lines, contact resistance of 2 Ω or smaller is often required. Thus the requirements for the contact material include low resistivity and low stiffness. The contact force is usually required to be >1 mN [Hol68, Sch98]. The capacitive RF switch uses metal-insulator-metal contact to achieve the switching function. The DC signal is blocked and the RF signal is transmitted via the contact cantilever. Compared with the DC contact MEMS switch, the capacitive MEMS switch does not require large contact force since the down-state capacitance depends only on the dielectric material and thickness. This property provides the capacitive switch with a longer lifetime than the DC contact switch. A large down-state capacitance is often required for conducting the RF signal, which makes the capacitive switch large in footprint.

Many research groups have worked on the DC contact RF switch. For a DC actuated RF switch, the electrostatic actuation is the dominant actuation mechanism [Ozk12, Pat12, Mih01, Cho09]. At the University of Michigan, researchers reported a high power electrostatically-actuated DC-RF switch which consists of stainless steel cantilevers and Pt-Rh contact tips [Ozk12]. This design had a footprint of 8.4 mm^2, provided contact and restoring force on the order of mN, and remained functional at a maximum input power of 20 W and survived >8000 hot switching cycles with 10W input power (Fig. A.1(a)). This device was fabricated directly on PCB for integration with other individual RF components. Another example is the DC contact switch from the University of San Diego (Fig. A.1(b)) [Pat12]. The cantilever was fabricated with electroplated

gold and the switch had a footprint of 0.25×0.25 mm^2 and a power handling capability of >10 W over 0-40 GHz. Measured results showed a reliability of >100 million cycles at 0.1 W under hot-switching conditions. These RF switches have the advantages of low on-state insertion loss, high off-state isolation and high power handling capability. However, as described earlier, the lifetime of DC contact switches is limited due to the direct metal-to-metal contact.

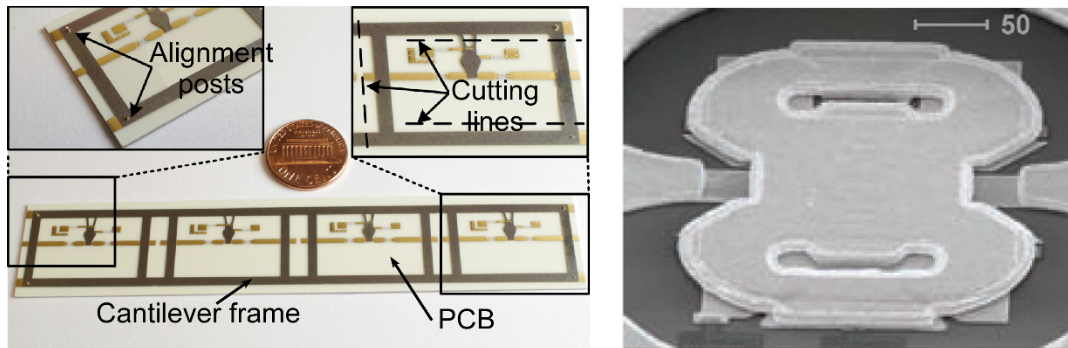

Figure A.1: (a) The photo of a high power DC-RF switch from the University of Michigan [Ozk12]. (b) The SEM image of a high power DC-RF switch from the University of California, San Diago [Pat12].

The DC contact MEMS switches suffer from reliability issues. The predominant failure mechanism of low power DC-contact switches is damage, piting and hardening of the metal contact area. For high power applications, the localized high contact temperature could cause the melting of the contact metal [Reb03]. The maximum reported lifetime of DC-contact MEMS switches is 10^9 cycles cold switching at 2 W input power. In the hot switching condition, the switching cycle number reaches 1 billion with -10 dBm power, and drops to 10^3 cycles with 20 dBm power [Rad15]. These numbers are still far below what are achieved by semiconductor switches. Small FET switches in microprocessors running at 3 GHz can accumulate 10^{17} cycles per year, while high voltage (>100 V) high power (>50 W) FETs for switched power supplies can

achieve more than 10^{12} cycles per year [Spe12]. These constraints significantly limit the use of DC contact switches in many scenarios such as mechanical logics.

Capacitive switches do not require metal-to-metal contact during actuation and can achieve longer lifetimes. They are usually large in footprint to meet the on-state insertion loss requirement. Figure A.2(a) shows a typical RF shunt switch from Raytheon developed from 1995-2000, which was recognized as a most mature capacitive MEMS switch at that time [Gol98]. This switch had a footprint of 300×250 μm^2, actuation voltage of 30-50 V, capacitance ratio of 80-120 and an isolation of -20 dB at 10 GHz. Figure A.2(b) shows an RF MEMS switch fabricated at the University of Michigan [Pac00]. With the help of a meandered spring structure, this device had a low actuation voltage of 6-20 V while it maintained other device properties such as miniaturized size and RF performance. In recent years, research on RF switches has been directed towards lower actuation voltage, faster speed, higher power handling capability, longer lifetime and CMOS process compatibility [Fou10, Al10, Per11, Mah10l, Bad12]. Figure A.2(c) shows a MEMS capacitive switch fabricated with a standard 0.35 µm CMOS process. The switch had an actuation voltage of 82 V, a capacitance ratio of 91:1 with a wrapped-plate structure, with an operating frequency up to 20 GHz [Fou10]. As seen from these examples, the performance of capacitive RF switches is limited by several factors. Due to the principle of capacitive coupling, a minimal down-state capacitance is usually required. This capacitance requirement requires the RF switch to be large enough. The actuation voltage cannot be too low since the switch needs certain recoil force when switching off.

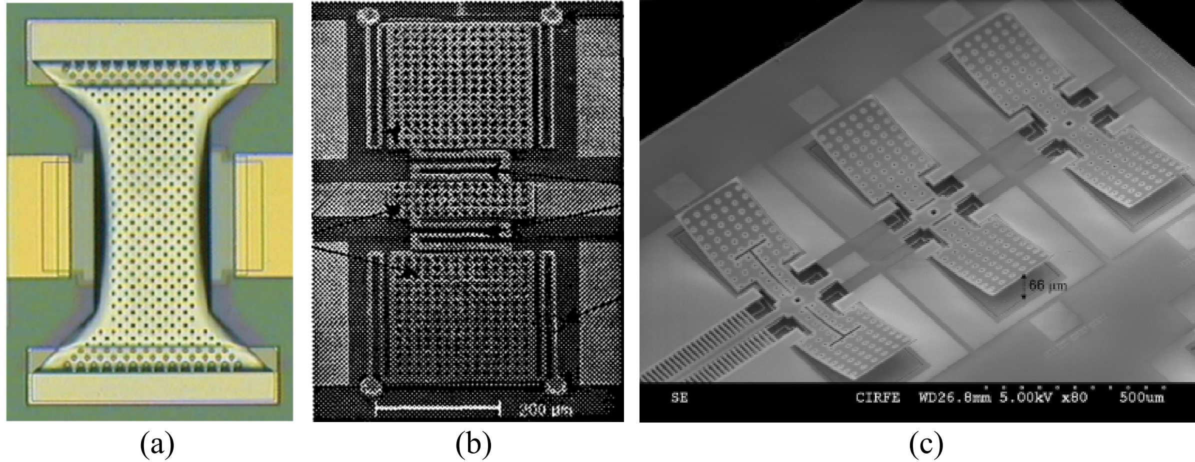

(a) (b) (c)

Figure A.2: (a) Photo of the Raytheon MEMS capacitive MEMS shunt switch [Gol98]. (b) Photo of the University of Michigan low voltage MEMS shunt switch [Pac00]. (c) SEM of the University of Waterloo capacitive MEMS switch fabricated with the standard CMOS fabrication process. A wrapped-plate structure is used to enhance capacitance ratio [Fou10].

The lifetime of the capacitive RF switch is mainly limited by dielectric charging. As explained before, in capacitive switches, there is always a dielectric layer between the actuation cantilevers for insulation protection. Due to the high electrostatic actuation voltage, the charges are injected and trapped in the dielectric layer (Fig. A.3(a)). Theoretical analysis of the accumulating charges was presented by researchers at the U.S. Air Force Research Laboratory [Rei02]. In the model, the shift of the switch C/V curve caused by a certain amount of trapped electrons was presented. It was known afterwards that these charged electrons were developed over time and gradually increased. Extensive efforts were made to address this dielectric charging issue. Many types of dielectrics were experimented with including SiO_2, Si_3N_4, AlN and Al_2O_3 [Bad12, Spe12]. As an example, researchers at the University of Colorado developed a capacitive RF switch with ALD Al_2O_3/ZnO alloy as the dielectric material for enhanced lifetime (Fig. A.3(b)) [Her07]. However, none of these solid-state dielectric materials can be completely free from dielectric charging. A dielectric-less capacitive switch was proposed and tested (Fig. A.3(c)) [Gri10]. With the dielectric layer removed from between the actuation electrode and ground and

an optimized geometric design, this switch achieved a lifetime of > 10 billion cycles, with 1 W input power under hot switching condition. In this design, the maximum capacitance ratio was only 5 due to the geometry of a large contact gap, which was intended to prevent the short circuit.

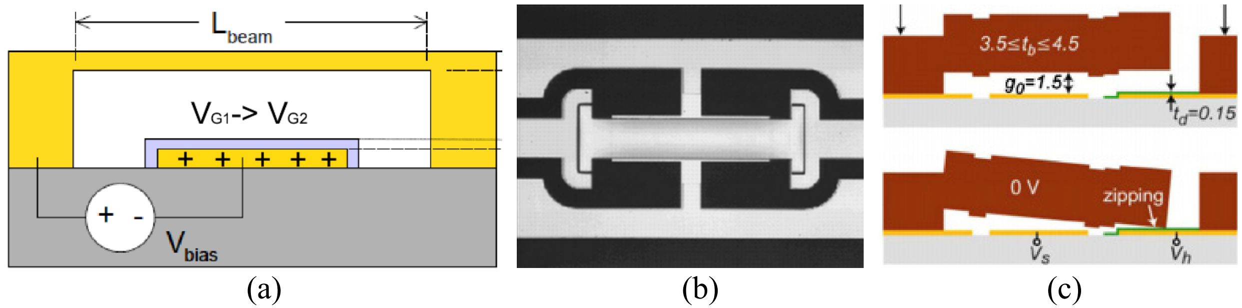

Figure A.3: (a) The principle of dielectric charging of the RF capacitive switch. (b) SEM of RF switch designed at the University of Colorado with ALD Al_2O_3/ZnO as the dielectric layer [Her07]. (c) The side view of the dielectric RF switch proposed by the University of San Diego [Gri10].

Packaging is the most costly step during MEMS production processes. As MEMS switches are very sensitive to humidity and contaminants, they must be packaged using hermetic or near-hermetic seals in a dry-air environment [Reb03]. Although the RF switch has been invented and improved on for years, appropriate packaging techniques are still under investigation. The available wafer scale packaging technologies include epoxy seals, metal-to-metal solder bonding, glass-to-glass anodic bonding and surface micromachining sealing. Among those technologies, surface micromachining sealing offers great benefits over the others in terms of single wafer processing, thus low cost. A surface micromachined vacuum packaging process was developed in University of Michigan [An14]. By using a 2-mask process and deposition of ONO as well as ALD Al_2O_3, a circular cavity structure was achieved with a near-vacuum condition (< 0.3 Torr). The hermeticity of the circular cavity was checked after 19 months and no deflection was observed (Fig. A.4). This packaging process can be modified to fit the needs of packaging the MEMS RF switches.

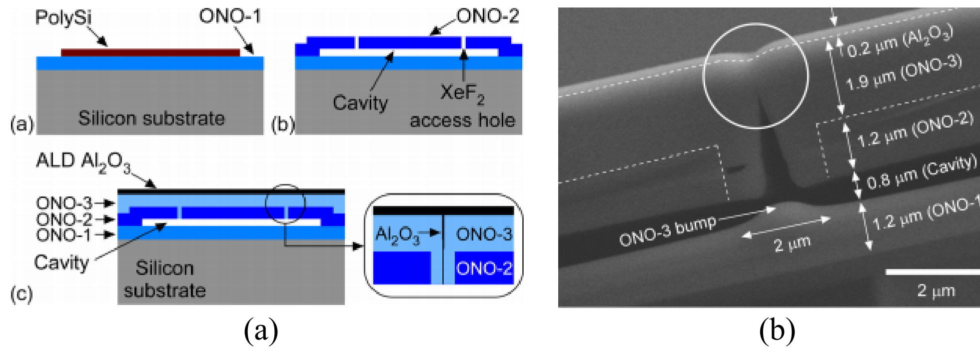

Figure A.4: (a) Fabrication process for the University of Michigan ALD packaging process. (b) The SEM photo of the cross section of the ALD package [An14].

The state-of-the-art RF switches as of 2015 and their performance parameters are included in Table A.1. Both the semiconductor switches and the MEMS switches are included. It can be clearly seen that the MEMS switches have wider bandwidth over 10 GHz, which is the mm wave frequency range. The frequency band is under exploration for the next generation of wireless technologies including the 5G network [Rap13]. The lifetime of the MEMS switch is still the main disadvantage compared with the semiconductor switch.

Table A.1: The performance parameters of state-of-the-art RF switches. Both semiconductor and MEMS switches are included.

Switch Component	Operational Frequency	Power / Lifetime	Linearity (IIP3)	Footprint	Packaging Technique
TriQuint GaAs Switch [Tri14]	0.1–6 GHz	33 dBm	56 dBm @ 1 GHz	2×2 mm^2	SMT Package
Peregrine UltraCMOS® Switch [Per14]	9 kHz – 18 GHz	30 dBm	58 dBm	4×4 mm^2	SMT Package
Radant MEMS Switch [Rad12]	DC-10 GHz	33 dBm, 10^9 cycles cold switching	65 dBm @ 900 MHz	1.85×1.9 mm^2	SMT Package
University of Michigan High Power Switch [Ozk12]	DC-10 GHz	43 dBm, 8414 cycles hot switching	N/A	4.2×2 mm^2 cantilever	LCP Package Filled Nitride
UCSD High Power DC Switch [Pat12]	DC-40 GHz	40 dBm, 10^8 cycles cold switching	69 dBm @ 1.96 GHz	0.25×0.25 mm^2	Unpackaged
UCSD RF Capacitive Switch [Gri10]	1-10 GHz	30 dBm, 10^{10} hot switching	N/A	0.14×0.16 mm^2	Unpackaged
Wrapped Cantilever Switch [Fou10]	10-20 GHz	25 dBm	N/A	0.21×0.275 mm^2 cantilever	Unpackaged
University of Colorado ALD Al_2O_3/ZnO Switch [Her07]	10-14 GHz	10^9 cycles, condition not mentioned	N/A	0.45×0.08 mm^2	Unpackaged
Raytheon MEMS Capacitive Switch [Gol98]	10-35 GHz	10^4-10^8 cycles	N/A	0.35×0.2 mm^2	Unpackaged
University of Michigan Capacitive Switch [Par00]	10-40 GHz	37 dBm N/A	N/A	0.7×0.25 mm^2	Unpackaged

A.2. Design and Modeling

A.2.1. Switch Design

The switch design is based on a fixed-fixed bridge structure (Fig. A. 5). The bridge is formed on an insulating (sapphire) substrate by an oxide-nitride-oxide (ONO) sandwiched film. The bridge structure consists of an actuation region on each end of the bridge and an RF contact region in the middle. The bridge is electrostatically actuated by a DC voltage applied between an

actuation electrode in each actuation region of the bridge and a corresponding DC ground electrode on the device substrate. Each actuation region has an area of 300×300 μm^2. The actuation gap is 1 μm. The RF contact region of the bridge includes a contact electrode, and is suspended over the RF signal lines. The area of the contact electrode is 200×120 μm^2. This large area is designed for the 2 GHz signal frequency. All electrode metal layers in this device are aluminum, and titanium is used as an adhesion layer. A layer of Al_2O_3 deposited by atomic layer deposition (ALD) to a thickness of 20 nm is used to insulate the electrodes and block DC current flow when the electrodes are pulled together. Sapphire is selected as the substrate material because of its low RF loss and high thermal conductivity. During the up state (in which the switch is off), the bridge is suspended over the coplanar waveguide (CPW) signal lines and the input RF signal is reflected at the input port. To transition to the down state (switch on) the signal, electrostatic force is generated in both actuation regions by an applied DC voltage. This drives the bridge down and greatly elevates the capacitance between the contact electrode and CPW lines, which enables RF signal transmission. The fixed-fixed bridge topology is better than a free cantilever topology since it provides better parallelism between the contact electrode and the RF lines during actuation.

The device is self-packaged in a 1.1 μm thick ONO shell, which is sealed by a 2.9 μm-thick Si_3N_4 film and a 100 nm-thick ALD Al_2O_3 film. This provides a modest vacuum environment for the bridge structure, allowing very low damping during actuation and release, thereby reducing the switching time. The hermeticity of packages sealed by ALD Al_2O_3 has been successfully demonstrated for over 19 months in past work [An14]. The package also helps reduce device contamination and leads to a longer lifetime.

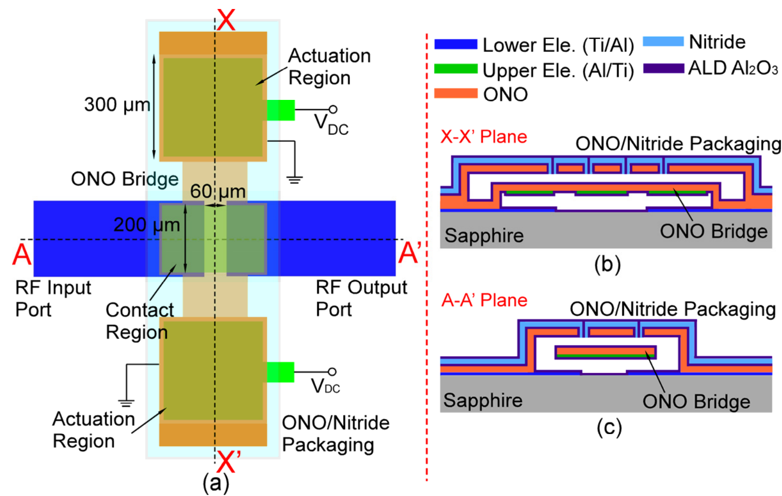

Figure A.5: (a) Top view of the proposed switch structure. (b) Cross sectional view along X-X'. (c) Cross sectional view along A-A'.

In certain design variations of the switch, a crab-leg shaped suspension is used to interconnect the actuation region and the contact region of the bridge. This structure is intended to help release the stresses on both regions so that the contact electrode remains flat after device fabrication. The spring constant of the bridge reduces with the crab-leg structures, and so does the actuation voltage. This reduction reduces the recoil force and results in a slower switch.

There are six design variations in total, named from R-SP1 to R-SP6. The R-SP1, R-SP2 and R-SP3 designs have similar sizes and constitute the "regular design set". The R-SP4, R-SP5 and R-SP6 designs are similar in shape to R-SP1 to R-SP3, but with smaller footprints, and these constitute the "small design set". In these design sets, R-SP1 and R-SP4 do not have the crab-leg suspension, R-SP2 and R-SP5 have thin stress release arms, and R-SP3 and R-SP6 have wide stress release arms (Fig. A.6). As a result, R-SP1 and R-SP4 have greater stiffness than other designs. Table A.2 summarizes the geometry parameters for each design variation. Table A.3 summarizes the estimated performance parameters of the six designs, which will be discussed in a later section.

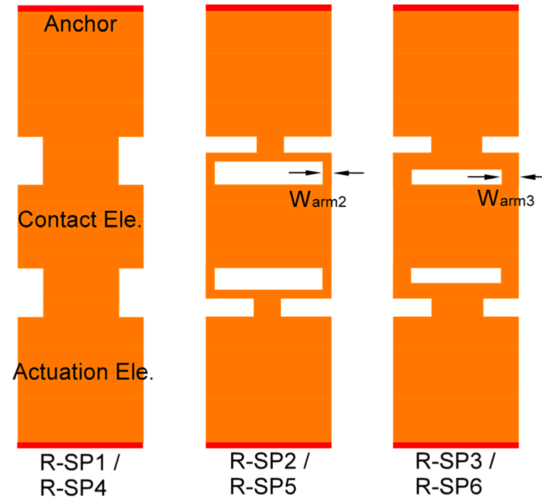

Figure A.6: The bridge design for switches R-SP1 to R-SP3. The designs R-SP4 to R-SP6 are the same designs as R-SP1 to R-SP3 but with 0.5x dimensions. The designs R-SP2, R-SP3, R-SP5 and R-SP6 contain crab-leg shaped structures for in-plane stress release.

Table A.2: Geometry parameters for each design variation of the RF switch.

Parameter	**Value (Regular Design Set)**	**Value (Small Design Set)**
Design Variable		
Actuation Electrode Length L_a	300 μm	150 μm
Actuation Electrode Width W_a	300 μm	150 μm
Contact Electrode Length L_c	300 μm	250 μm
Contact Electrode Width W_c	200 μm	100 μm
Transmission Line Space W_s	50 μm	50 μm
Crab-leg Arm Width W_{arm} (R-SP2, R-SP3, R-SP5, R-SP6)	R-SP2: 20 μm R-SP3: 40 μm	R-SP5: 10 μm R-SP6: 20 μm
CPW Line Width C_w	100 μm	
CPW Line Space to Ground C_s	50 μm	
Process Variable		
Actuation Gap g_a	1 μm	
Package Gap g_c	1 μm	
ONO1 Thickness t_{ONO-1}	0.15/1.4/0.15 μm	
ONO2 Thickness t_{ONO-2}	3.9 μm	
ALD Dielectric Thickness t_{ALD1}	20 nm	
ALD Sealing Thickness t_{ALD1}	100 nm	

Table A.3: Summary of RF switch designs and their performances.

Design ID	$V_{pull-in}$	S_{21}, on	S_{21}, off	Description
R-SP1	22 V	-0.12 dB	-16.5 dB	Regular sized design.
R-SP2	4.1 V	-0.12 dB	-16.5 dB	Regular sized design with thin crab-leg stress release structure.
R-SP3	7.7 V	-0.12 dB	-16.5 dB	Regular sized design with thick crab-leg stress release structure.
R-SP4	49 V	-0.28 dB	-20.1 dB	0.5x design of design R-SP1. Extended cantilever.
R-SP5	13.7 V	-0.28 dB	-20.1 dB	0.5x design of design R-SP2, with extended contact cantilever.
R-SP6	17.4 V	-0.28 dB	-20.1 dB	0.5x design of design R-SP3, with extended contact cantilever.

A.2.2. Switch Mechanical Modeling

The switch is actuated by electrostatic force between the bottom electrodes and the ONO bridge. The pull-in voltage during the electrostatic actuation is given by [Reb03]:

$$V_p = \sqrt{\frac{8k}{27\varepsilon_0 A} g_0^3} \tag{A.1}$$

where k is the spring constant for the bridge, ε_0 is the dielectric constant, A is the actuation area and g_0 is the initial actuation gap. Applying an actuation voltage $V_a > V_P$ would cause the device to pull-in. The fixed-fixed topology has a stiffer spring constant than that of the free cantilever. The spring constant for a fixed-fixed bridge with uniformly distributed load is given by equation [Ame07]:

$$k = \frac{384EI}{l^3} \tag{A.2}$$

where E is the Young's modulus of the bridge material, I is the moment of inertia for the bridge cross-section and l is the bridge length. Compared with a cantilever fixed only on one end, the fixed-fixed bridge has a flatter contact region.

As described earlier, there is no need to generate large contact force for a capacitive RF switch. However, to ensure good capacitive contact between the bridge and the RF signal lines, it is still recommended that the actuation voltage V_a equal 1.5-2 V_p [Reb03]. The equation to estimate contact force for a free-fixed cantilever is given by [Cou04]:

$$F_c = \frac{\varepsilon_0 \times A_{sa} \times V_{act}^2 \times a^2}{4 \times L \times (D_{act} - D_{con})}(3L - a) \qquad (A.3)$$

where D_{act} is the actuation gap, D_{con} is the contact gap, L is the bridge length and a is the actuation length. From the equation, a larger actuation area, larger actuation voltage and smaller actuation gap contribute to larger contact force.

The pull-in voltage of the RF switch is simulated in COMSOL™ Multiphysics 4.4. In the electrostatic simulation, a DC voltage is applied between the actuation electrodes and the ground electrodes, and the voltage value that causes the maximum bridge displacement before the bridge collapses is recorded as the pull-in voltage $V_{pull\text{-}in}$. To assess the impact of the in-plane stress caused by thermal expansion coefficient mismatch between the substrate and bridge, a uniform tensile biaxial stress of 0-200 MPa is applied to the ONO structure. This results in a bridge structure with higher stiffness, thus higher $V_{pull\text{-}in}$. Figure A.7(a) shows the deformation of 0.8 μm of the switch design R-SP1 at the 22 V pull-in voltage right before collapse. Figure A.7(b) summarizes the actuation voltages of designs R-SP1 to R-SP6, with various biaxial stresses. In the fabrication process, +160 MPa is selected as the target tensile stress for the bridge layer for stress compensation purposes. However, the actual stress value varies from run to run because of equipment limitations. With this stress value, the switch has moderate pull-in voltages and adequate stiffness. The bridge stiffness can provide sufficient recoil force to restore the bridge position and shape after it is released.

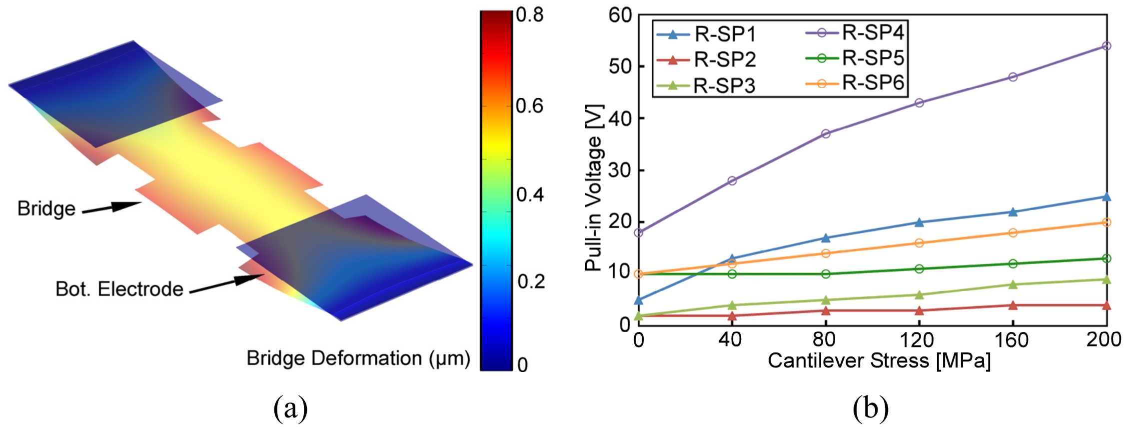

Figure A.7: (a) Deformation of bridge at 22.5 V voltage, right before pull-in. The design evaluated in the plot is R-SP1. (b) The bridge actuation voltage with different residual tensile stress, designs from R-SP1 to R-SP6 are included.

With a large tensile stress in the bridge structure (+160MPa in fabrication), the structure experiences high tensile force and mechanical failure at some weak points could occur. The von-mise stress distribution over the device volume is simulated in COMSOL™ Multiphysics 4.4. The simulation setup is shown in Fig. A.8(a). In the simulation setup, the bridge is fixed at two ends, and the ONO layer is assigned with a stress of -50/+170/-50 MPa. The averaged tensile stress in the structure is thus +160 MPa. With the assigned tensile stress, the maximum stress generated in design R-SP1 is 380 MPa, which is created at each corner of the bridge structure (Fig. A.8(b)). This stress is much smaller than the ultimate stress for silicon nitride (Si_3N_4) (>2 GPa), but the yield of the switch might be affected due to this stress. The maximum stresses for other designs are very similar, and have no dependence on device footprint or stress release structure. To reduce the stress generated at those weak points, one possible solution is to reduce the tensile stress in the ONO bridge layer. However, this reduction makes the bridge less stiff, and therefore a thicker bridge is required for certain recoil force.

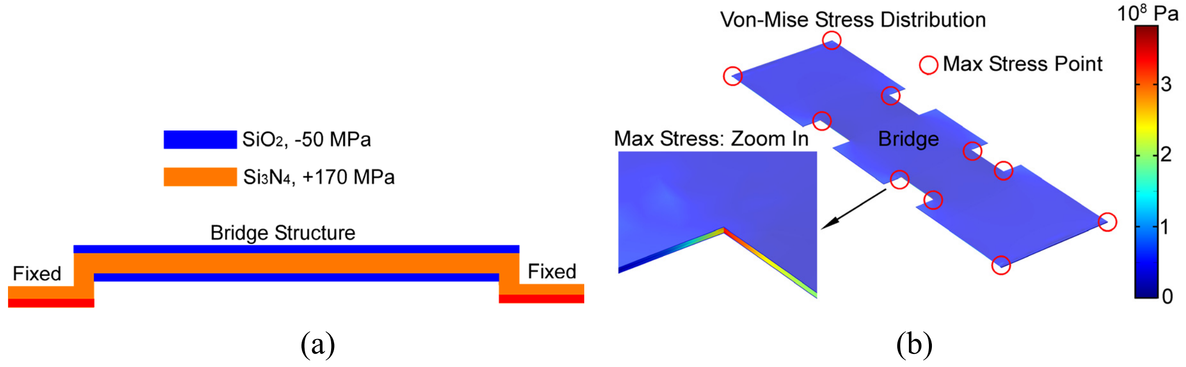

Figure A.8: (a) The setup for the stress analysis. (b) The simulation results for the stress analysis. The maximum stresses are generated at each corner of the bridge structure. The maximum stress generated with the pre-defined stress condition is 380 MPa.

The switching speed is obtained by analyzing the 1-D nonlinear dynamic model of the bridge structure. For inertial limited systems (beam with small damping coefficient and Q>2), switching speed is governed by equation [Reb03]:

$$t_s = 3.67 \frac{V_P}{V_s \omega_0} \tag{A.4}$$

where t_s is the switching time, V_p is the pull-in voltage, V_s is the actuation voltage and ω_0 is the bridge resonant frequency. Since the switch is vacuum packaged with ALD Al_2O_3 sealing, it can be treated as a low damping system. The resonant frequency of the structure can be obtained by:

$$\omega_0 = \sqrt{\frac{k}{m}} \tag{A.5}$$

where k is the spring constant and m is the mass of the bridge. The m equals 9.6×10^{-10} kg for regular-sized switches and 2.4×10^{-10} kg for smaller switches. According to equation (A.4) and (A.5), to achieve a faster switch, a switch structure with greater stiffness and lower mass is preferred. Table A.4 shows the calculated switching time, assuming $V_s = 2V_p$ and $\sigma_{biaxial} = +160$ MPa. Note that for switch designs with lower actuation voltages, such as R-SP2, the switching speed could be augmented with a larger applied actuation voltage.

Table A.4: The actuation speed of RF switches at $V_s = 2V_p$.

Design \ Parameter	Resonant Frequency ω_0 (rad/s)	Calculated Switching Speed t_c (μs)
R-SP1	417×10^3	4 μs
R-SP2	93×10^3	20 μs
R-SP3	126×10^3	14.6 μs
R-SP4	913×10^3	2 μs
R-SP5	270×10^3	6.8 μs

There is a concern that the switch bridge could bend upward or downward due to residual stress. Because the bridge occupies a large footprint and the bridge is thin, the in-plane residual stress could have spatial variation and cause the bridge to bend. Bending upward causes the bridge to touch the ONO packaging shell, and a stiction problem could occur. Bending downward causes the bridge to touch the substrate, and the switch stays in the down state and fails. To evaluate this situation, pre-defined stress conditions are assigned to the bridge. The bending of the bridge under the pre-defined stress conditions is simulated.

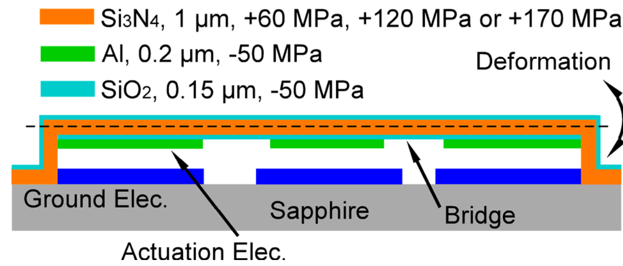

Figure A.9: The simulation setup for analyzing the out-of-plane bending of the RF switch.

The simulation setup is shown in Fig. A.9. In the setup, the stresses in each layer are assumed to be constant and any in-plane stress gradient is ignored. The bridge structure starts with the Al metal layer on the bottom surface, with a thickness of 0.2 µm and a stress of -50 MPa. Then the sandwiched bridge structural layers of $SiO_2/Si_3N_4/SiO_2$ follow, with thicknesses of

0.15/0.8/0.15 µm. The stress for the SiO_2 layer is set as -50 MPa constant. The stress of the nitride layer is set as one of three values: +60 MPa, +120 MPa and +170 MPa. The bending of the bridge layer at each stress value is estimated. This simulation allows us to observe the bridge bending with process variation. Theoretically, there exists an optimized stress for minimal bridge bending. The actual situation is more complicated due to process variation and an in-plane stress gradient.

Table A.5 summarizes the simulated bending distances of different designs under different stresses. According to the table, higher in-plane stress results in a larger bending distance. Comparing R-SP1 and R-SP2, the bending distance of R-SP1 is insensitive to the in-plane stress. The estimated bridge deformation is only 0.35 µm with +170 MPa biaxial stress (Fig. A.10(a)). The design R-SP2 with stress release arms is more sensitive to stress variations because of the reduced bridge stiffness. With the nitride stress varying from +60 MPa to +170 MPa, the deformation of the bridge varies from 5.87 µm to 10.2 µm (Fig. A.10(b)). This bending distance is large and could cause device failure.

Table A.5: Summary of out-of-plane bending distances at various Si_3N_4 stress conditions.

Si_3N_4 Stress / Design	+60 MPa	+120 MPa	+170 MPa
R-SP1	0.31 µm	0.33 µm	0.35 µm
R-SP2	5.9 µm	8.2 µm	10.2 µm
R-SP4	0.23 µm	0.24 µm	0.26 µm
R-SP1 with double bridge thickness	0.17 µm	0.17 µm	0.17 µm

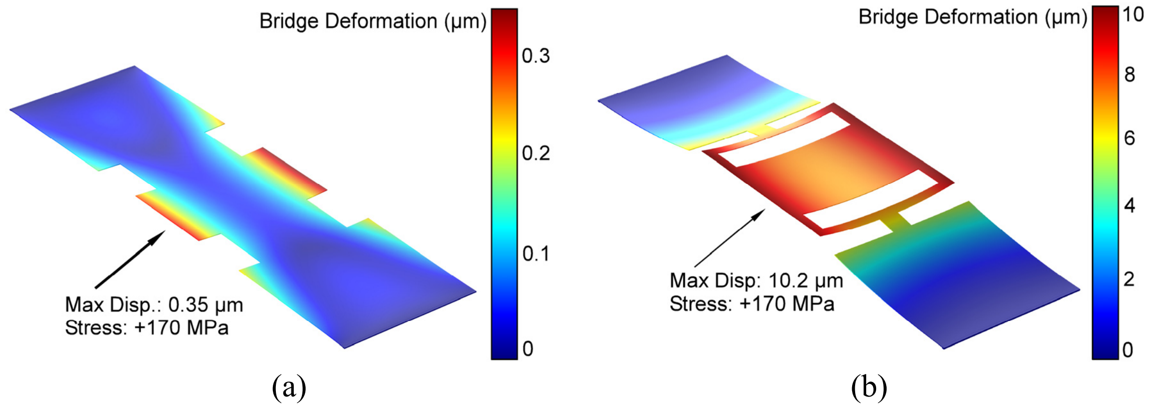

Figure A.10: (a) Deformation with +170 MPa stress in Si_3N_4 for design R-SP1. (b) Deformation with +170 MPa stress in Si_3N_4 for design R-SP2.

Increasing the ONO bridge thickness makes the bridge stiffer, thus preventing the out-of-plane bending. With the thickness of the Si_3N_4 layer doubled, the spring constant of the bridge increases by 8 times, and the deformation caused by in-plane stress stays at 0.17 µm with all three stress conditions. The drawbacks of a thicker bridge include a higher pull-in voltage and a more complicated fabrication process. The added thickness of the bridge requires the second sacrificial layer to be thicker as well. As described later in Section A.2, the sacrificial material is α-Si and deposition of very thick α-Si could cause the wafer to crack.

The dielectric Al_2O_3 layer between the bridge and the actuation electrode should sustain the high DC electric field in the down state and prevent the possible dielectric breakdown. For thin film Al_2O_3, the ultimate electric field before dielectric breakdown is 10 MV/cm [Hay15]. To sustain 40 V actuation voltage, the required minimal Al_2O_3 thickness is 40 nm. Since the ALD Al_2O_3 is evenly deposited to cover all exposed surfaces, 20 nm ALD Al_2O_3 is needed for deposition. The thickness of ALD Al_2O_3 can be increased if dielectric breakdown is observed during testing.

A.2.3. Switch RF Modeling

The switch is designed with a CPW transmission line configuration for convenient implementation and testing. The input and output ports are designed to accommodate the 150 mm pitch of the testing probe as well as 50 Ω RF characteristic impedance on a sapphire substrate at 2 GHz. The line calculator tool in the Advanced Design System (ADS) is used to calculate the design dimensions. A signal line width of 100 µm and space of 50 µm are obtained from the calculator tool (Fig. A.11). These parameters are chosen for the switch input and output port geometry.

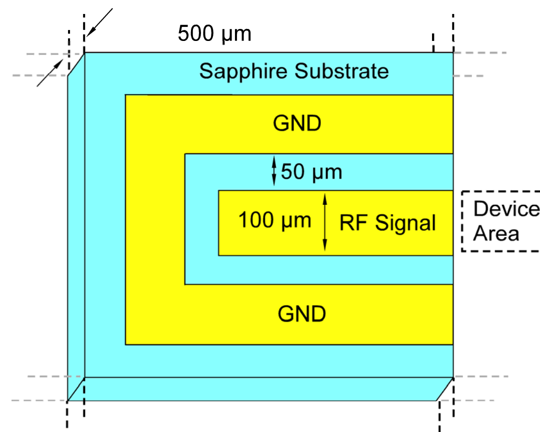

Figure A.11: The CPW line configuration used for the input and output ports of the RF switch.

Figure A.12 shows the physical structure comprising the switch from an electromagnetic perspective. Figure A.13(a) presents the lumped element model based on the traditional electromagnetic model for capacitive RF switches. Both input and output ports are modeled as a short section of transmission line. In the down state, the capacitive contact is represented as a series RLC network. The C_{down} depends on the contact material and thickness, which is the thickness of the ALD Al_2O_3. In the up state, the capacitance is modeled as C_{up} and this capacitance depends on the contact gap distance. The contact electrode is modeled as a short section of

transmission line, with the same characteristic impedance as the input port. The C_{gap} is the parasitic capacitance between the input and output signal lines. The C_{loss} is the parasitic capacitance between the signal line and the DC electrode, which is RF grounded. This capacitance is the major RF power loss path.

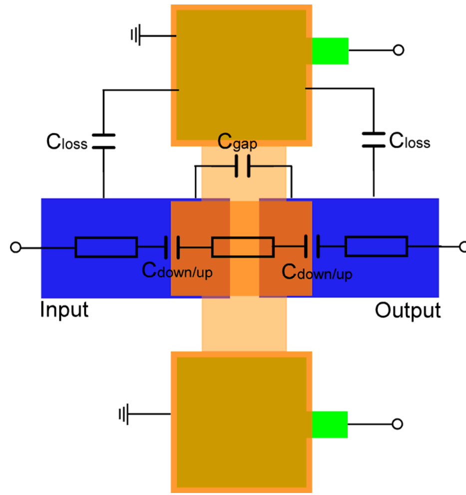

Figure A.12: Origins of the lumped-element components from the physical structure of the switch.

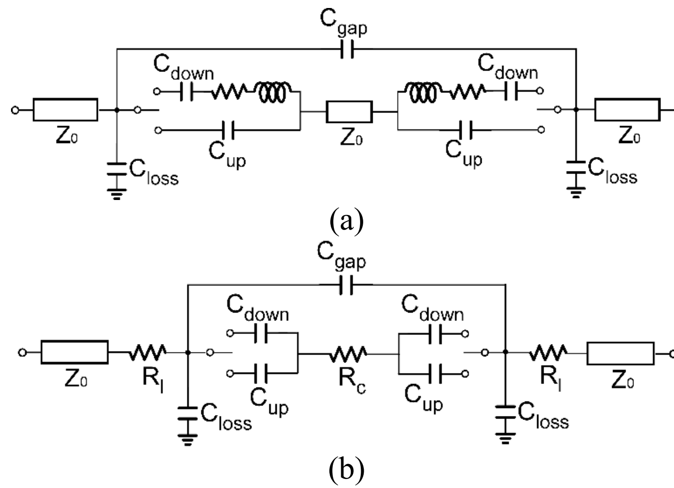

Figure A.13: (a) The general lumped-element model for the series capacitive RF switch. (b) The lumped-element model for the series RF switch in this work, considering the fabrication process and the metal thickness of each layer.

Figure A.13(b) shows the revised electrical model based on the device operation frequency and fabrication process in this work. Since this switch is designed for 2 GHz operation, the series inductance and resistance are ignored for their low impedance. Because the thickness of the metal input line is less than 1 µm, the series resistance of the input line cannot be ignored and is modeled as R_l. Due to the short distance of the contact electrode and its resistance, the contact electrode is modeled as a resistance R_c instead of a small piece of transmission line. The values for the lumped elements in the electromagnetic model are extracted (Table A.6).

Table A.6: The extracted parasitic capacitance in the lumped-element switch model.

Parameters	**Value (Regular Design)**	**Value (Small Design)**
C_{down}, 20 nm Al_2O_3	24.7 pF	7.6 pF
C_{down}, 40 nm Al_2O_3	12.3 pF	3.8 pF
C_{up}, 1 µm gap	212.4 fF	66 fF
C_{up}, 2 µm gap	106 fF	33 fF
Capacitance ratio (2 µm gap, 20 nm Al_2O_3)	233 fF	230 fF
C_{gap}	36.4 fF	17.6 fF
C_{loss}	40.0 fF	18.9 fF
R_l	0.159 Ω	0.265 Ω
R_c	0.141 Ω	0.141 Ω

From the table, with 2 µm gap and 20 nm ALD Al_2O_3, a capacitance ratio of 233 can be achieved. The switch isolation is limited by the large overlapping area between the bridge and the RF signal lines, which is the typical feature of capacitive switches. To improve the device isolation, these switches can be placed in a series and the equivalent on-state capacitance is reduced.

To model the RF performance of the switch designs, the switch models are imported into ANSYS HFSS to calculate the insertion loss and isolation of the switch from 1 GHz to 10 GHz. In the down state, ALD Al_2O_3 thicknesses of 20 nm and 40 nm are simulated. Thinner Al_2O_3 results in a lower (better) insertion loss due to the larger contact capacitance, but it also reduces

(worsens) the dielectric breakdown voltage (Fig. A.14(a)). In the up state, contact gaps of 1 µm and 2 µm are simulated. A larger contact gap provides higher (better) isolation (Fig. A.14(b)). All designs achieve insertion loss <0.4 dB and isolation >10 dB. The ALD thickness of 20 nm gives adequate insertion loss performance, and a 1 µm contact gap is adequate for isolation. As a result, 20 nm ALD and the 1 µm gap are selected as the fabrication parameters.

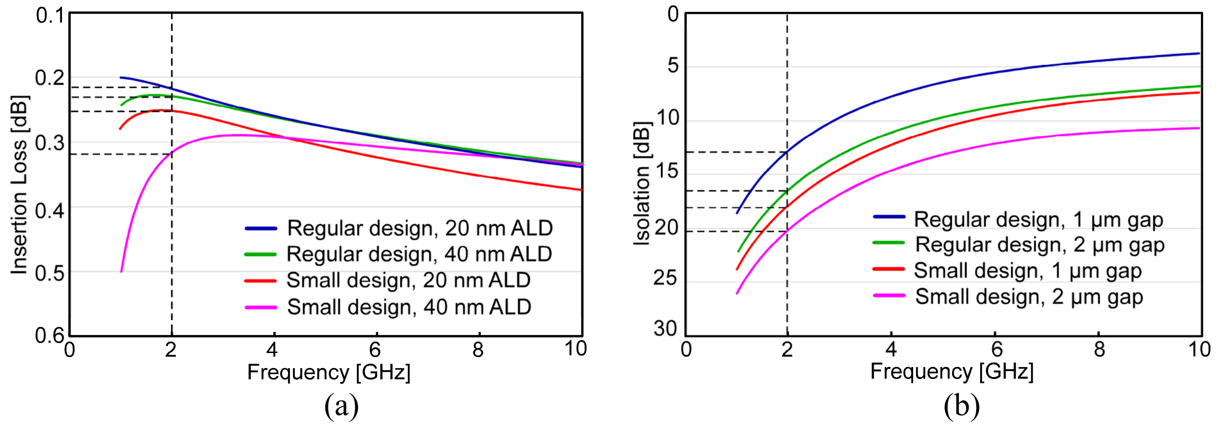

Figure A.14: (a) Down state insertion loss for regular and small design sets of the switch, with 20 nm and 40 nm Al_2O_3 thicknesses. (b) Up state isolation for both design sets, with 1 µm and 2 µm gap distances.

A.2.4. Switch Power Handling Analysis

The device is designed to handle continuous 1 W RF power without evident performance degradation. With high input power, the temperature at the contact point of the switch will increase, which affects the device's performance and reliability. The steady state temperature distribution of the device with 1 W input power is simulated in COMSOL™ Multiphysics 4.4. The simulation setup is shown in Fig. A.15(a). In the simulation setup, the input thermal power of the switch is estimated as the total RF power loss, and is assumed to be generated at the capacitive contact electrodes. For the proposed design, S21 ≈ -0.2 dB and the RF power loss is ≈0.05%. This contributes to 0.05 W input thermal power at the switch contact. The bottom surface of the

substrate is set at a constant temperature of 20°C. The heat generated from the switch contact electrodes is dissipated through the substrate. The ambient and the bottom of the substrate are assumed to be at 20°C. Both conductive and convective heat loss mechanisms are assumed to exist, and the thermal convection coefficient is assumed to be 5 W/m^2K. Only the switch element is simulated; the cap structure is ignored for simplicity. For comparison, both sapphire and glass substrates are simulated, with thermal conductivity of 35 W/mK and 1.1 W/mK, respectively. Figure A.15(b) and Fig. A.15(c) illustrate the simulated temperature distribution. Table A.7 includes the maximum temperatures for design R-SP1 and R-SP4 on sapphire and glass substrates. The maximum temperature of the device on sapphire substrate is 23°C (Fig. A.15(b)), compared with 87°C for the device on glass substrate (Fig. A.15(b)). This reaffirms the selection of sapphire as the device substrate.

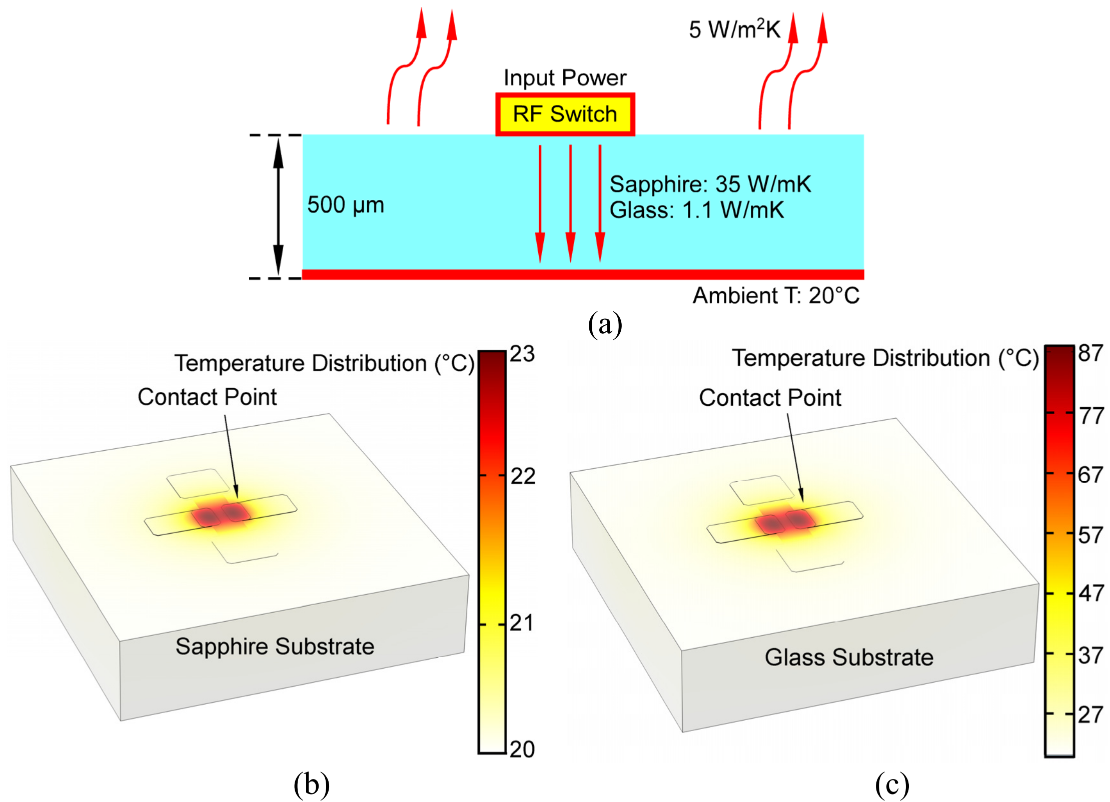

Figure A.15: (a) The simulation setup for steady state temperature; the heat conduction in the substrate is the main heat transfer path. The ambient temperature is set as 20°C. (b) The device temperature distribution with sapphire substrate at 1W input power, regular-sized design. (c) The device temperature distribution with glass substrate at 1 W input power, regular-sized design.

Table A.7: The simulated steady-state temperature at the switch contact point.

Condition \ Design ID		R-SP1 (S_{21} = -0.2 dB)	R-SP4 (S_{21} = -0.5 dB)
Sapphire substrate	1 W input power	22°C	33°C
	0.5 W input power	21°C	27°C
	0.2 W input power	20°C	23°C
Glass substrate	1 W input power	92°C	296°C
	0.5 W input power	57°C	158°C
	0.2 W input power	35°C	75°C

To improve the power handling capability of the switch, switches with larger footprints can be designed. The metal for contact and the metal signal lines on the substrate could be made thicker, so that the equivalent resistance of the transmission line would be reduced. This would

result in less on-state thermal power loss. Substrate materials with higher thermal conductivity and similar RF performances can be investigated as substitutes for sapphire.

A.3. Fabrication[1]

As noted previously, the RF switch is intended to be fabricated on a sapphire wafer (C plane, 650 μm thickness, front side polished) using a 7-mask lithography process (Fig. A.16). First, a Ti/Al layer (20/500 nm) is deposited by sputtering and patterned by lift-off on sapphire substrate to form the bottom electrodes, CPW transmission lines and exposed pads (Mask #1). Second, an α-Si layer (1.5 μm) is deposited by PECVD, which is then patterned by RIE plasma. The α-Si layer is used as the sacrificial layer between the substrate and the switch bridge structure (Mask #2). Third, an Al/Ti layer (thickness 250/20 nm) is deposited by sputtering and patterned by lift-off to form the upper electrodes (Mask #3). The exposed pads are thickened in this step by this metal layer for better contact. Fourth, a first ONO layer (150/1400/150 nm, total 1.7 μm, changed in later process modifications) is deposited by PECVD and patterned to construct the bridge structural layer (Mask #4). To match the temperature coefficient with the sapphire substrate, the ONO thicknesses are selected to provide a target tensile stress level of 160 MPa. Fifth, an α-Si layer (2 μm) is deposited by PECVD and then patterned by RIE plasma to form a sacrificial layer for the packaging shell (Mask #5). Sixth, a second ONO layer (150/800/150 nm, total 1.1 μm) is deposited by PECVD and patterned to construct the device hermeticity package (Mask #6). Etching access holes with a size of $0.8\times5\ \mu m^2$ are patterned on the second ONO layer. After this step, the wafer is diced to die scale.

---

[1] Switches were fabricated by Mr. Alexander Benken.

Seventh, after wafer dicing, the sacrificial silicon from steps (b) and (e) is etched by XeF_2 dry gas through the etching access holes, which releases the switch bridge structure and the hermitic package. Eighth, an Al_2O_3 layer (20 nm) is deposited by ALD to form the dielectric layer of the switch. This ALD layer covers the entire surface of the package (both external and internal). Ninth, a silicon nitride layer (2.9 μm) is deposited by PECVD to seal the etching access holes. This step is followed by an ALD layer (100 nm) to vacuum seal the package. Finally, the nitride and ONO layers are patterned by plasma etching and the contact pads are exposed for probing (Mask #7).

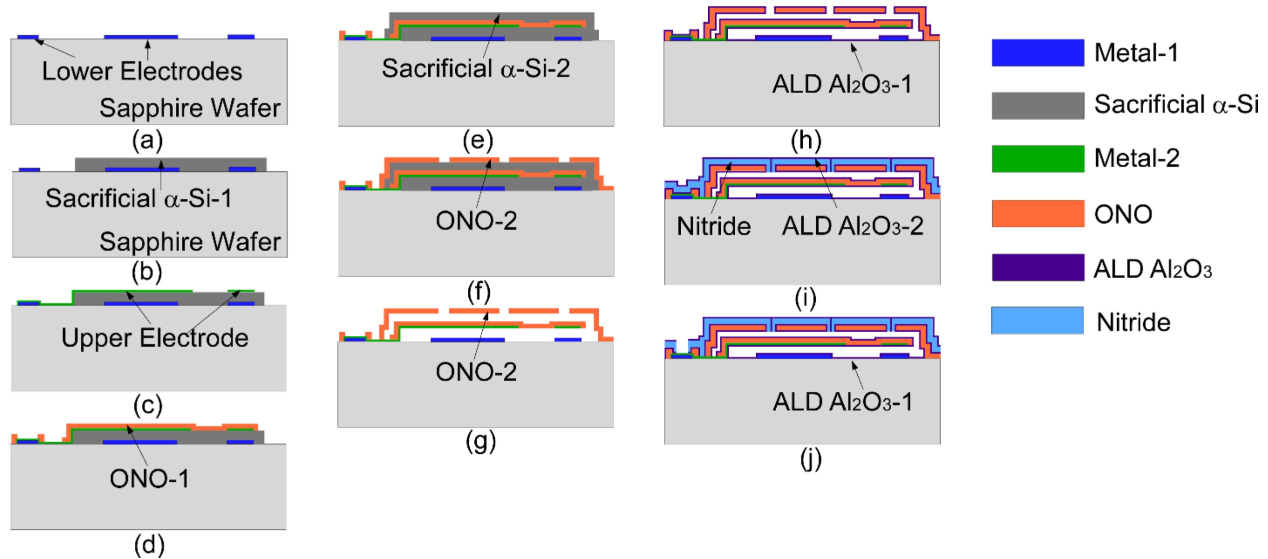

Figure A.16: The baseline fabrication process flow for the RF switch. (a) (Mask 1) Lower metal deposition and patterning. (b) (Mask 2) First sacrificial α-Si deposition and patterning. (c) (Mask 3) Upper metal deposition and patterning. (d) (Mask 4) ONO-1 structural layer deposition and patterning. (e) (Mask 5) Second sacrificial α-Si deposition and patterning. (f) (Mask 6) ONO-2 structural layer deposition and patterning. (g) XeF_2 etching of the sacrificial α-Si from steps b and e. (h) ALD Al_2O_3 deposition. (i) Nitride and ALD Al_2O_3 deposition, sealing the ONO-2 device package. (j) (Mask 7) ALD Al_2O_3, nitride and ONO-2 patterning.

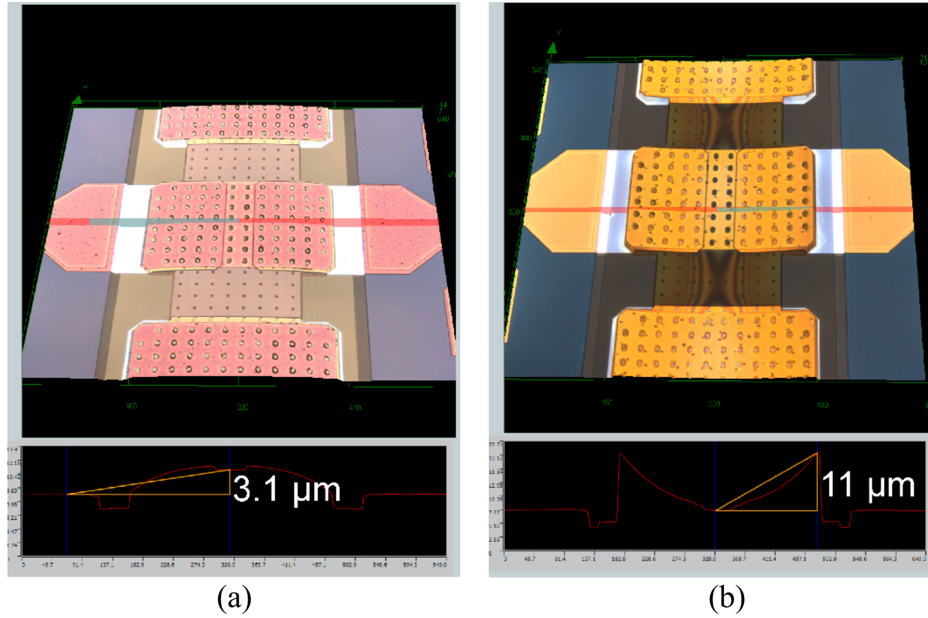

(a) (b)

Figure A.17: (a) 3D profile of the switch contact area, first batch, R-SP1. The switch is bent downwards for 3 µm. (b) 3D profile of the switch contact area, second batch, R-SP1. The switch is bent upwards for 10 µm.

As found during the process of development, the PECVD nitride has a biaxial tensile stress of +80 MPa and the PECVD oxide has a biaxial compressive stress of -120 MPa due to a thermal coefficient mismatch with the sapphire substrate. The upper electrode metal also has a tensile stress of ~100 MPa. As a result, these stresses not only cause increased bridge stiffness, but also bending. The bridge curvature affects the pull-in voltage and degrades the RF performance. Figure A.17 shows a 3D microscope scan that was performed after step (d), after the sacrificial α-Si was etched to release the bridge structure. The cross section of the RF switch without the ONO-2 capping layer is drawn in Fig. A.18. As specified by the fabrication process, the thickness of the lower electrode is 0.5 µm, the upper electrode is 0.25 µm, the sacrificial is 1.0µm and ONO-1 is 1.7 µm. Figure A.18(a) shows the expected cross-section profile at the A-A' plane with zero stress, where the contact cantilever is located on top of the two signal lines. Figure A.18(b) shows the expected cross section profile at the X-X' plane with zero stress, where the anchor is located. The

expected device profiles along A-A’ and X-X’ are illustrated in these two figures, and the diaphragm should remain flat after XeF2 release if no biaxial stress is presented.

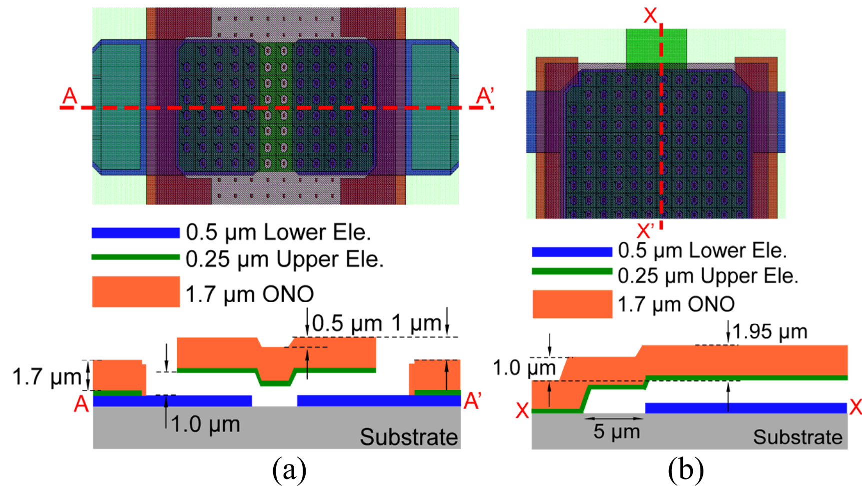

Figure A.18: (a) Cross-section view of the switch at A-A’ plane, where the contact cantilever is located. (b) Cross-section view of the switch at B-B’ plane, where the anchor is located.

Two batches of devices were fabricated with different ONO thickness combinations, and the profile of each device was measured. In the first batch, the ONO thickness was 0.15/1.4/0.15 µm, and the switch was bent downwards (Fig. A.17(a)). The bending of the diaphragm in the contact region was about 3 µm for R-SP1. The cause of this bending was suspected to be the extra tensile stress in the 0.25 µm thick upper electrode. In the second batch, to eliminate this downward bending, the oxide on the bottom was increased to 0.45 µm so that a higher compressive stress appeared on the lower side. The ONO thickness used in this batch was 0.45/1.1/0.15 µm. An extra 100 nm thickness of silicon nitride was also deposited on top of the lower electrode before the α-Si to prevent dielectric breakdown. This time, after sacrificial release, the switch was bent upwards and the bending in the contact region was close to 10 µm for R-SP1 (Fig. A.18(b)). This indicated that the bottom oxide of the ONO in this batch was too compressive. To eliminate this

upward bending, the bottom oxide can be reduced or additional compressive oxide can be added on top of the ONO. Top-down and angled view photos of the RF switches are shown in Fig. A.19.

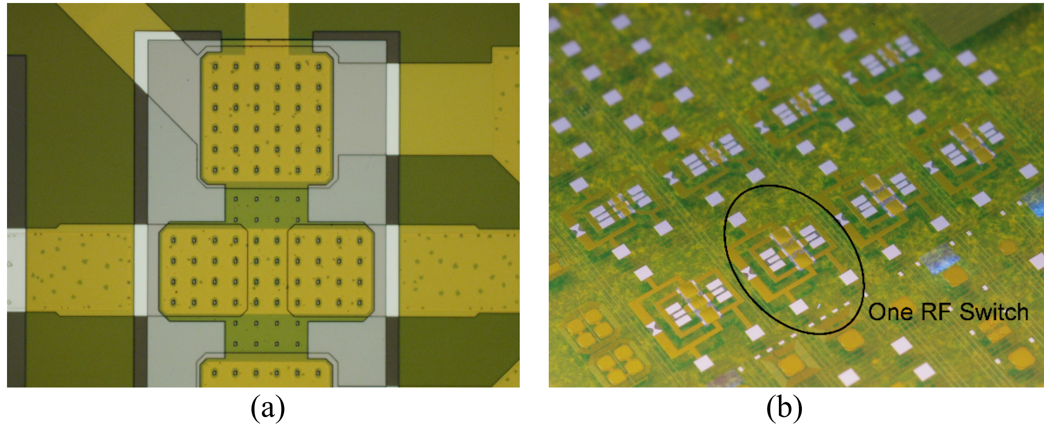

(a) (b)

Figure A.19: (a) Top-down view photo of device R-SP4. (b) The photo of the RF switch die with angled view.

A.4. Preliminary Testing Results

The RF performance of the switch is then characterized over 0.1-10 GHz. The measurement setup is shown in Fig. A.20. In the experiment setup, an HP 0-120V DC power supply is connected to the two DC actuation pads of the switch to provide actuation voltage V_{DC}. To prevent an high dielectric breakdown current and achieve a good RF isolation, two 1 MΩ resistors are connected in series with the DC actuation pads. The RF pads are connected with a 0.1-26.5 GHz network analyzer with 50 Ω RF probes. An isolator is used to protect the high reverse current from the DC voltage supply. The DC and RF grounds are shared in the experimental setup. In the test, the RF input signal is first swept from 0.1 to 10 GHz when V_{DC} is 0 V, and the S-parameter between the output and input port S_{21} is recorded as the off-state isolation. The DC voltage is then slowly increased until a sudden change occurs in the S-parameter curve. This sudden S_{21} change indicates that the contact capacitance has changed abruptly (thus the pull-in occurred), and this voltage is recorded as the pull-in voltage. The DC voltage is further

increased until the S_{21} curve stabilizes, and then this S_{21} curve is recorded as the on-state insertion loss.

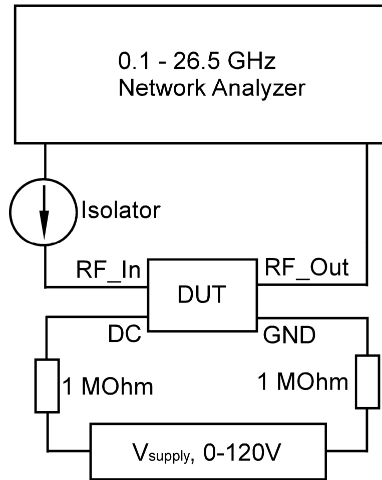

Figure A.20: The experimental setup for switch RF measurement. The two DC actuation pads are connected with the power supply, with 1 MΩ series resistors for dielectric breakdown protection and high isolation. The RF input and output pads are connected with the 0.1-26.5 GHz network analyzer with 50 Ω RF probes.

Device R-SP1 from the first batch has a pull-in voltage of ~60 V and the S_{21} in the on/off state is shown in Fig. A.21(a). At 2 GHz, the on-state insertion loss is -13 dB, and the off-state isolation is -22 dB. This low insertion loss is caused by the downward bending of the bridge. The bending causes a non-flat contact after actuation, and the contact capacitance is thus as large as expected. Device R-SP1 from the second batch achieved better RF performance, and the corresponding S-parameter is shown in Fig. A.21(b). The design R-SP1 has a pull-in voltage of ~40 V and the insertion loss at 60 V V_{DC} is -4.7 dB, and the off-state isolation is -16 dB at 2 GHz. Although the bridge is bent upwards, a solid contact between the upper and lower electrodes is formed during actuation. According to our previous transmission line model, an on/off capacitance ratio of 5 is achieved in this device.

The RF performance of other switch design variations (R-SP2 to R-SP6) is either similar or inferior to the performance of R-SP1 in each fabrication batch, so those RF measurement results are not repeated here. Indeed, some of the design variations have a lower actuation voltage. For example, R-SP3 in batch 1 has an actuation voltage of ~40 V.

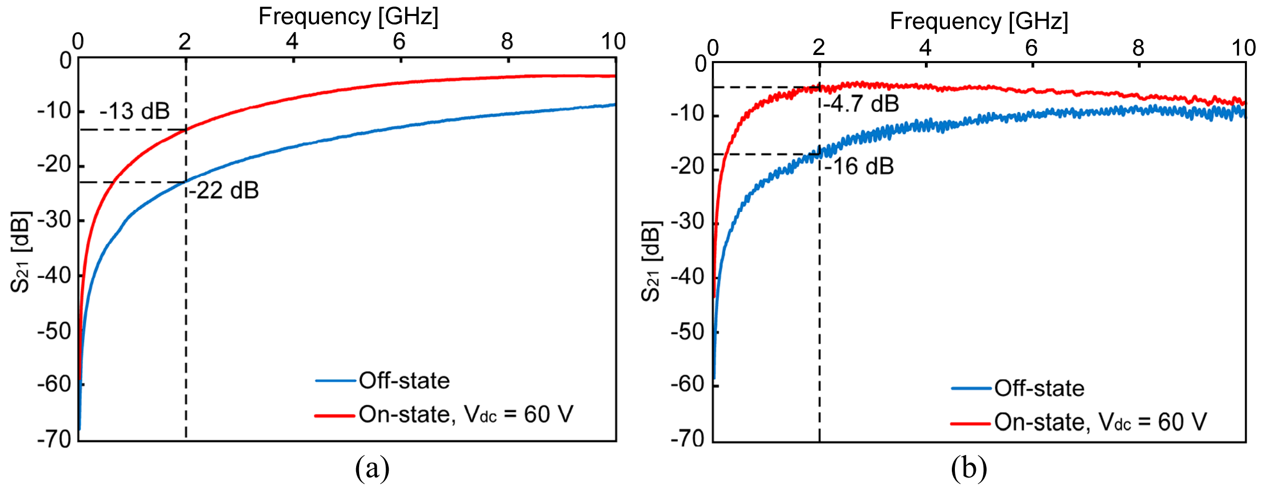

Figure A.21: (a) The measured S-parameter of device R-SP1 from the first batch of fabricated devices. (b) The measured S-parameter of device R-SP1 from the second batch.

In the future, the switch structure will be modified to reduce the out-of-plane bending, allowing a better capacitive contact to be achieved. This can be done if the switch is anchored at four corners. This would require a much higher actuation voltage since the stiffness of the structure will be high. The actuation portion of the switch can be modified so that it lies in the center of the bridge area. This could prevent the unbalanced actuation and potential buckling. Better stress control of the ONO layer could be achieved so that the biaxial stress would be more uniform across the layers, but this is mainly limited by the laboratory equipment. In terms of the device characterization, high power RF measurement can be performed to evaluate the switch power handling capability. The lifetime of the RF switch also needs to be characterized under cold and hot switching conditions.

APPENDIX B

LITERATURE REVIEWS ON RFID ASSISTED SENSOR TECHNOLOGY

As described in Chapter 5, passive RF communication consumes zero power and has moderate communication speed, which is very appealing in wireless sensor network application. One major passive communication method is RFID. This section provides a literature review on the current RFID standards and integrated RFID sensing systems. These ideas can potentially be used to implement the downhole sensing system and save communication power.

A typical schematic diagram of an RFID system is shown in Fig. B.1. During a typical operation cycle, the RFID reader first sends a query to the transponder to initiate communication. The query is a modulated RF signal. The carrier signal powers up the transponder via the energy harvester module. The impedance matching network and demodulator convert the RF signal into digital form, which is then picked up by the processor. The processor controls the modulator, which modulates the signal with amplitude-shift keying (ASK). The modulator then changes the antenna impedance by shorting or opening an antenna stub, with the modulated signal from the processor. The reflected RF signal is picked up by the reader and communication is established.

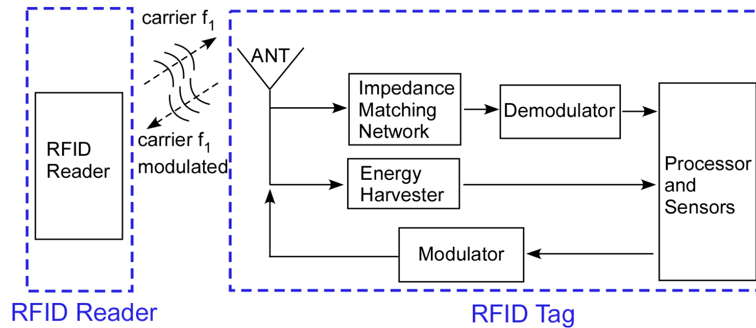

Figure B.1: Schematic diagram of a typical RFID system [Sam08, Una11, Kha14, Ser15]. The transponder modulates and backscatters the RF signal for data transmission.

There are several existing RFID standards that deal with the air interface protocol (the way tags and readers communicate), data content (the way data is organized or formatted), conformance (ways to test that products meet the standard) and applications (how standards are used on shipping labels, for example). The International Organization for Standardization (ISO) has created multiple standards for RFID, including a standard for the air interface protocol for RFID tags used in payment systems and contactless smart cards (ISO 14443) and in vicinity cards (ISO 15693). It has also developed RFID standards for automatic identification and item management, which covers the major frequency used in RFID systems around the world, from air interface of 135 kHz to 5.8 GHz. At the same time, the Auto-ID center also developed an RFID standard called the "Electronic Production Code" (EPC), which is used to track items in the supply chain. In 2004, they proposed EPC Class 1 Gen 2, which is widely used in the modern RFID tag product. Both of these standards have been applied in commercial products [Web-Vio].

RFID technology has been used for several platforms, such as sensing, product tracking and so on. At the University of Washington, both far field communication (FFC) and near field communication (NFC) RFID-based sensing systems were developed. In their work, they developed programmable computing platforms with combined temperature sensor, accelerometer

and RFID communication modules. The systems had a communication distance of more than 10 cm for NFC RFID tags [Zha15] (Fig. B.2(a)) and 4.5 m for FFC RFID tags [Sam08]. Similar work was done at Florida International University as a generic sensing platform for the internet of things [Kha14]. At Mid-Sweden University, researchers developed an RFID-based sensor platform for packaging surveillance applications. The RFID tags and printed moisture sensors were integrated on a 150×110 mm^2 PCB with an achieved reading range of 3.4 m [Una11]. At Boston University, researchers developed RFID systems with miniaturized RFID antennas for oil field sensing applications. In their system, microfluidic channels were built for transporting those miniaturized sensor tags. An antenna with a size of 380×380×15 μm^3 was fabricated and effective communication was proved in an air and pump oil medium, with a distance of several mm (Fig. B.2(b)) [Ser15].

Research was also conducted towards innovative RFID communication methods. At the VTT Technical Research Centre of Finland, researchers developed an RFID system in the mm-wave frequency range. The idea was achieved by adding an up-converter to the reader and a down-converted to the tag. With this carrier frequency range, the size of the tag antenna was reduced while the communication distance was maintained. A communication distance of 30 cm at 10 GHz carrier frequency was achieved [Pur11]. Multi-channel RFID communication was investigated by using the 3rd harmonics of the original carrier frequency [Ver15]. Chipless RFID systems has also been investigated in recent years. At Monash University, researchers developed a chipless RFID tag (Fig. B.2(c)) [Isl12]. Instead of using a digital chip to modulate the reflection signals, they directly printed the slot antenna on a metal substrate and those slots served as the RFID tags. These tags are read-only, but the cost is substantially reduced by dropping the integrated circuit components.

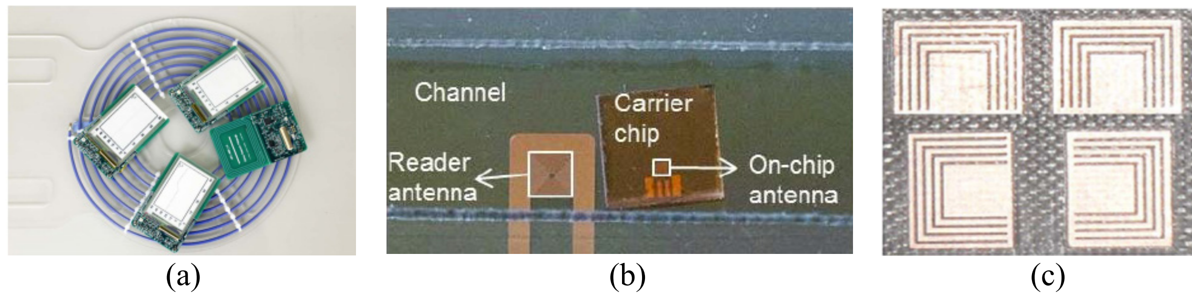

(a) (b) (c)

Figure B.2: (a) The photo of the NFC-RFID platform developed at the University of Washington [Zha15]. (b) The schematic of the miniaturized sensor and microfluidic channel developed at Boston University [Ser15]. (c) Chipless RFID tag fabricated at Monash University [Isl12].

Table B.1 includes the recent published RFID platforms. From the table, it can be seen that RFID platforms are widely used in sensing applications. With an embedded RFID module, the reader can interrogate each sensor node at any time. Passive communication eliminates the requirement for power source conditions in each sensing system, which enhances the system-level reliability. Areas that may potentially benefit include smart home environments, homeland security, healthcare, biometric identification and so on [Kha14].

Table B.1: Comparison of state-of-the-art RFID tags and systems.

RFID Platform	**Tag Size**	**Read Range**	**Power Consumption**	**Protocol & Extra Features**
WISP [Sam08]	Not reported	4.5 m	500 µA active 1.8 µA sleep	EPC Class 1 Gen 1
NFC-WISP [Zha15]	86×54×4.8 mm^3	11.2 cm	9.7 µA sleep	ISO-14443 Battery assisted
GSP-Tag [Kha14]	On protoboard, not reported	5.6 m	1.743 µA Sleep 3622 µA transmit	Battery assisted
RFID Platform Mid-Sweden [Una11]	150×110 mm^2	3.4 m	0.7 µA	Battery assisted
Miniaturized RFID [Ser15]	Antenna: 0.38×0.38 mm^2 On protoboard	1 mm	Passive	Equipped with microfluidic channel
MMID [Pur11]	Antenna: 55×45 mm^2	30 cm	Passive	Operation at 10 GHz, EPC protocol
Passive UHF RFID [Ver15]	85×62 mm^2	>4.5 m	Passive	Operate at f_0 ant $3f_0$, compliance with EPC class 1 Gen 2
Chipless RFID System [Isl12]	7.2×6.4 mm^2	50 mm	Passive	Chipless RFID Non writable Operated at 7-12 GHz
Murata RFID Tag [Mur14]	2×1×0.5 mm^2	1 cm	Passive	EPC Class 2 Gen 2
TI HF Transponder [Tex14]	⌀22×3 mm^3	N/A	Passive	ISO 18000-3

REFERENCE

[Al10] R. Al-Dahleh, R.R. Mansour, "High-capacitance-Ratio Warped-beam Capacitive MEMS Switch Designs," *Journal of Microelectromechanical Systems*, vol. 19, no. 3, pp. 538-547, Jun. 2010.

[Ame07] *Beam Formulas with Shear and Moment Diagrams*, American Forest & Paper Association Inc., Washington, D.C., 2007.

[An14] S. An, N.K. Gupta, Y.B. Gianchandani, "Vacuum Sealing Using Atomic Layer Deposition of Al_2O_3 at 250°C," *Journal of Vacuum Science & Technology -A*, vol. 32, no. 1, Jan. 2014.

[Ana06] D.E. Anagnostou, G. Zheng, M.T. Chryssomallis, J.C. Lyke, G.E. Ponchak, J. Papapolymerou, C.G. Christodoulou, "Design, Fabrication, and Measurements of an RF-MEMS-based Self-similar Reconfigurable Antenna," *IEEE Transactions on Antennas and Propagation*, vol. 54, no. 2, pp. 422-432, Feb. 2006.

[Bad12] M.F Badía, E. Buitrago, A.M. Ionescu, "RF MEMS Shunt Capacitive Switches Using AlN Compared to Si_3N_4 Dielectric," *Journal of Microelectromechanical Systems*, vol. 21, no. 5, pp. 1229-1240, Oct. 2012.

[Bal05] C.A. Balanis, *Antenna Theory: Analysis and Design*. John Wiley & Sons, 2005.

[Bis06] C.M. Bishop, *Pattern Recognition and Machine Learning*. Springer LLC, 2006.

[Bow09] A.F. Bower, *Applied Mechanics of Solids*. CRC Press, 2009.

[Boz00] C. Bozler, R. Drangmeister, S. Duffy, M. Gouker, J. Knecht, L. Kushner, R. Parr, S. Rabe, L. Travis, "MEMS Microswitch Arrays for Reconfigurable Distributed Microwave Components," *IEEE International Microwave Symposium Digest*, Boston, Massachusetts, Jun. 2000, pp. 153-156.

[Caj13] J. Caja, T. Dunstan, M. Caja, "Rechargeable, Lithium-ion Molten Salt Battery for High Temperature Applications," *ECS Transactions*, vol. 50, no. 26, pp. 3-11, 2013.

[Cha12] D. Chapman, W. Trybula, "Meeting the Challenges of Oilfield Exploration Using Intelligent Micro and Nano-Scale Sensors," *IEEE Conference on Nanotechnology (IEEE-NANO)*, Birmingham, United Kingdom, Aug. 2012, pp. 1-6.

[Cho09] J. Choi, J. Ruan, F. Coccetti, S. Lucyszyn, "Three-dimensional RF MEMS Switch for Power Applications," *IEEE Transactions on Industrial Electronics*, vol. 56, no. 4, pp. 1031-1039, Apr. 2009.

[Cla92] E.E. Clarke, F.N. Trofimenkoff, J.W. Haslett, “High-temperature Silicon Diode Models,” *Solid-State Electronics*, vol. 35, no. 1, pp. 103-111, Jan. 1992.

[Cor12] P.D.T. O’Cornor, A. Kleyner, *Practical Reliability Engineering*. John Wiley & Sons, 2012.

[Cou04] R.A. Coutu Jr., P.E. Kladitis, L.A. Starman, J.R. Reid, “A Comparison of Micro-switch Analytic, Finite Element, and Experimental Results,” *Sensors and Actuators A: Physical*, vol. 115, no. 2-3, pp. 252- 258, Sep. 2004.

[Cym14] *Rechargeable Solid State Bare Die Batteries Datasheet*, Cymbet Corporation, Elk River, Minnesota, 2014.

[Dic76] J. Dickson, “On-chip High-voltage Generation MNOS Integrated Circuits Using an Improved Voltage Multiplier Technique,” *IEEE Journal of Solid-State Circuits*, vol. 11, no. 3, pp. 374-378, Jun. 1976.

[Dou12] D. Doughty, E.P. Roth, “A General Discussion of Li Ion Battery Safety,” *The Electrochemical Society Interface*, vol. 21, no. 2, pp. 37-44, Jun. 2012.

[Dup17] *Summary of Properties for Kapton Polyimide - DuPont*, DuPont, Wilmington, Delaware, 2017.

[Eat97] W.P. Eaton, J.H. Smith, “Micromachined Pressure Sensors: Review and Recent Developments,” *Smart Materials and Structures*, vol. 6, no. 5, pp. 530-539, Jun. 1997.

[Ell07] D. Ellis, J. Singer, *Well Logging for Earth Scientists*. Springer, 2007.

[Ene10] *U.S. EIA International Energy Statistics*, U.S. Energy Information Administration, Washington, D.C., 2010.

[Erd07] E. Erdil, K. Topalli, M. Unlu, O.A. Civi, T. Akin, “Frequency Tunable Microstrip Patch Antenna Using RF MEMS Technology,” *IEEE Transactions on Antennas and Propagation*, vol. 55, no. 4, pp. 1193-1196, Apr. 2007.

[Etn89] L.M. Etnyre, *Finding Oil and Gas from Well Logs*. Springer, 1989, pp. 1-20.

[Fin10] K. Finkenzeller, *RFID Handbook*, John Wiley & Sons, Aug. 2010.

[Fou10] S. Fouladi, R.R. Mansour, “Capacitive RF MEMS Switches Fabricated in Standard 0.35 µm CMOS Technology”, *IEEE Transactions on Microwave Theory and Techniques*, vol. 58, no. 2, pp. 478-486, Feb. 2010.

[Gia06] Y.B. Gianchandani, C. Wilson, J.S. Park, “Micromachined Pressure Sensors: Devices, Interface Circuits, and Performance Limits,” *The MEMS Handbook*, ed: M. Gad-el-Hak, CRC Press, 2006.

[Gol98] C.L. Goldsmith, S. Eshelman, Z. Yao, T.H. Lin, D. Denniston, "Performance of Low-loss RF MEMS Capacitive Switches," *IEEE Microwave Guided Wave Letters*, vol. 8, no. 8, pp. 269-271, 1998.

[Gri10] A. Grichener, G.M. Rebeiz, "High-reliability RF-MEMS Switched Capacitors with Digital and Analog Tuning Characteristics," *IEEE Transactions on Microwave Theory and Techniques*, vol. 58, no. 10, pp. 2692-2701, Oct. 2010.

[Hay15] W.M. Haynes, *CRC Handbook of Chemistry and Physics, 96th Edition*. CRC Press, 2015.

[Hen98] D. Hensley, M. Milewits, W. Zhang, "The Evolution of Oil Field Batteries," *Oil Field Review*, vol. 10, no. 3, pp. 42-57, Oct. 1998.

[Her07] C.F. Herrmann, F.W. DelRio, D.C. Miller, S.M. George, V.M. Bright, J.L. Ebel, R.E. Strawser, R. Cortez, K.D. Leedy, "Alternative Dielectric Films for RF MEMS Capacitive Switches Deposited Using Atomic Layer Deposited Al_2O_3/ZnO Alloys," *Sensors and Actuators A: Physical,* vol. 135, no.1, pp. 262-272, Mar. 2007.

[Hol68] R. Holm, *Electric Contacts*. Springer, 1968.

[Hor98] G.V.D. Horn, J. Huijsing, *Integrated Smart Sensors-Design and Calibration*. Springer, 1998.

[Isl12] M.A. Islam, N.C. Karmakar, "A Novel Compact Printable Dual-polarized Chipless RFID System," *IEEE Transactions on Microwave Theory and Techniques*, vol. 60, no. 7, pp. 2142-2151, Jul. 2012.

[Ixy12] *CPC1822 4V Output Solar Cell Datasheet*, IXYS Integrated Circuits Division, Beverly, Massachusetts, 2012.

[Jac06] C.B. Jacobina, I.S.D. Freitas, E.R.C.D. Silva, A.M.N. Lima, R.L.D.A. Ribeiro, "Reduced Switch Count DC-link AC–AC Five-leg Converter," *IEEE Transactions on Power Electronics*, vol. 21, no. 5, pp. 1301-1310, Sep. 2006.

[Kha14] M.S. Khan, M.S. Islam, H. Deng, "Design of a Reconfigurable RFID Sensing Tag as a Generic Sensing Platform toward the Future Internet of Things," *IEEE Internet of Things Journal*, vol. 1, no. 4, pp. 300-310, Aug. 2014.

[Kum14] S.S. Kumar, B.D. Pant. "Design Principles and Considerations for the 'Ideal' Silicon Piezoresistive Pressure Sensor: a Focused Review," *Microsystem Technologies*, vol. 20, no. 7, pp. 1213-1247, Jul. 2014.

[Ko07] H.S. Ko, C.W. Liu, C. Gau, "Novel Fabrication of a Pressure Sensor with Polymer Material and Evaluation of its Performance," *Journal of Micromechanics and Microengineering*, vol. 17, no. 8, pp. 1640-1648, Jul. 2007.

[Kon14] *Brochure-Engine Monitoring Systems*, Kongsberg, Novi, Michigan, Aug. 2014.

[Lee89] J.M. Hill, A.I. Lee, "Large Elastic Compression of Finite Rectangular Blocks of Rubber," *The Quarterly Journal of Mechanics and Applied Mathematics*, vol. 42, no. 2, pp. 267-287, May 1989.

[Luc04] S. Lucyszyn, "Review of Radio Frequency Microelectromechanical Systems Technology," *IEE Proceedings - Science, Measurement & Technology*, vol. 151, no. 2, pp. 93-103, Mar. 2004.

[Luo14] X. Luo, C.K. Eun, Y.B. Gianchandani, "Fabrication of a Monolithic Microdischarge-Based Pressure Sensor for Harsh Environments," *IEEE/ASME International Conference on Micro Electro Mechanical Systems (MEMS '14)*, San Francisco, California, Jan. 2014.

[Ma15] Y. Ma, Y. Sui, T. Li, Y.B. Gianchandani, "A Submillimeter Package for Microsystems in High-pressure and High-salinity Downhole Environment," *Journal of Microelectromechanical Systems*, vol. 24, no. 4, pp. 861-869, Aug. 2015.

[Mah10] R. Mahameed, G.M. Rebeiz, "A High-power Temperature-stable Electrostatic RF MEMS Capacitive Switch Based on a Thermal Buckle-beam Design," *Journal of Microelectromechanical Systems*, vol. 19, no. 4, pp. 816-826, Aug. 2010.

[Mcc12] F.P. McCluskey, T. Podlesak, R. Grzybowski, *High Temperature Electronics*. CRC Press, 2012.

[Mih01] R.E. Mihailovich, M. Kim, J.B. Hacker, E.A. Sovero, J. Studer, J.A. Higgins, J.F. DeNatale, "MEM Relay for Reconfigurable RF Circuits," *IEEE Microwave and Wireless Components Letters*, vol. 11, no. 2, pp. 53-55, Feb. 2001.

[Muñ07] D. Muñoz-Rojas, J. Leriche, C. Delacourt, P. Poizot, M. Palacín, J. Tarascon, "Development and Implementation of a High Temperature Electrochemical Cell for Lithium Batteries," *Electrochemistry Communications*, vol. 9, no. 4, pp. 708-712, Apr. 2007.

[Mur14] *MAGICSTRAP® Product Brief*, Murata Electronics, Nagaokakyo, Japan, 2014.

[Mur15] *MEMS Sensors and Sensing Elements*, Murata Electronics, Nagaokakyo, Japan, 2015.

[Ohr98] M. Ohring, *Reliability and Failure of Electronic Materials and Devices*. Academic Press, 1998.

[Ope13] *Smartball Flowable Pressure and Temperature Micro-recorder*, Openfield Technology, Versailles, France, 2013.

[Ozk12] F.M. Ozkeskin, S. Choi, K. Sarabandi, Y.B. Gianchandani, "Batch-fabricated High-power RF Microrelays with Direct on-PCB Package," *Journal of Microelectromechanical System*, vol. 21, no. 4, pp. 990-1001, Aug. 2012.

[Pac00] S.P. Pacheco, L.P.B. Katehi, C.T.C. Nguyen, "Design of Low Actuation Voltage RF MEMS Switch," *IEEE International Microwave Symposium Digest*, Boston, Massachusetts, Jun. 2000, pp.165-168.

[Pal04] G. Palumbo, D. Pappalardo, M. Gaibotti, "Charge Pump Circuits: Power Consumption Optimization - A Summary," *IEEE Circuits and Systems Magazine*, vol. 4, no. 3, pp. 26-29, 2004.

[Par12] K.J. Park, S.M. Kang, H.S. Kim, C.W. Baek, T.K. Chung, "Energy Scavenging System Utilizing MEMS Switch for Power Management," *Electronics Letters*, vol. 48, no. 15, pp. 948-949, Jul. 2012.

[Pat12] C.D. Patel, G.M. Rebeiz, "A High-reliability High-linearity High-power RF MEMS Metal-contact Switch for DC-40GHz Applications," *IEEE Transactions on Microwave Theory and Techniques*, vol. 60, no. 10, pp. 3096-3112, Oct. 2012.

[Ped97] M. Pedersen, M.G.H. Meijerink, W. Olthuis, P. Bergveld, "An IC-compatible polyimide pressure sensor with capacitive readout," *Sensors and Actuators A: Physical*, vol. 63, no. 3, pp. 163-168, Dec. 1997.

[Per11] A. Persano, A. Cola, G.D. Angelis, A. Taurino, P. Siciliano, F. Quaranta, "Capacitive RF MEMS Switches with Tantalum-based Materials", *Journal of Microelectromechanical Systems*, vol. 20, no. 2, pp. 365-370, Apr. 2011.

[Per14] *PE42542 datasheet*, Peregrine Semiconductor, San Diego, California, 2014.

[Pie96] R.F. Pierret, *Semiconductor Device Fundamentals*. Pearson Education, 1996, pp. 270-282.

[Pur11] P. Pursula, F. Donzelli, H. Seppä, "Passive RFID at Millimeter Waves," *IEEE Transactions on Microwave Theory and Techniques*, vol. 59, no. 8, pp. 2151-2157, Aug. 2011.

[Qia14] X.Y. Qiao, J.M. Liu, X.M. Zhang, J. Liu, Z.Q. Liu, "Approach to Design Digital Meter for Monitoring Armored Vehicle Engine," *Applied Mechanics and Materials*, vol. 599-601, pp. 835-840, Aug. 2014.

[Rad15] *SPST RF-MEMS Switch DC to 12 GHz RMWS101 Datasheet*, Radant MEMS, Littleton, Massachusetts, 2015.

[Rap13] T.S. Rappaport, S. Sun, R. Mayzus, H. Zhao, Y. Azar, K. Wang, G.N. Wong, J.K. Schulz, M. Samimi, F. Gutierrez, "Millimeter Wave Mobile Communications for 5G Cellular: It Will Work!" *IEEE Access*, vol. 1, pp. 335-349, 2013.

[Reb03] G.M. Rebeiz, *RF MEMS: Theory, Design and Technology*. John Wiley & Sons, 2003.

[Rei02] J.R. Reid, "Simulation and Measurement of Dielectric Charging in Electrostatically Actuated Capacitive Microwave Switches," *Proceedings of the International Conference on Modeling and Simulation of Microsystems*, San Juan, Puerto Rico, Apr. 2002, pp. 250-253.

[Rob97] A.D. Robertson, A.R. West, A.G. Ritchie, "Review of Crystalline Lithium-ion Conductors Suitable for High Temperature Battery Applications," *Solid State Ionics*, vol. 104, no. 1, pp. 1-11, Dec. 1997.

[Roy03] K. Roy, S. Mukhopadhyaym, H. Mahmoodi-Meimand, “Leakage Current Mechanisms and Leakage Reduction Techniques in Deep-submicrometer CMOS Circuits,” *Proceedings of the IEEE*, vol. 91, no. 2, pp. 305-327, Feb. 2003

[Sam08] A.P. Sample, D.J. Yeager, P.S. Powledge, A.V. Mamishev, J.R. Smith, “Design of an RFID-based Battery-free Programmable Sensing Platform,” *IEEE Transactions on Instrumentation and Measurement*, vol. 57, no. 11, pp. 2608-2615, Nov. 2008.

[Sch06] Schlumberger, “Crosswell Electromagnetic Resistivity Imaging: Illuminating the Reservoir,” *Middle East & Asia Reservoir Review*, no. 7, pp. 24-33, Nov. 2006.

[Sch98] J. Schimkat, “Contact Materials for Microrelays,” *IEEE/ASME International Conference on Micro Electro Mechanical Systems (MEMS’98)*, Heidelberg, Germany, Jan. 1998.

[Sei11] *MS Lithium Rechargeable Battery Precautions for Handling and Usage*, Seiko Instruments Inc., Chiba, Japan, 2011.

[Sei12] *Guide for Rechargeable Battery Charging Circuit*, Seiko Instruments Inc., Chiba, Japan, 2012.

[Sei13] *MS412FE Product Specification*, Seiko Instruments Inc., Chiba, Japan, 2013.

[Sei14] *Micro Battery Product Catalogue*, Seiko Instruments Inc., Chiba, Japan, 2014.

[Ser15] H.R. Seren, X. Zhao, C. Chen, C. Wang, X. Zhang, “Enabling a Microfluidic RFID Readout System via Miniaturization and Integration,” *Journal of Microelectromechanical Systems*, vol. 24, no. 2, pp. 395-403, Apr. 2015.

[She14] S. Sherrit, H. Lee, P. Walkemeyer, J. Hasenoehrl, J. Hall, T. Colonius, L. Tosi, A. Arrazola, N. Kim, K. Sun, G. Corbett, “Flow Energy Piezoelectric Bimorph Nozzle Harvester,” *Proceedings of the SPIE*, vol. 9057, Apr. 2014.

[Shi15] Z. Shi, Y. Chen, M. Yu, S. Zhou, N. Al-Khanferi, “Development and Field Evaluation of a Distributed Microchip Downhole Measurement System,” *SPE Digital Energy Conference and Exhibition*, The Woodlands, Texas, Mar. 2015.

[Sho89] F. Shoucair, “Scaling, Subthreshold, and Leakage Current Matching Characteristics in High-temperature (25°C-250°C) VLSI CMOS Devices,” *IEEE Transactions on Components, Hybrids, and Manufacturing Technology*, vol. 12, no. 4, pp. 780-788, Dec. 1989.

[Sil11] *C8051F99x-C8051F98x Datasheet*, Silicon Laboratories, Austin, Texas, 2011.

[Sil15] *Quarterly Quality & Reliability Report*, Silicon Laboratories, Austin, Texas, 2015.

[Smi88] M.J.S. Smith, “On the Circuit Analysis of Schmitt Trigger,” *IEEE Journal of Solid-State Circuits*, vol. 23, no. 1, pp. 292-294, Feb. 1988.

[Web-Blu] *Bluetooth*. Available: https://en.wikipedia.org/wiki/Bluetooth. Accessed Nov. 2015.

[Web-Har] *Go Ahead-Take 28nm FD-SOI out for a Test Drive*. Available: http://www.advancedsubstratenews.com/2012/10/go-ahead-take-28nm-fd-soi-out-for-a-test-drive. Accessed on Sep. 2015.

[Web-Smi] L.I Smith. *A Tutorial on Principal Component Analysis*. Available: http://csnet.otago.ac.nz/cosc453/student_tutorials/principal_components.pdf. Accessed on April. 2017.

[Web-Vio] Bob Violino. *A Summary of RFID Standards*. Available: http://www.rfidjournal.com/articles/view?1335/2. Accessed on Nov. 2015.

[Web-WiF] *WiFi*. Available: https://en.wikipedia.org/wiki/Wi-Fi. Accessed on Nov. 2015.

[Web-Zig] *ZigBee*. Available: https://en.wikipedia.org/wiki/ZigBee. Accessed on Nov. 2015.

[Spe12] W.M. van Spengen, "Capacitive RF MEMS Switch Dielectric Charging and Reliability: A Critical Review with Recommendations," *Journal of Micromechanics and Microengineering*, vol. 22, no. 7, Jun. 2012.

[Stm14] *LSM303C Datasheet*, STMicroelectronics, Geneva, Switzerland, Jun. 2014.

[Sze88] S.M. Sze, *VLSI Technology*, McGraw Hill Companies, 1988.

[Tad11] *Model TLH2450 Datasheet*, Tadiran Batteries, Feb. 2011.

[Tak08] K. Takahata, Y.B. Gianchandani, "A Micromachiend Capacitive Pressure Sensor Using a Cavity-less Structure with Bulk-Metal/Elastomer Layers and Its Wireless Telemetry Application," *Sensors*, vol. 8, no. 4, pp. 2317-2330, Apr. 2008.

[Tex04] *TLV3011, TLV3012 Datasheet*, Texas Instruments, Dallas, Texas, 2004.

[Tex14] *RI-I16-112A-03 Tag-it™ HF-I Plus Transponder Inlays 24.2-mm Circular*, Texas Instrument, Dallas, Texas, Jun. 2014.

[Tim85] A. Timur, "Downhole Geophysical Logging," *Annual Review of Earth and Planetary Sciences*, vol. 13, pp. 315-344, 1985.

[Tri14] *TQP4M0008 datasheet*, TriQuint Semiconductor, Hillsboro, Oregon, Oct. 2014.

[Una11] T. Unander, J. Sidén, H. Nilsson, "Designing of RFID-based Sensor Solution for Packaging Surveillance Applications," *IEEE Sensors Journal*, vol. 11, no. 11, pp. 3009-3018, Nov. 2011.

[Ver15] G.A. Vera, Y. Duroc, S. Tedjini, "Third Harmonic Exploitation in Passive UHF RFID," *IEEE Transactions on Microwave Theory and Techniques*, vol. 63, no. 9, pp. 2991-3004, Sep. 2015.

[Wat12] J. Watson G. Castro, "High-temperature Electronics Pose Design and Reliability Challenges," *Analog Dialogue*, vol. 46, Apr. 2012.

[Wol12] D. Wolpert, P. Ampadu, *Managing Temperature Effects in Nanoscale Adaptive Systems*. Springer, 2012.

[Yan13] J. Yang, "A Harsh Environment Wireless Pressure Sensing Solution Utilizing High Temperature Electronics," *Sensors*, vol. 13, no. 3, pp. 2719-2734, Mar. 2013.

[Yu12] M. Yu, S. He, Y. Chen, N. Takach, P. LoPresti, S. Zhou, N. Al-Khanferi, "A Distributed Microchip System for Subsurface Measurement," *SPE Annual Technical Conference and Exhibition*, San Antonio, Texas, Oct. 2012.

[Zha15] Y. Zhao, J.R. Smith, A. Sample, "NFC-WISP: A Sensing and Computationally Enhanced Near-Field RFID Platform," *IEEE International Conference on RFID (RFID)*, San Diego, California, Apr. 2015, pp. 174-181.